

COMPUTATIONAL DESIGN, SENSITIVITY ANALYSIS AND OPTIMIZATION OF FUEL
REFORMING CATALYTIC REACTOR

By

Arman Raoufi

James C. Newman III
Professor of Computational Engineering
(Chair)

Sagar Kapadia
Research Assistant Professor of
Computational Engineering
(Committee Member)

Robert S. Webster
Research Associate Professor of
Computational Engineering
(Committee Member)

James Hiestand
Professor of Mechanical Engineering
(Committee Member)

COMPUTATIONAL DESIGN, SENSITIVITY ANALYSIS AND OPTIMIZATION OF FUEL
REFORMING CATALYTIC REACTOR

By

Arman Raoufi

A Dissertation Submitted to the Faculty of the University of
Tennessee at Chattanooga in Partial Fulfillment
of the Requirements of the Degree of
Doctor of Philosophy in Computational Engineering

The University of Tennessee at Chattanooga
Chattanooga, Tennessee

August 2016

Copyright © 2016
By Arman Raoufi
All Rights Researved

ABSTRACT

In this research, the catalytic combustion of methane is numerically investigated using an unstructured, implicit, fully coupled finite volume approach. The nonlinear system of equations is solved by Newton's method. The catalytic partial oxidation of methane over a rhodium catalyst in one channel of a coated honeycomb reactor is studied three-dimensionally, and eight gas-phase species (CH_4 , CO_2 , H_2O , N_2 , O_2 , CO , OH and H_2) are considered for the simulation. Surface chemistry is modeled by detailed reaction mechanisms including 38 heterogeneous reactions with 20 surface-adsorbed species for the Rh catalyst and 24 heterogeneous reactions with 11 surface-adsorbed species for Pt catalyst. The numerical results are compared with experimental data and good agreement is observed. Effects of the design variables, which include the inlet velocity, methane/oxygen ratio, catalytic wall temperature, and catalyst loading on the cost functions representing methane conversion and hydrogen production are numerically investigated. The sensitivity analysis for the reactor is performed using three different approaches: finite difference, direct differentiation and an adjoint method. Two gradient-based design optimization algorithms are utilized to improve the reactor performance. For additional test cases, the performance of two full scale honeycomb-structured reactors with 49 and 261 channels are investigated. The sensitivity analysis of the full reactor is performed using an adjoint method with four design variables consisting of the inlet velocity, inflow methane concentration, inlet oxygen density and thermal conductivity of the monolith.

DEDICATION

This dissertation is lovingly dedicated to my mother, Zahra Ghorbannejad, who passed away in November, 2015 and could not see this dissertation completed, for her lifetime support, encouragement, and unbounded love.

ACKNOWLEDGMENTS

My deepest gratitude goes to my beautiful wife Maryam for her support, encouragement, kindness and unbounded love and my lovely sweet daughter Ava.

I would like to express my special appreciation and thanks to my advisor Dr. James Newman for devoting a great deal of time to answer my questions and offer suggestions. I wish to express my thanks to Dr. Sagar Kapadia for his time and effort over the past five years. Without their guidance and encouragement throughout my time as a graduate student, this work would not have been possible. I also thank my other committee members, Dr. Robert Webster and Dr. James Hiestand for their guidance regarding this work. In addition, I would like to express my appreciation to Dr. Timothy Swafford for his support and help.

This work was supported by the Office of Naval Research (ONR) Grant No. N00014-10-1-0882 and the Tennessee Higher Education Commission (THEC) Center of Excellence in Applied Computational Science and Engineering (CEACSE). This support is greatly appreciated.

TABLE OF CONTENTS

ABSTRACT	iv
DEDICATION	v
ACKNOWLEDGMENTS	vi
LIST OF TABLES	ix
LIST OF FIGURES	x
LIST OF ABBREVIATIONS	xiii
LIST OF SYMBOLS	xiv
CHAPTER	
1. INTRODUCTION	1
2. GOVERNING EQUATIONS AND NUMERICAL SOLUTION.....	12
2. 1. Modeling the surface chemistry	17
2.1.1 Gas-phase chemistry model	19
2.1.2 Surface chemistry model	20
2.2. Sensitivity derivatives.....	28
3. NUMERICAL SIMULATION OF CATALYTIC COMBUSTION IN STAGNATION FLOW	32
3. 1. Methane oxidation on a platinum surface	37
3. 2. Methane oxidation on a platinum surface	44
4. CATALYTIC PARTIAL OXIDATION OF METHANE	50
4.1. Parallel performance	50
4.2. Validation for the catalytic partial oxidation of methane.....	53
4.3. Parameter study	60
4.4. Sensitivity Analysis	69
4.5. Optimization	70
5. NUMERICAL SIMULATION A HONEYCOMB-STRUCTURED CATALYTIC REFORMING REACTOR	76
5.1. Sensitivity analysis of the full reactor	87

6. CONCLUSION.....	89
6.1. Summary	89
6.2. Recommendations for future work	90
REFERENCES	92
APPENDIX	
A. CANTERA FILE FOR CATALYTIC COMBUSTION OF HYDROGEN ON PALLADIUM	96
B. REACTION MECHANISM FOR METHANE CATALYTIC COMBUSTION ON PLATINUM....	101
C. REACTION MECHANISM FOR METHANE CATALYTIC COMBUSTION ON RHODIUM	103
VITA.....	106

LIST OF TABLES

1 The literature review and numerical studies were carried out in the field of the catalytic combustion.....	8
2 Reaction mechanism for methane combustion on a Pt surface [6]	39
3 Reaction mechanism for iso-octane combustion on a Rh surface [12]	46
4 Initial conditions for catalytic partial oxidation of methane	54
5 Baseline conditions for catalytic combustion of methane.....	61
6 The sensitivity derivatives for the different design variables	70
7 Initial values and constrained bounds for the design variables	73
8 the number of solver and gradients calls for the optimization algorithms	74
9 Initial conditions for fuel reforming reactor	78
10 Sensitivity derivatives of both cost functions obtained using the discrete adjoint method for the full reactor	88

LIST OF FIGURES

1 The different kind of the catalytic reactors	2
2 Monoliths with various channel shapes [3].....	3
3 Catalytic combustion monolith and physical and chemical process occurring in the monolith reformer .	4
4 Control Volume based on Median Dual	15
5 Methods for modeling the chemical reaction rate of heterogeneous reactions	18
6 Schematic of the coupling between the gas and the surface due to transport and heterogeneous chemistry	21
7 Normalized runtimes for solving the stiff problem.....	26
8 Data exchange between the solver and Cantera through the interface.....	28
9 The schematic of stagnation-point flow	35
10 The solution algorithm for solving the ODE equations	36
11 Geometry and boundary conditions for catalytic combustion of methane on the platinum surface	38
12 The comparison between the obtained numerical results with experimental data reported by [42]	40
13 Velocity and temperature profiles for the surface temperature 800 K.....	41
14 Effect of the surface temperature on CH ₄ concentration.....	41
15 Surface site fraction for the different surface temperature.....	42
16 Gas phase species concentrations for the surface temperature 1200 K.....	43
17 Geometry and boundary conditions for catalytic combustion of iso-octane over the Rhodium surface	44
18 Effect of the surface temperature on I-C ₈ H ₁₈ concentration	47
19 Surface coverages for the different surface temperature.....	48
20 Gas phase species concentrations for the surface temperature 1100 K.....	49
21 The total run times for the different number processors	51

22 Parallel performance using Speedup	52
23 Grid generated for the channel of reactor	54
24 Convergence history of the solution	55
25 Comparison between the numerical results and experimental data for the partial oxidation of methane	56
26 The mole fraction of species along symmetry axis of the reformer for both catalyst Rh and Pt	57
27 Contour plots for the reactor with Platinum catalyst	58
28 Contour plots for the reactor with Rhodium catalyst	59
29 The comparison of the mole fraction of species along symmetry axis of the reformer	61
30 The mole fraction contour for the reactor with the inlet velocity 2 m/s	62
31 The comparison of the mole fraction of species along symmetry axis of the reformer	63
32 The influence of the variation of methane/oxygen ratio on the reformer performance	64
33 The mole fraction contour for the reformer with the methane/oxygen ratio 1/3	65
34 The influence of the variation of the catalyst loading on the reformer performance	67
35 The mole fraction contour for the reformer with $F_{cat}/geon = 0.5$	68
36 The data interchange and interface between the flow solver and DAKOTA	72
37 The comparison between the optimized conditions for methane concentration along the reactor	74
38 The comparison between the base condition and the optimized condition for hydrogen concentration	75
39 The cylindrical monolithic reactor with square cross-section channels	77
40 The generated grid for the monolithic reactor	77
41 The boundary conditions for the monolithic reactor and mesh cross-section	78
42 Contours of a) Temperature b) Velocity for the reactor at test conditions 1	80
43 Contour plots for species mole fractions for test condition 1 a) CH ₄ b) CO ₂ c) CO d) H ₂ e) H ₂ O f) O ₂	81
44 Contours of a) Velocity b) Temperature for the reactor at test conditions 2	82
45 Contour plots for species mole fractions at test conditions 2 a) CH ₄ b) CO ₂ c) CO d) H ₂ e) H ₂ O f) O ₂	83

46 The structure of the reactor	84
47 The mesh generated for the simulation	85
48 The boundary conditions for the simulation	85
49 Contour plots for the reactor a) O ₂ b) CH ₄ c) H ₂ d) CO ₂ e) Temperature.....	87

LIST OF ABBREVIATIONS

ATR, Auto Thermal Reforming

CFD, Computational Fluid Dynamics

SOFC, Solid Oxide Fuel Cell

LIST OF SYMBOLS

c_t , Total molar mixture concentration

D_{ij} , Binary mass diffusion coefficient of species i into species j

D_i^{kn} , Knudsen diffusion coefficient

\vec{F}_e , Inviscid flux vector

\vec{F}_v , Viscous flux vector

E , Young's modulus

e_i , Species internal energy

e_t , Specific total energy (total energy per unit mass)

h_i , Species enthalpy

J_i , Mass diffusion flux vector for species i

\tilde{k} , Heat transfer coefficient

MW , Mean molecular weight of the mixture

MW_j , Molecular weight of species j

N_i , Diffusion molar flux

ns , Number of species

p , Pressure (mixture)

p_i , Partial pressure

\vec{Q} , Conservative flow variables

\hat{q} , Heat flux vector

R_i , Gas constant

R_u , Universal gas constant

\vec{S} , Source term vector

T , Temperature

u , x-velocity

U_i , Species diffusion velocity

v , y-velocity

w , z-velocity

X_j , Mole fraction of species j

Y_i , Mass fraction of species i

Greek symbols

ρ , Mixture density

ρ_i , Species density

Ω_μ , Collision integral value for viscosity

Ω_{ij} , Collision integral

μ , Dynamic viscosity (mixture)

τ , Shear stress tensor

$\dot{\omega}_i$, Reaction rate source term for the species i

σ , Lennard-Jones collision diameter

$\tau_{xy}, \tau_{yz}, \tau_{zx}$, Shear stresses

$\varepsilon_{xx}, \varepsilon_{yy}, \varepsilon_{zz}$, Normal strains

$\gamma_{xy}, \gamma_{yz}, \gamma_{zx}$, Shear strains

α , Thermal expansion coefficient

CHAPTER 1

INTRODUCTION

The Fuel reformer is one of the most important components of the SOFC system. The purpose of the fuel reformer is to convert the chemical composition of primary fuel into the species that systems like SOFCs can be operated with. Fuel reforming can be broadly classified into three categories including, steam reforming (SR), partial oxidation (POX) and autothermal reforming (ATR). The reactors used in reforming process can have many different structures such as pack bed and monolith, depending on the application and other parameters. These reactors are categorized as the catalytic reactors. Catalytic reactors are widely used in fuel reforming processes and have engineering applications such as in automotive catalytic converters, gas turbines, and for portable radiant heaters. There are many kinds of the catalytic reactors used in the industry as summarized in Figure 1. These reactors are mainly required for environment concerns with regards to reducing pollutants and emission levels. The catalytic reactor can be distinguished from the conventional reactor by considering fundamental differences between homogeneous (conventional) combustion and catalytic combustion. The main differences can be summarized as [1]:

- Conventional combustion occurs in the presence of a flame, while catalytic combustion is a flameless process.
- Catalytic combustion generally proceeds at a lower temperature than conventional combustion.

- Catalytic combustion results in lower emission of oxides of nitrogen.
- Conventional combustion can only exist within well-defined fuel-to-air ratios. Catalytic combustion is not constrained by such conditions.
- Catalytic combustion can offer fewer constraints on reactor design.

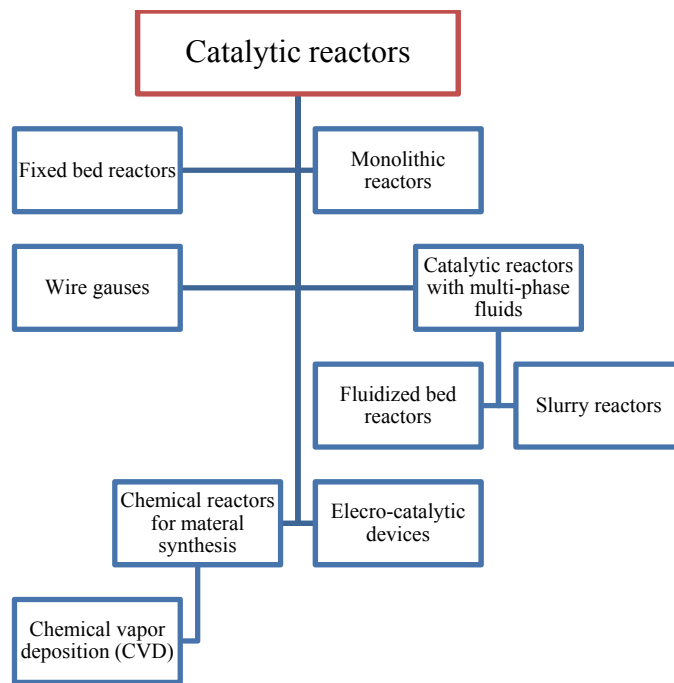


Figure 1 The different kind of the catalytic reactors

The monolith or honeycomb reactor is a commonly-used configuration in the fuel reforming industry. With the catalyst being coated on the channel walls, these structures consist of a number of parallel passageways through which the gas flows. The monolith configuration offers a number of interesting features including a high surface to volume ratio with low pressure drop that may be exploited in reactor design [1].

Monolith channels can have various cross-sectional shapes, e.g. circular, hexagonal,

square or sinusoidal (Figure 2). Monolith structures can be manufactured to have a specified size of channel, cell density, and wall thickness. Materials for the support vary ranging from ceramics [2] to metallic alloys.

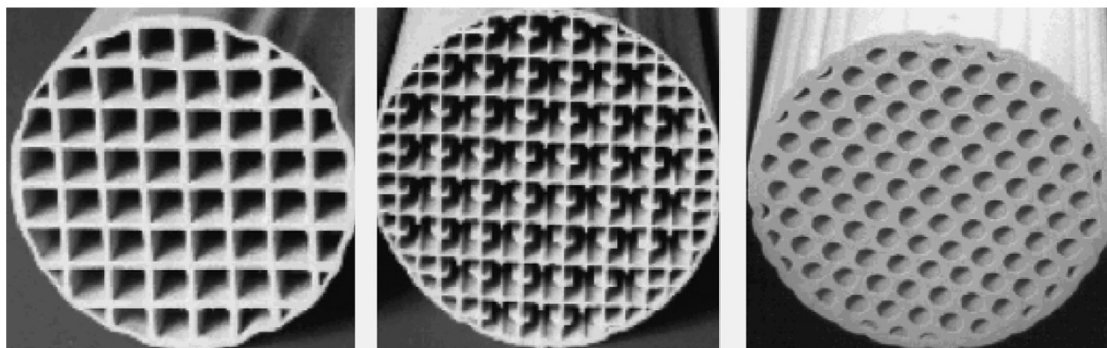


Figure 2 Monoliths with various channel shapes [3]

Catalytic monolithic reactors are generally characterized by the complex interaction of various physical and chemical processes. Figure 3 illustrates the physics and chemistry in a catalytic combustion monolith. The flow field includes the complex transport of momentum, energy, and chemical species. The reactants diffuse to the inner channel wall, which is coated with the catalytic material, where the gaseous species adsorb and react on the surface. The products diffuse back into the flow. Since most reforming processes are conducted at high temperatures, homogeneous reactions in the gas phase can accompany the heterogeneous reactions in the catalytic wall. In catalytic reactors, the catalyst material is often dispersed in porous structures, such as washcoats or pellets. Mass transport in the fluid phase and chemical reactions are then superimposed by diffusion of the species to the active catalytic centers in the pores [2].

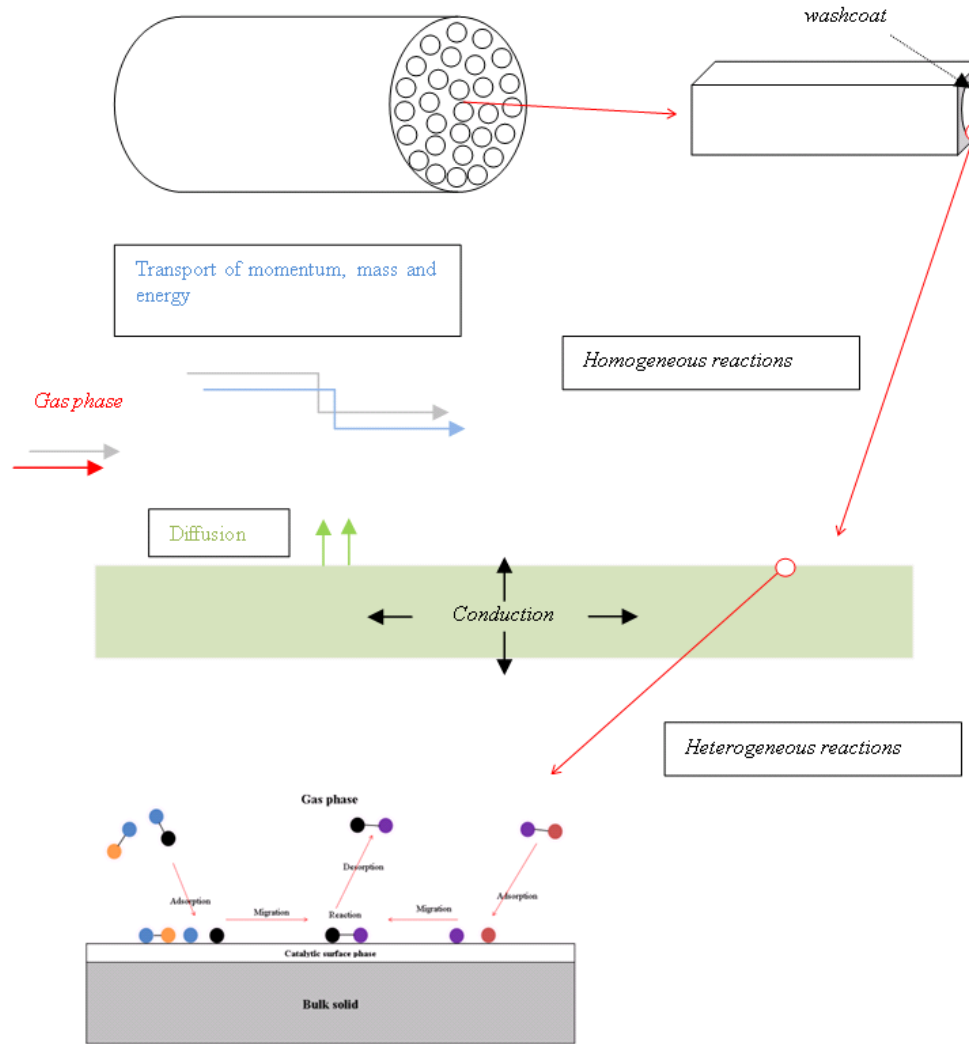


Figure 3 Catalytic combustion monolith and physical and chemical process occurring in the monolith reformer

Because of the complexity and coupled interaction between mass and heat transfer, design and optimization of catalytic reactors is challenging. Computational fluid dynamics (CFD) can be used to simulate and understand the physical and chemical interactions within the reactor. Moreover, this predictive capability may then be utilized to perform reactor design or offer design alternatives. However, an enabling technology is the need to develop robust and reliable numerical methods to model the fluid mechanics which includes the complex chemical

reactions. The use of detailed models for chemical reactions is exceedingly challenging due to the large number of species involved, nonlinearity, and multiple time scales arising from the complex reacting systems. The resulting partial differential equations (PDEs) tend to be very large and stiff systems, with highly nonlinear boundary conditions [3].

In addition to design and optimization, CFD can be used to support experimental testing of these catalytic reactors. For example, Hettel *et al.* (2013) developed a numerical model to study the in situ effect of a probe insertion on the velocity and species profiles [4]. Therefore, numerical modeling combined with experimental measurements together should be used to provide a comprehensive and detailed understanding of catalytic reactors.

Modeling of monolithic reactors can be broadly divided in two categories: single-channel modeling that considers just one channel of the monolith and full-scale modeling that considers the whole reactor comprised of several hundred channels [5] [6]. Single-channel models can be one-dimensional, two-dimensional or three-dimensional.

Simulations for a single-channel have been previously performed using one-, two- and three-dimensional models. One-dimensional (1D) models ignore radial and angular gradients in temperature, concentration, and velocity, and consider only axial variations. These models, which use lumped heat and mass coefficients, are widely used because of their simplicity, ease of implementation, and computational efficiency. The resulting one-dimensional model is typically referred to as the plug-flow model.

In the monolith channel, the catalytic reaction occurs in the washcoat on the channel wall. There are two choices for incorporating the catalyst reaction into the heat and mole balance equations: pseudo-homogeneous models and heterogeneous models. In the pseudo-homogeneous model, the wall temperature and concentrations are assumed to be the same as the fluid, and the

reaction rate is incorporated directly into the conservation equations. For the heterogeneous model, the gas-solid interface at the wall is assumed to be discontinuous and separate mole and energy balance equations are solved for the solid. These equations are coupled to the fluid equations through mass and heat transfer coefficients. The catalytic reactor results presented in this report utilize the heterogeneous model for surface chemistry. Since no diffusive terms remain, the plug-flow equations form a differential-algebraic-equation (DAE) initial-value problem for the axial variation of the mean species composition [6].

The catalytic partial oxidation of hydrogen was previously investigated by Cerkanowicz *et al.* (1977) [7] with simplified chemistry and by Kramer *et al.* (2002) [8] with detailed kinetics. Two and three-dimensional models are more complex but provide more realistic results than the one-dimensional models. These models are developed based on both boundary-layer equations and the Navier-Stokes equations. In boundary-layer approximations, axial (flow-wise) diffusive transport is neglected, but detailed transport to and from the channel walls is retained. Deutschmann *et al.* (2000) [9] and Dogwiler *et al.* (1999) [10] used Navier-Stokes 2D models with detailed heterogeneous and homogeneous chemistry for simulation of the catalytic combustion. The catalytic combustion of methane-air was studied by Markatou *et al.* (1993) [11] using a 2D boundary layer model. Raja *et al.* (2000) [6] investigated the efficiency and validity range of the Navier–Stokes, boundary-layer, and plug-flow models in a catalytic monolithic channel. Their research showed that the boundary-layer models provide accurate results with low computational cost. Kumar (2009) [5] developed a new implicit solver for species conservation equations and investigated the flow field in a full-scale 3D catalytic converter. The catalytic combustion of iso-octane over rhodium catalysts was studied by Hartmann *et al.* (2010) [12]. In that research, detailed surface chemistry including 17 surface species and 58 surface reactions

was utilized in the simulation.

In the current study, the effect of considering homogeneous reaction mechanisms in the numerical model is investigated. Maestri and Cuoci (2013) [13] have used the open-source CFD solver OpenFOAM [15] to simulate heterogeneous catalytic systems three-dimensionally with the detailed kinetics schemes. The catalytic partial oxidation (CPOX) of methane over a honeycomb reactor was numerically studied by Hettel *et al.* (2015) [14], where OpenFOAM and DETCHEM [17] were coupled to model a large-scale COPX reactor. Table 1 illustrates a summary of the literature review, and presents the numerical studies that have been carried out in the field of catalytic partial oxidation.

Table 1 The literature review and numerical studies were carried out in the field of the catalytic combustion

Authors	Affiliation	Year	Model	Fuel/catalyst
Cerkanowicz <i>et al.</i>	Exxon Research and Engineering Co	1977	1D- simplified chemistry	Hydrogen- Pt
Markatou <i>et al.</i>	Yale University	1993	2D Boundary layer-detailed chemistry	Methane -Pt
Deutschmann <i>et al.</i>	University of Stuttgart	1994	1D- detailed chemistry	Methane -Pt
Deutschmann <i>et al.</i>	University of Heidelberg	1996	1D- detailed chemistry	Methane -Pd
O. Deutschmann, L. D. Schmidt	University of Minnesota	1998	2D - detailed chemistry	Methane- Rh- Pt
Dogwiler <i>et al.</i>	Paul Scherrer Institute	1999	2D - detailed chemistry	Methane - Pt
Raja <i>et al.</i>	Colorado School of Mines	2000	2D- detailed chemistry	Methane -Pt
Deutschmann <i>et al.</i>	University of Heidelberg	2000	2D - detailed chemistry	Methane -Pt
Dupont <i>et al.</i>	University of Leeds	2001	1D- detailed chemistry	Methane -Pt
Kramer <i>et al.</i>	University of Maryland	2002	1D- detailed chemistry	Hydrogen -Pt
Minh	University of Heidelberg	2005	2D- detailed chemistry-optimization	Ethane-Pt
Minh <i>et al.</i>	Karlsruhe Institute of Technology	2008	2D- detailed chemistry-optimization	Ethane-Pt
Kumar	Ohio State University	2009	3D- detailed chemistry	Methane -Pt
Hartmann <i>et al.</i>	Karlsruhe Institute of Technology	2010	2D- detailed chemistry	Iso-octane-Rh
Maestri and Cuoci	Politecnico di Milano	2013	3D- detailed chemistry	Iso-octane-Rh
Hettel <i>et al.</i>	Karlsruhe Institute of Technology	2013	3D - detailed chemistry	Methane - Rh
Hettel <i>et al.</i>	Karlsruhe Institute of Technology	2015	3D- detailed chemistry	Methane- Rh

Computational fluid dynamics (CFD) methods are generally classified as two distinct families of schemes: pressure-based and density-based methods. The pressure-based algorithm solves the momentum and pressure correction equations separately. The density-based solver solves the governing equations of continuity, momentum, energy and species transport simultaneously. In the density-based approach, the velocity field is obtained from the momentum equations and the continuity equation is used to obtain the density field. The pressure field is determined from the equation of state using computed flow field variables. In pressure-based methods, since there is no independent equation for pressure, a special treatment is required in order to achieve velocity-pressure coupling and enforcing mass conservation. Traditionally, pressure-based approaches were developed for low-speed incompressible flows, while density-based approaches were mainly used for high-speed compressible flows. However, this separation has been blurred in recent times as both methods have been extended and reformulated to solve a wide range of flow conditions beyond their original intent. As the majority of work involving simulation of the catalytic combustion uses pressure-based schemes; relatively less research has been performed in this field using fully coupled density-based methods. Kumar (2009) [5] and [17] studied catalytic combustion with a coupled model for species equations, but the flow solution was solved separately. In the current work, the potential of using the density-based approach for solving chemically reacting flow inside a catalytic reactor is investigated. Since all governing equations including species, momentum and energy are solved simultaneously, very accurate solutions are obtained. One of the drawbacks of the density-based method is that the system of equations becomes very stiff at low velocity. This problem may be mitigated by using appropriate preconditioners.

Many researchers have numerically studied the effects of reactor parameters, such as the

velocity inlet, temperature, and fuel concentration, on the performance of catalytic systems. In those works, the dependency of reactor performance on different design variables was obtained via parametric studies. That is, simulating the reactor performance at baseline values, then systematically changing the parameter values and reevaluating the performance. This method provides valuable information for reactor design. However, when the number of design variables is large, this procedure may become computationally prohibitive. Furthermore, utilizing parametric studies to investigate design alternatives has proven extremely valuable in practice, but this process does not provide a direct nor rigorous manner in which to arrive at an optimal design. This is the underlying motivation for the combination of computational fluid dynamics with numerical optimization methods. Moreover, the use of sensitivity analysis represents a more computationally efficient alternative for parametric studies as well as for optimization purposes. To this end, Minh (2005) [17] developed numerical methods for the simulation and optimization of complex processes in catalytic monoliths for two practical applications: catalytic partial oxidation of methane and conversion of ethane to ethylene. In that work, the optimization was formulated as an optimal control problem constrained by a system of PDEs describing the chemical fluid dynamics process. Minh *et al.* (2008) [18] then investigated the optimization of the oxidative dehydrogenation of ethane to ethylene over platinum using this optimal control problem. In that study, a two-dimensional model was used to simulate the single monolith channel.

In this research, a three-dimensional fully implicit unstructured model is developed to simultaneously solve the transport of mass, momentum, energy and species in a methane reformer. The surface chemistry is solved using the mean-field approximation model to obtain the surface coverages and reaction rates. Effects of the different parameters on the reactor

performance are investigated. The sensitivity derivatives are computed using three different approaches: finite difference, direct differentiation and adjoint method. The fuel reactor is numerically optimized using gradient-based algorithms. The simulation is performed for two different honeycomb-structured reactors. The governing equations for fluid and solid regions of the monolith are simultaneously solved considering the catalytic combustion at their interface. The performance of the reforming reactor is numerically studied. Sensitivity derivatives of objective functions representing the outlet concentration are obtained with respect to the design parameters using a discrete adjoint method.

CHAPTER 2

GOVERNING EQUATIONS AND NUMERICAL SOLUTION

The time-dependent Reynolds Averaged Navier-Stokes equations for chemically reacting flows can be written in the conservative form as:

$$\frac{\partial \vec{Q}}{\partial t} + \nabla \cdot (\vec{F}_e(\vec{Q}) - \vec{F}_v(\vec{Q})) = \vec{S}(\vec{Q}) \quad (1)$$

The conservative flow variables \vec{Q} , the inviscid flux vector \vec{F}_e , the viscous flux vector \vec{F}_v and the source term vector S are defined as:

$$\vec{Q} = \begin{bmatrix} \rho_1 \\ \rho_2 \\ \vdots \\ \rho_{ns} \\ \rho u \\ \rho v \\ \rho w \\ \rho e_t \end{bmatrix} \quad (2)$$

$$\vec{F}_e = \begin{bmatrix} \rho_1 u \\ \rho_2 u \\ \vdots \\ \rho_{ns} u \\ \rho u^2 + p \\ \rho uv \\ \rho uw \\ (\rho e_t + p)u \end{bmatrix} \hat{i} + \begin{bmatrix} \rho_1 v \\ \rho_2 v \\ \vdots \\ \rho_{ns} v \\ \rho uv \\ \rho v^2 + p \\ \rho vw \\ (\rho e_t + p)v \end{bmatrix} \hat{j} + \begin{bmatrix} \rho_1 w \\ \rho_2 w \\ \vdots \\ \rho_{ns} w \\ \rho uw \\ \rho wv \\ \rho w^2 + p \\ (\rho e_t + p)w \end{bmatrix} \hat{k} \quad (3)$$

$$\vec{F}_v = \begin{bmatrix} J_{1x} \\ J_{2x} \\ \vdots \\ J_{nsx} \\ \tau_{xx} \\ \tau_{xy} \\ \tau_{xz} \\ u\tau_{xx} + v\tau_{xy} + w\tau_{xz} - \hat{q}_x \end{bmatrix} \hat{i} + \begin{bmatrix} J_{1y} \\ J_{2y} \\ \vdots \\ J_{nsy} \\ \tau_{xy} \\ \tau_{yy} \\ \tau_{yz} \\ u\tau_{xy} + v\tau_{yy} + w\tau_{yz} - \hat{q}_y \end{bmatrix} \hat{j} + \begin{bmatrix} J_{1z} \\ J_{2z} \\ \vdots \\ J_{nsz} \\ \tau_{zx} \\ \tau_{zy} \\ \tau_{zz} \\ u\tau_{zx} + v\tau_{zy} + w\tau_{zz} - \hat{q}_z \end{bmatrix} \hat{k} \quad (4)$$

$$\vec{S} = \begin{bmatrix} \dot{\omega}_1 \\ \dot{\omega}_2 \\ \vdots \\ \dot{\omega}_{ns} \\ 0 \\ 0 \\ 0 \\ 0 \end{bmatrix} \quad (5)$$

The modified Stephen-Maxwell equation is used to compute the diffusion molar flux [19]:

$$\frac{N_i}{D_i^{kn}} + \sum_{\substack{j=1 \\ j \neq i}}^{ns} \frac{X_j N_i - X_i N_j}{D_{ij}} = -c_t \nabla X_i \quad (6)$$

The binary diffusion coefficients are obtained by using the Chapman–Enskog theory [20] as following:

$$D_{ij} = 1.8583e^{-7} \sqrt{\frac{T^3 \left(\frac{1}{MW_i} + \frac{1}{MW_j} \right)}{p \sigma_{ij}^2 \Omega_{ij}}} \left(m^2/s \right) \quad (7)$$

where Ω_{ij} is the collision integral value and $\sigma_{ij} = \frac{\sigma_i + \sigma_j}{2}$

The collision integral value is determined by a quadratic interpolation of the tables based on Stockmayer potentials [20]

The Knudsen diffusion coefficient is obtained by:

$$D_i^{kn} = d_{pore} \frac{2}{3} \sqrt{\frac{8R_u T}{\pi MW_i}} \quad (8)$$

The Wilke's mixing rule is used for estimation of the mixture viscosity:

$$\mu = \frac{\sum_{i=1}^{ns} X_i \mu_i}{\sum_{j=1}^{ns} X_j \Phi_{ij}} \quad (9)$$

where

$$\Phi_{ij} = \frac{1}{\sqrt{8}} \left(1 + \frac{MW_i}{MW_j} \right)^{-\frac{1}{2}} \left[1 + \left(\frac{\mu_i}{\mu_j} \right)^{\frac{1}{2}} \left(\frac{MW_j}{MW_i} \right)^{\frac{1}{4}} \right]^2$$

$$\mu_i = 2.6693 e^{-6 \frac{\sqrt{MW_i}}{\sigma_i^2 \Omega_\mu}} \frac{T}{\sigma_i^2 \Omega_\mu}$$

The governing equations are discretized using the finite volume method on an unstructured mesh. The computational domain is subdivided into a series of non-overlapping elements. The integral form of the governing equations can be written in the form:

$$\oint_{\Omega} [\phi] \left(\frac{\partial \vec{Q}}{\partial t} + \nabla \cdot (\vec{F}_e(\vec{Q}) - \vec{F}_v(\vec{Q}) - \vec{S}(\vec{Q})) \right) d\Omega = 0 \quad (10)$$

where ϕ is a weighted function and Ω is an arbitrary volume.

The governing equations are discretized using a node-centered finite volume method on an unstructured mesh. That is, the field is discretized into control volumes defined by the median dual centered on the mesh point vertices as shown in Figure 4 for two-dimensions. In three dimensions, the faces of the control volume are formed by the lines connecting the midpoints of the mesh edges to the centroids of the elements formed by the edges. A Green-Gauss formula is used for gradient evaluation at vertices, which results in second-order spatial accuracy.

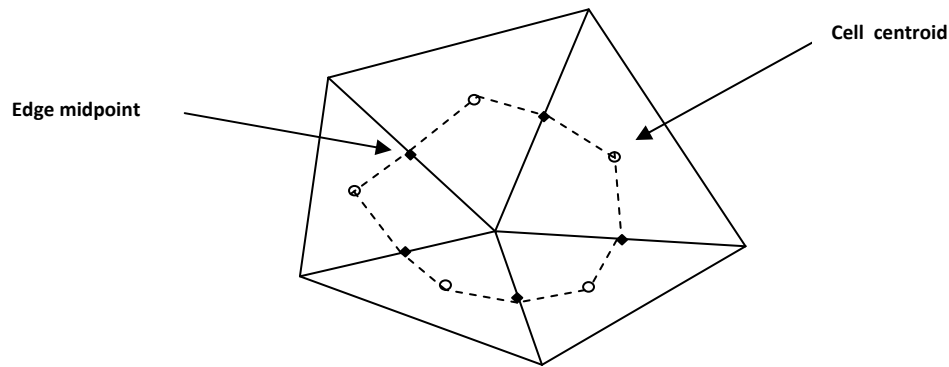


Figure 4 Control Volume based on Median Dual

The residual for each control volume is approximated by quadrature of the fluxes passing through the boundaries of the control volume faces. The convective flux terms are calculated using the Roe scheme [21]:

$$\vec{F}_e = \frac{1}{2}(F(Q_L) + F(Q_R)) - \frac{1}{2}|\tilde{A}(Q_R, Q_L)|(Q_R - Q_L) \quad (11)$$

where $|\tilde{A}| = \tilde{R}|\tilde{\Lambda}|\tilde{R}^{-1}$, \tilde{R} is matrix of right eigenvectors of the Roe averaged flux Jacobian, and $\tilde{\Lambda}$ is diagonal matrix of eigenvalues of the Roe averaged flux Jacobian. The Roe averaged variables are constructed using a density weighted average of the flow variables on either side of the control volume face for a multi species mixture [22]. The Roe averaged flux Jacobian is computed using the eigensystem described in references [22] and [23]. The viscous flux contribution is evaluated using the average of the flux vectors on either side of the control volume faces.:

$$\vec{F}_v = \frac{1}{2}(F_v(Q_L, \nabla Q_L) + F_v(Q_R, \nabla Q_R)) \quad (12)$$

A robust iterative solution process based on Newton's method is used to solve the coupled, non-linear partial differential equations. The discretized equations can be written in the residual form:

$$\frac{\partial Q}{\partial t} + R(Q) = 0 \quad (13)$$

where Q is the vector of independent variables and R is the spatial residuals. Using a backward Euler time discretization and a time linearization of the residual:

$$\frac{\Delta Q^n}{\Delta t} + R^n + \left[\frac{\partial R}{\partial Q}\right]^n \Delta Q^n = 0 \quad (14)$$

For an infinite time step, Newton's method in delta form is written as:

$$\left[\frac{\partial R}{\partial Q}\right]^n \Delta Q^n = -R^n \quad (15)$$

The complex Taylor series expansion (CTSE) method is used for accurate linearization of the residual to form the Jacobian derivatives $\left(\frac{\partial R}{\partial Q}\right)$ [24] [25]. There is no difference expression, and hence no subtractive cancelation error is presented in this method. Thus, in a computer implementation, the truncation error becomes negligible when the perturbation size is set equal or less than the square root of the machine zero [26]. The GMRES algorithm is utilized for the solution to the linear systems arising at each Newton iteration [27]. An ILU(K) preconditioner is used to improve convergence of the linear solver.

Parallelization of the solution algorithm is afforded via Message Passing Interface (MPI) libraries. METIS [28] is utilized to decompose the computational domain and create the sub-domain connectivity for parallel communications.

2. 1. MODELING THE SURFACE CHEMISTRY

The heterogeneous and homogeneous chemical reaction mechanisms are key components of reacting flow modeling. The mechanism of heterogeneously catalyzed gas-phase reactions can be described by the sequence of elementary reaction steps including adsorption, surface diffusion, chemical transformations of adsorbed species, and desorption. Several modeling approaches are available to compute the reaction rates of heterogeneous reactions. These methods are summarized in Figure 5:

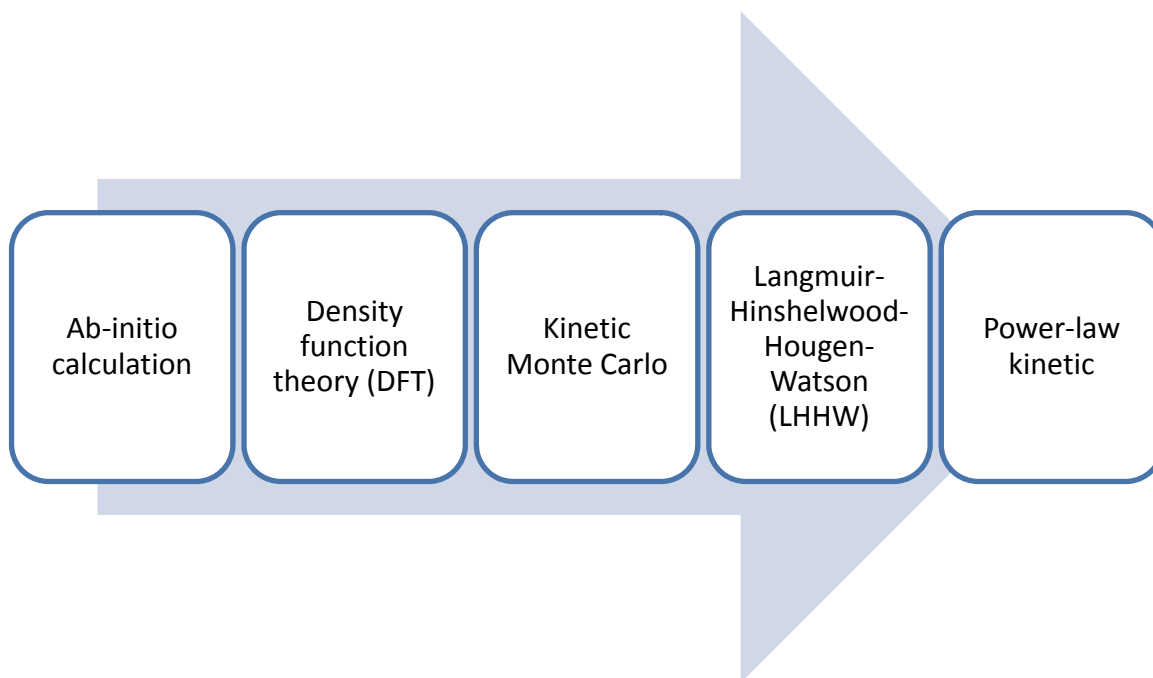


Figure 5 Methods for modeling the chemical reaction rate of heterogeneous reactions

Different approaches, such as Ab-initio calculation, density function theory (DFT), and kinetic Monte Carlo modeling have been used to include the molecular aspects of heterogeneous catalysis. In the power-law kinetic approach, the rate of the catalytic reaction is calculated by fitting empirical equations to experimental data. In the last two decades mean-field approximation has been used to improve upon the much simpler Langmuir-Hinshelwood or power-law approaches. Additionally, this approximation permits the elementary aspects of catalysis for models suitable for numerical simulation of catalytic reactors [2]. In the mean-field approximation, rate equations similar to homogeneous reactions are used to model heterogeneous reactions. In the next section, a brief explanation of the modeling of the homogeneous reactions is given, and then the simulation of the heterogeneous reactions will be reviewed.

2.1.1 GAS-PHASE CHEMISTRY MODEL

Chemical reactions in the gas phase lead to source terms R_i that are given as the mass rate of creation and depletion of species i by chemical reactions. The chemical source terms R_i are given as:

$$R_i = M_i \sum_{k=1}^{K_g} v_{ik} k_{fk} \prod_{j=1}^{N_g} [X_j]^{v_{jk}'} \quad (i = 1, \dots, N_g) \quad (16)$$

where M_i is the molar mass of species i , K_g is the number of elementary gas-phase reactions, v_{ik} (right side minus left side of reaction equation) and v_{jk}' (left side of reaction equation) are stoichiometric coefficients, k_{fk} is the forward rate coefficient and $[X_j]$ is the concentration of species j . The temperature dependence of the rate coefficients is described by a modified Arrhenius expression:

$$k_{fk} = A_k T^{\beta_k} \exp \left[\frac{-E_{a_k}}{RT} \right] \quad (17)$$

with A_k as preexponential factor, β_k as temperature coefficient, E_{a_k} as activation energy, and R as the gas constant.

Because the chemical reaction systems are stiff, a direct calculation of the chemical source terms R_i , by equation (16), using the given temperature and concentrations, may easily lead to divergence or oscillations of the iterative solution procedure. Therefore, a pseudo-time integration is usually used to calculate the chemical source term.

Since the chemical source terms have to be calculated for each fluid cell and for each iteration step, the total CPU time needed to achieve convergence increases dramatically if detailed gas-phase chemistry is used.

2.1.2 SURFACE CHEMISTRY MODEL

The range of kinetic and transport processes that can take place at a reactive surface are shown schematically in Figure 6. Heterogeneous reactions are fundamental in describing mass and energy balances that form boundary conditions in reacting flow calculations.

There are three types of chemical species that describe the heterogeneous reactions:

- Species in the gas phase (gas species(g))
- Species residing at the interface of gas and solid (surface species(s))
- Species residing within the bulk solid (below the gas-surface interface) (bulk species(b))

The surface species are those that are adsorbed on the top mono-atomic layer of the catalytic particle while the bulk species are those found in the inner solid catalyst.

Each surface species occupies one or more surface sites. A site is considered to be a location or position on the surface at which a species can reside. The total number of sites per unit area is considered a property of the material surface, and is often assumed to remain constant (site density).

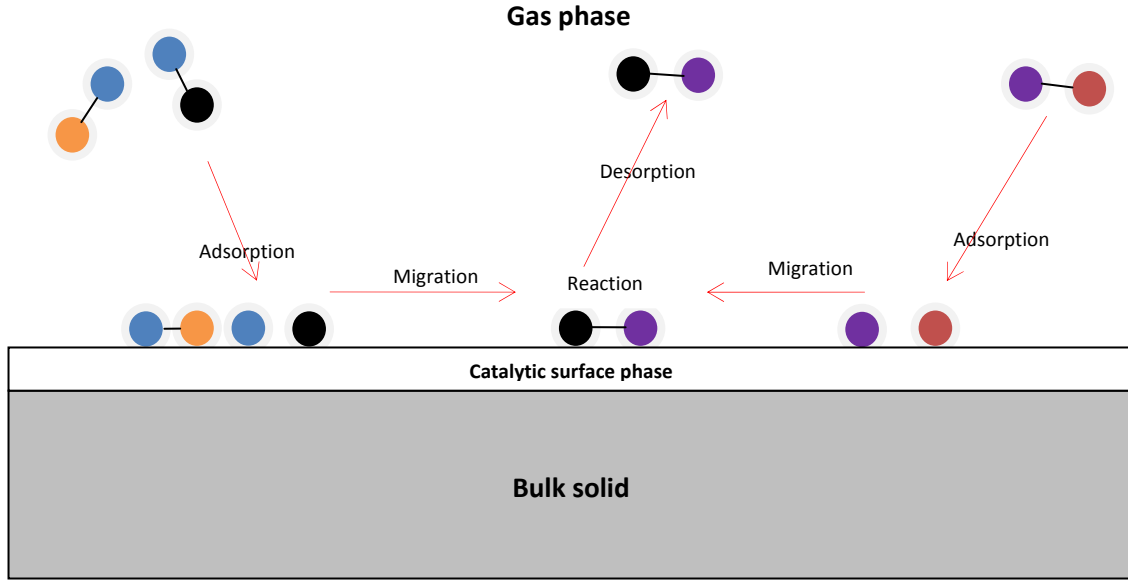


Figure 6 Schematic of the coupling between the gas and the surface due to transport and heterogeneous chemistry

Chemical kinetic rate expressions need to include the concentrations of the chemical species. For gas-phase species the molar concentration X_i (mol/m³) is written:

$$[X_i] = \frac{Y_i \rho}{M_i} \quad (i = 1, \dots, N_g) \quad (18)$$

where the Y_i are the mass fractions, ρ is the gas-phase mass density.

The composition of surface phases can be specified in terms of surface coverages θ . The surface coverages in each phase are normalized:

$$\sum_{i=N_g+1}^{N_g+N_s} \theta_i = 1 \quad (19)$$

The surface molar concentration of a species is then

$$[X_i] = \theta_i \Gamma \quad (i = N_g + 1, \dots, N_g + N_s) \quad (20)$$

where Γ is the surface site density (mol/m²) which describes the maximum number of species that can adsorb on a unit surface area. The surface site densities are of the order of 10⁻⁹ mol/cm² (approximately 10¹⁵ adsorption sites per cm²) [29].

The surface chemistry is also modeled by elementary reactions similar to the gas-phase reaction model. The chemistry source terms, \dot{s}_i , of gas-phase species due to adsorption/desorption and surface species (adsorbed species) are given by:

$$\dot{s}_i = \sum_{k=1}^{K_s} v_{ik} k_{f_k} \prod_{j=1}^{N_g+N_s} [X_j]^{v_{jk'}} \quad (i = 1, \dots, N_g + N_s) \quad (21)$$

where K_s is the number of elementary surface reactions (including adsorption and desorption), and N_s is the number of species adsorbed. The heterogeneous flux on the surface is obtained by:

$$Flux_{het} = MW_i \dot{s}_i \quad (22)$$

Since the catalyst is dispersed as small particles in the reactor support, the active catalyst area is usually much greater than the geometric surface area. The ratio of these two values is defined as:

$$F_{cat/geo} = \frac{A_{catalyst}}{A_{geometric}} \quad (23)$$

To accounting for the pore diffusion within the catalyst coating layer, the effectiveness factor, η , is defined. $F_{cat/geo}$ and η are experimentally determined. Therefore, the heterogeneous flux formula can be written as:

$$Flux_{het} = F_{cat/geo} \eta MW_i \dot{s}_i \quad (24)$$

The temperature dependence of the rate coefficients in equation (21) is described by a modified Arrhenius expression:

$$k_{fk} = A_k T^{\beta_k} \exp \left[\frac{-E_{a_k}}{RT} \right] \prod_{i=1}^{N_s} \Theta_i^{\mu_{ik}} \exp \left[\frac{\epsilon_{ik} \Theta_i}{RT} \right] \quad (25)$$

For some simple surface reaction mechanisms it is convenient to specify the surface reaction rate constant in terms of a “sticking coefficient” (probability), rather than an actual reaction rate. This approach is only allowed when there is exactly one gas-phase species reacting with a surface:

$$k_{fk} = \frac{S_i^0}{\Gamma^\tau} \sqrt{\frac{RT}{2\pi M_i}} \quad S_i^0 = \frac{S_i}{1 - \frac{S_i}{2}} \quad (26)$$

where S_i^0 is the initial (uncovered surface) sticking coefficient, τ is sum of surface reactants' stoichiometric coefficients.

Using equation (25), equation (21) can be rewritten as:

$$\dot{s}_i = \sum_{k=1}^{K_s} v_{ik} \left(A_k T^{\beta_k} \exp \left[\frac{-E_{a_k}}{RT} \right] \prod_{i=1}^{N_s} \Theta_i^{\mu_{ik}} \exp \left[\frac{\epsilon_{ik} \Theta_i}{RT} \right] \right) \prod_{j=1}^{N_g + N_s} [X_j]^{v_{jk}'} \quad (i = 1, \dots, N_g + N_s) \quad (27)$$

From equation (20), $\dot{s}_i = \frac{\delta[X_i]}{\delta t} = \frac{\delta \Theta_i}{\delta t} \Gamma$ and:

$$\frac{\delta \Theta_i}{\delta t} = \frac{\dot{s}_i}{\Gamma} \quad (28)$$

Note, equation (28) assumes that the total surface site density Γ is constant.

The equation above is used for a transient simulation. In a steady-state calculation, surface species concentrations (or site fractions) remain constant with time [30], which gives:

$$\dot{s}_i = 0 \quad (i = N_g + 1, \dots, N_g + N_s) \quad (29)$$

At steady-state the surface species concentrations have to adjust themselves consistent with the adjacent gas-phase species concentrations such that the condition $\dot{s}_i = 0$ is satisfied. In a steady-state reacting flow simulation, the surface-species governing equations are taken to be [20]:

$$\begin{cases} \dot{s}_i = 0 & (i = N_g + 1, \dots, N_g + N_s - 1) \\ \sum_{i=N_g+1}^{N_g+N_s} \theta_i = 1 \end{cases} \quad (30)$$

$$\begin{cases} \sum_{k=1}^{K_s} v_{ik} \left(A_k T^{\beta_k} \exp \left[\frac{-E_{a_k}}{RT} \right] \prod_{i=1}^{N_s} \left(\frac{[X_i]}{\Gamma} \right)^{\mu_{ik}} \exp \left[\frac{\epsilon_{ik} \left(\frac{[X_i]}{\Gamma} \right)}{RT} \right] \right) \prod_{j=1}^{N_g+N_s} [X_j]^{v_{jk}'} = 0 \\ (i = N_g + 1, \dots, N_g + N_s - 1) \end{cases} \quad (31)$$

$$\sum_{i=N_g+1}^{N_g+N_s} \left(\frac{[X_i]}{\Gamma} \right) = 1 \quad (32)$$

A normalization condition, equation (32), is used for one of the surface species to make the system of equations well-posed.

The solution of equations (31) and (32) provides the surface coverages and the surface molar concentrations. Once these have been obtained, the chemistry source terms can be computed.

The system of equations generated by equations (31) and (32) is considered to be extremely stiff. A system of ODEs is stiff if it forces the method to employ a discretization step size excessively small with respect to the smoothness of the exact solution [31]. The Jacobian

matrix of a stiff system of ODEs has greatly differing magnitudes. Since most chemical kinetics problems are stiff, many attempts were performed to find a stable and robust method for solving them. For time-dependent problems, implicit methods are more stable than explicit methods. The implicit time-integration methods are highly robust for time dependent problems but they provide slow convergence to a steady state solution. Newton's method provides a fast (quadratically convergent property) and robust algorithms for solving the steady state problems, but it only works when the initial guesses are within the domain of convergence. In practice, the modern solution algorithms usually use a hybrid approach that combines the advantages of both methods the implicit time-integration method and Newton's method.

In the current work, a stiff solver using the Backward Differentiation Formulae (BDF) method is developed. BDF methods with an unbounded region of absolute stability are widely used for solving stiff ODEs. There are several possible ways of using a variable step size including interpolated fixed-step BDF, fully variable-step BDF, and fixed-leading coefficient BDF. The fixed-leading coefficient (FLC) BDF is used in the current work. The main advantages of FLC BDF is that it does not suffer from the unstable behavior of the interpolated fixed-step method and the Newton iteration matrix can be reused for more steps than in a fully variable-step approach [32]. The Newton method is used for the solution of the resulting nonlinear system. The linear algebraic system is solved using GMRES. For validation of the implementation, a stiff solver software package is utilized. There are several software packages such as VODE [33] and DASSL [34] that efficiently compute and produce high-accuracy solutions for stiff system of ODEs. DASSL is based on fixed leading-coefficient BDF and can solve differential-algebraic equations as well as stiff ODEs. VODE offers fixed leading-coefficient Adams and BDF methods. The implicit formulae are solved via functional iteration or modified Newton,

depending on the option selected. Thus, this code has options for dealing with both stiff and non-stiff problems. These solvers usually automatically switch between stiff and non-stiff methods to achieve good performance. A C version of VODE, CVODE, is included in the SUNDIALS (Suite of Nonlinear and Differential/Algebraic Equation Solvers) package.

To this end, the currently developed solver and CVODE are used for solving detailed heterogeneous oxidation mechanism proposed by [35]. The surface reaction mechanism includes 24 heterogeneous reactions and 11 surface-adsorbed species. Figure 7 shows the runtime of solving the stiff ODE systems for two solvers. As indicated in the figure, CVODE is much faster than the solver developed herein. This may be due to greater optimization and faster algorithms.

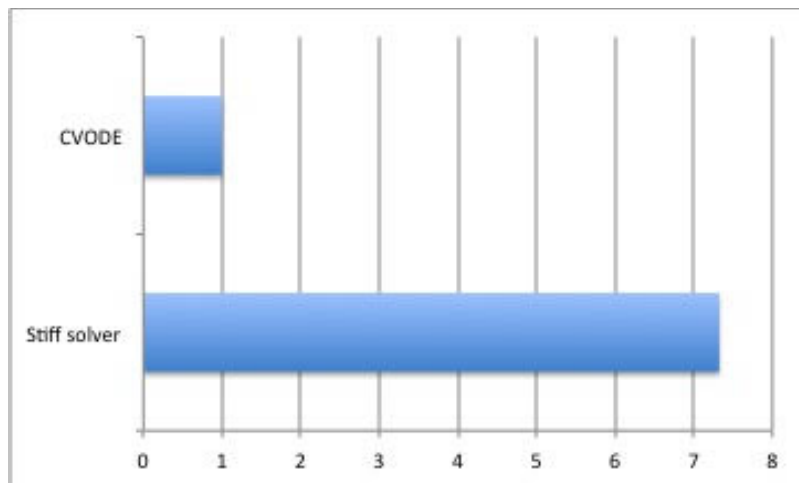


Figure 7 Normalized runtimes for solving the stiff problem

Due to this improved performance, CVODE is chosen for solving the stiff equations. For coupling the developed flow solver with CVODE, an interface based on Cantera [36] is used.

Cantera, written in C++, is a collection of object-oriented software tools for problems involving chemical kinetics, thermodynamics, and transport processes. Cantera can be used in Fortran or C++ reacting-flow simulation codes to evaluate properties and chemical source terms that appear in the governing equations with fast and efficient numerical algorithms. Cantera places no limits on the size of a reaction mechanism, or on the number of mechanisms [37].

The phase, interface definitions, and chemical reaction mechanisms are defined in a text file (cti file). For example, a cti file written for the catalytic combustion of hydrogen on palladium is shown in Appendix. 1. The cti file is converted into an XML-based format called CTML using Cantera. There are several reasons for this conversion. XML is a widely-used standard for data files, and it is designed to be relatively easy to parse. This makes it possible for other applications to use Cantera CTML data files, without requiring the substantial chemical knowledge that would be required to use cti files [36].

An interface is developed to link Cantera to the current flow solver. The structure of this interface is illustrated in Figure 8. Based on the application, a Cantera input file is written which includes the definition of the gas and surface phases and detailed chemical reactions. Input from this file is used to create and allocate the Cantera gas, surface and interface objects at the beginning of the simulation. During simulation, the flow solver provides the gas phase to Cantera. This information includes the temperature, pressure, and mole fractions of the species. Cantera specifies the required parameters, which is then provided to the CVODE solver. The surface coverages and reaction rates are computed and communicated back to the flow simulation solver to use as the chemical source terms.

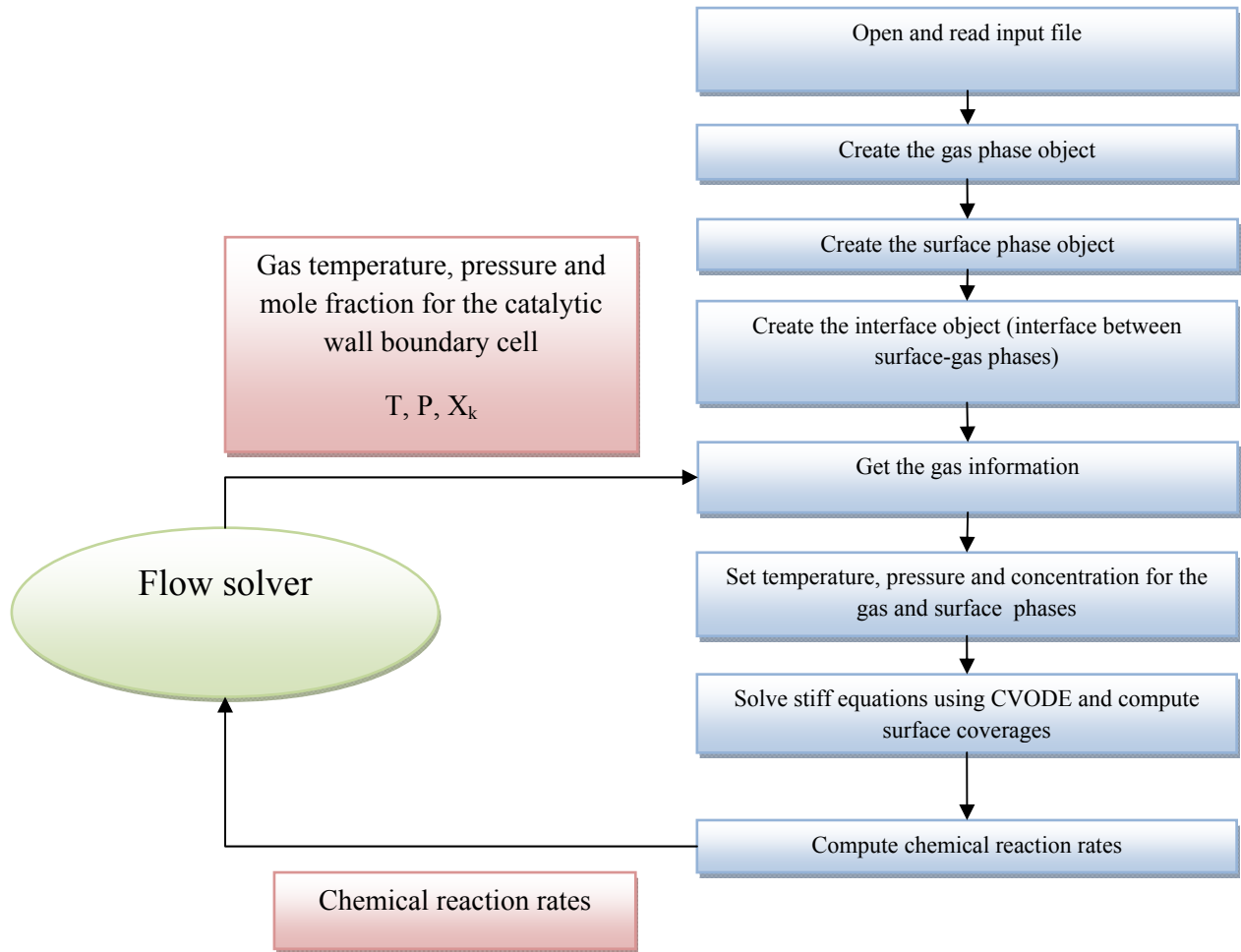


Figure 8 Data exchange between the solver and Cantera through the interface

2.2. SENSITIVITY DERIVATIVES

In many engineering design applications, sensitivity analysis techniques are useful in identifying the design parameters that have the most influence on the response quantities. This information is helpful prior to an optimization study as it can be used to remove design

parameters that do not strongly influence the responses. In addition, these techniques can provide assessments as to the behavior of the response functions which can be invaluable in algorithm selection for optimization, uncertainty quantification, and related methods. In a post-optimization role, sensitivity information is useful in determining whether or not the response functions are robust with respect to small changes in the optimum design point [38]. The sensitivities are obtained by computing gradients or derivatives of the solution with respect to the set of design variables. There are many methods for computing and obtaining sensitivities derivatives. A review of these methods may be found in [26]. Finite difference, direct differentiation and adjoint methods have been widely used in the literature for this purpose. The finite difference method is the simplest approach to compute sensitivity derivatives. For a design variable β and a cost function $I(\beta)$, the sensitivity derivatives are obtained from a central difference as following:

$$\frac{\partial I}{\partial \beta} \approx \frac{I(\beta+\Delta\beta)-I(\beta-\Delta\beta)}{2\Delta\beta} \quad (33)$$

which has a second-order truncation error and is subjected to subtractive cancellation. This method is computationally expensive for a large number of design variables because two fully converged nonlinear flow solutions are required for every design parameter.

The direct differentiation method is obtained by use of the chain rule. The residual may be expressed in terms of explicit and implicit dependencies on the design variables as:

$$R = R(\beta, \vec{Q}(\beta), X(\beta)) \quad (34)$$

Applying the chain rule yields:

$$\frac{dR}{d\beta} = \frac{\partial R}{\partial \beta} + \frac{\partial R}{\partial Q} \frac{\partial Q}{\partial \beta} + \frac{\partial R}{\partial X} \frac{\partial X}{\partial \beta} \quad (35)$$

At convergence the residual and therefore the total differential are zero, that is $dR/d\beta=0$, and therefore the above may be solved for the sensitivity of the conserved variables as:

$$\left[\frac{\partial R}{\partial Q} \right] \left\{ \frac{\partial Q}{\partial \beta} \right\} = - \frac{\partial R}{\partial \beta} \quad (36)$$

In this linear system the Jacobian and sensitivity matrices, $\partial R/\partial Q$ and $\partial R/\partial \beta$, are evaluated using the CTSE method. Applying the chain rule to the cost function, assuming in general that this function has both explicit and implicit dependencies on the design variables, yields:

$$\frac{dI}{d\beta} = \frac{\partial I}{\partial \beta} + \frac{\partial I}{\partial Q} \frac{\partial Q}{\partial \beta} \quad (37)$$

The linearization of the cost function can be evaluated analytically or by using the CTSE method. Direct differentiation requires the solution to a linear system of equations for each design variable and, thus provides an efficient method when the number of design variables is relatively small.

In the adjoint method a constraint term, which is proportional to the residual through a Lagrange multiplier [39], is added to the cost function:

$$I(\beta, \vec{Q}(\beta), X(\beta)) = I_c(\beta, \vec{Q}(\beta), X(\beta)) + \lambda^T R(\beta, \vec{Q}(\beta), X(\beta)) \quad (38)$$

where I_c is the initial cost function, λ is an arbitrary vector of Lagrange multipliers and T is the transpose operator. Linearizing the above with respect to the design variables yields:

$$\frac{dI}{d\beta} = \frac{\partial I_c}{\partial \beta} + \frac{\partial I_c}{\partial Q} \frac{\partial Q}{\partial \beta} + \frac{\partial I_c}{\partial X} \frac{\partial X}{\partial \beta} + \lambda^T \left(\frac{\partial R}{\partial Q} \frac{\partial Q}{\partial \beta} + \frac{\partial R}{\partial X} \frac{\partial X}{\partial \beta} + \frac{\partial R}{\partial \beta} \right) \quad (39)$$

Rearranging this equation to isolate the sensitivity of the conserved variables gives:

$$\frac{dI}{d\beta} = \left[\frac{\partial Q}{\partial \beta} \right]^T \left\{ \left[\frac{\partial R}{\partial Q} \right]^T \lambda + \frac{\partial I_c}{\partial Q} \right\} + \left\{ \frac{\partial I_c}{\partial \beta} + \left[\frac{\partial X}{\partial \beta} \right]^T \frac{\partial I_c}{\partial X} \right\} + \left\{ \left[\frac{\partial R}{\partial \beta} \right]^T + \left[\frac{\partial X}{\partial \beta} \right]^T \left[\frac{\partial R}{\partial X} \right]^T \right\} \lambda \quad (40)$$

Since the Lagrange multipliers are arbitrary they are chosen to eliminate the first term on the right hand side resulting in:

$$\left[\frac{\partial R}{\partial Q} \right]^T \{\lambda\} + \left\{ \frac{\partial I_c}{\partial Q} \right\} = 0 \quad (41)$$

Once the Lagrange multipliers have been obtained by solving the above linear system, sensitivity derivatives can be obtained from:

$$\frac{dI}{d\beta} = \frac{\partial I_c}{\partial \beta} + \left[\frac{\partial X}{\partial \beta} \right]^T \frac{\partial I_c}{\partial X} + \lambda^T \left\{ \left[\frac{\partial R}{\partial \beta} \right] + \left[\frac{\partial R}{\partial X} \right] \left[\frac{\partial X}{\partial \beta} \right] \right\} \quad (42)$$

As can be seen, evaluation of the Lagrange multipliers only requires solution of one linear system of equations for a given cost function. Therefore, the adjoint method is more efficient than the direct differentiation approach for a large number of design variables.

CHAPTER 3

NUMERICAL SIMULATION OF CATALYTIC COMBUSTION IN STAGNATION FLOW

Since catalytic combustion includes a complex and coupled interaction of physics and chemistry, researches usually use simple configurations to study and investigate them numerically and experimentally. The stagnation flow field over a catalytically active foil is a well-documented configuration and allows for the application of simple modeling and measurement methods for analysis and study of heterogeneous combustion. Several researches have studied the catalytic combustion of methane in a stagnation flow reactor. Deutschmann *et al.* [40] investigated the heterogeneous oxidation of methane in a stagnation point flow numerically and experimentally and obtained the ignition temperature 600°C for the case. The catalytic combustion of CH₄, CO and H₂ oxidation on platinum and palladium are studied numerically by Deutschmann and *et al.* [41]. They presented the dependence of the ignition temperature on the fuel/oxygen ratio. Dupont *et al.* [42] investigated numerically and experimentally the dependencies of the methane conversion and CO selectivity on the surface temperature for the catalytic combustion of methane on a platinum foil in a stagnation point flow reactor. Most of research that has been done in the literature is related to the catalytic combustion of methane. In this chapter, we first study methane oxidation on a platinum surface. After the validation of numerical results with experimental data, the ignition temperature and the effects of the surface temperature on the catalytic combustion are investigated. The catalytic partial oxidation of iso-octane over a Rhodium (Rh) coated surface is considered as another test case.

Figure 9 shows the schematic of an axisymmetric stagnation-point flow. The stagnation flow can be analyzed exactly using a similarity solution approach. In a similarity solution, the number of independent variables is reduced by one using a coordinate transformation. For a incompressible flow and $\frac{L}{D} \ll 1$, the exact flow equations using a similarity solution method posses a solution with the following properties and assumptions [30]

- $u = u(z)$ (u =Axial velocity)
- $v = rV(z)$
- $T = T(z)$
- $Y_k = Y_k(z)$
- $P = P_0 + \Lambda_r \frac{r^2}{2}$ ($\Lambda_r = \frac{1}{r} \frac{dp}{dr}$ pressure-curvature term)

With these assumptions, the Navier-Stokes equations are reduced to a system of ODEs in the axial coordinate z [30]:

$$\frac{d(\rho u)}{dz} + 2\rho V = 0 \quad (\text{Mass continuity}) \quad (43)$$

$$\rho \frac{dV}{dz} = \frac{d}{dz} \left(\mu \frac{dV}{dz} \right) - \rho V^2 - \Lambda_r - \rho u \frac{dV}{dz} \quad (\text{Radial momentum}) \quad (44)$$

$$\rho \frac{dY_k}{dz} = -\rho u \frac{dY_k}{dz} - \frac{dj_k}{dz} + MW_k \dot{\omega}_k \quad (\text{Species continuity}) \quad (45)$$

$$\rho c_p \frac{dT}{dz} = -\rho c_p u \frac{dT}{dz} + \frac{d}{dz} \left(k \frac{dT}{dz} \right) - \sum_k MW_k \dot{\omega}_k h_k - \sum_k j_k c_{p_k} \frac{dT}{dz} \quad (\text{Thermal energy}) \quad (46)$$

$$p = \rho RT \sum_k \frac{Y_k}{MW_k} \quad (47)$$

where j_k is the diffusive flux, c_p is the mixture specific heat, μ is dynamic viscosity, k is thermal conductivity, MW_k is molecular weight, $\dot{\omega}_k$ is molar production rate of species k and h_k is the enthalpy of species k . The axial coordinate z is the independent variable and the axial velocity (u), the scaled radial velocity ($V = \frac{v}{r}$), the temperature (T) and mass fractions (Y_k) are dependent variables.

For the discretization of these equations, upwind differencing and central differencing are used for convective and diffusive terms respectively. A MATLAB code is written to solve these equations using a finite difference scheme. The CVODE computer program is used for the solving the ODEs equations. The interface for COVE is created by a one-dimensional module of Cantera. A hybrid Newton/time step algorithm suggested by [43] is used by Cantera to obtain the steady state solution. The solver tries to find the steady-state solution by Newton's method. If the initial guesses lie within its domain of convergence, Newton's method converges very fast. However, it is hard to find a good starting vector for initializing these highly nonlinear problems. In this case, a damping Newton's method is used to improve the convergence rate, which is well documented in [30]. Generally, two approaches, the line search method and the trust region method are used for the damping process of Newton's method. The line search parameter is adjusted at each iteration to ensure that the next vector of solution is a better approximation to the previous solution vector. This damping technique can improve the robustness but is not effective in some problems. An alternative to a line search is the trust region method, in which an estimate is maintained of the radius of a region in which the quadratic model is sufficiently accurate for the computed Newton step to be reliable, and, thus, the next approximate solution is constrained to lie within the trust region [44]. In the trust region method, both the direction and the length of the Newton step can be modified when necessary. The damping parameters are

chosen to ensure that 1) mass fractions are between zero and unity 2) the next Newton step has a smaller norm than the original undamped Newton step.

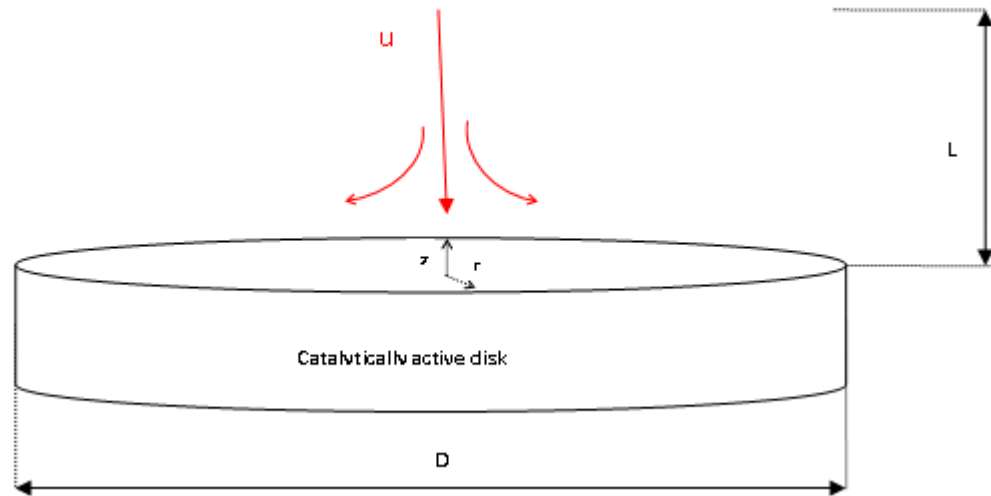


Figure 9 The schematic of stagnation-point flow

If the Newton iteration fails, the solver attempts to solve a pseudo-transient problem by adding transient terms in each conservation equation. The solution algorithm used by Cantera is illustrated in Figure 10.

The evaluation of the Jacobian matrix is the most computationally expensive operation in this algorithm. For the fast convergence, the Jacobians are not computed at each iteration and only calculated when the damped Newton algorithm fails [36].

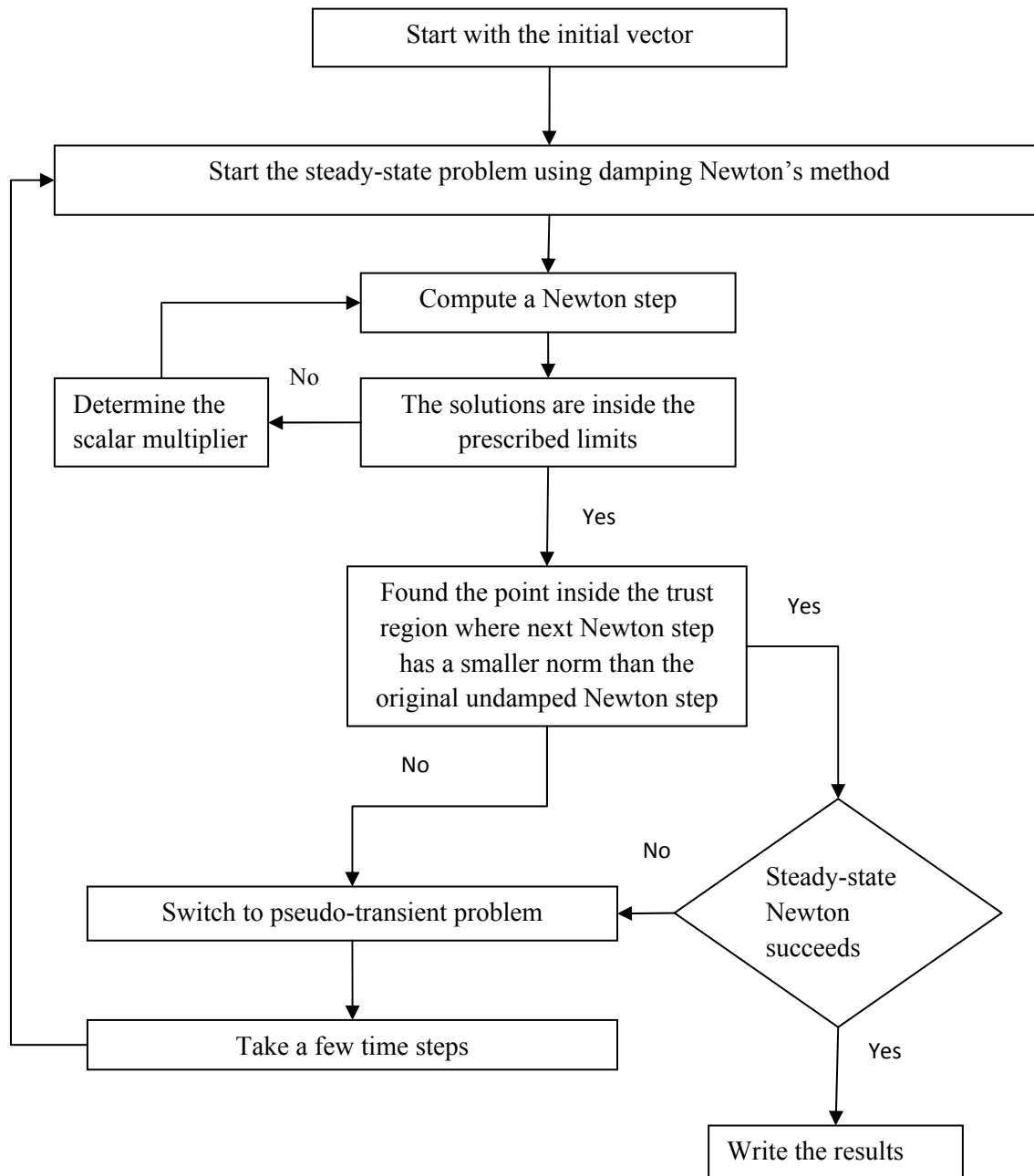


Figure 10 The solution algorithm for solving the ODE equations

3.1. METHANE OXIDATION ON A PLATINUM SURFACE

In this section, the catalytic combustion of methane on the platinum foil is investigated. This case is chosen because there are many examples in the literature that performed numerically and experimentally on this problem and it can be helpful for comparing our results with them for validation of the numerical data. As indicated in Figure 11, a lean mixture of methane-air with a uniform velocity distribution is injected at the distance 10 cm above the reactive surface. The flow field variables including density, velocity, species mole fractions and temperature are independent of radius and depend only on the distance from the surface. The boundary conditions are illustrated in Figure 11. Since there is no net mass exchange between the gas and surface, the Stefan velocity (u_{st}) is zero.

The simulations are performed with the detailed heterogeneous oxidation mechanism proposed by [41]. The surface reaction mechanism is shown in Table 2. It consists of 24 heterogeneous reactions, including 11 surface-adsorbed species. Since the ODE system of equations is stiff, a proper procedure should be used to make sure the solution is well converged. For this case, the problem is solved first for a hydrogen-oxygen case to provide a good initial estimate for methane-air test case. In addition, the solver is first run without the heterogeneous reaction rate and then the chemistry source term is added gradually. The solution is started with an initial grid with 10 nodes and refined if needed during the solution. The simulations showed that a grid with 40 nodes provides a robust and good solution.

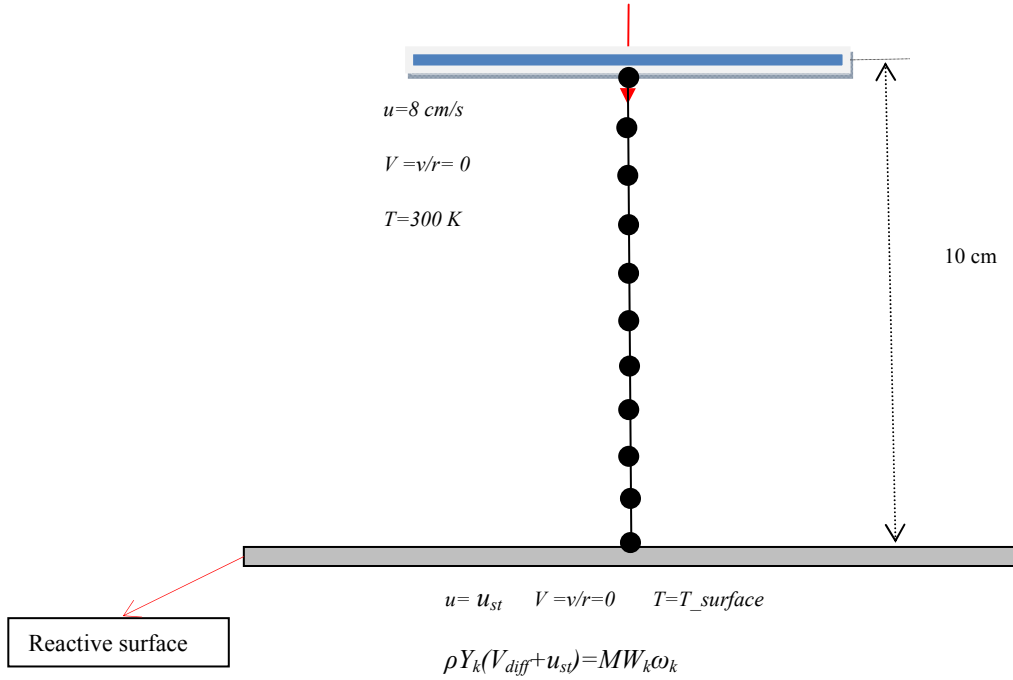


Figure 11 Geometry and boundary conditions for catalytic combustion of methane on the platinum surface

For validation of the numerical results, the experimental data provided by reference [42] is used. Figure 12 shows the comparison between the obtained numerical results with experimental data. The fuel conversion index (FCI) is defined as the ratio of fuel mass consumed to inlet mass flux of fuel [42]. As seen in Figure 12, good agreement is obtained.

The velocity and temperature profiles are indicated in Figure 13. The axial velocity is changed from the inlet value to zero on the surface. The radial velocity is increased to its maximum value near the surface and then sharply decreased to zero on the surface.

Table 2 Reaction mechanism for methane combustion on a Pt surface [6]

	Reaction	A^a	β^a	E^a
(1)	$H_2 + 2Pt(s) \rightarrow 2H(s)$ The reaction rate is first-order in Pt(s) The reaction has an equivalent sticking coefficient of 0.046	4.46×10^{10}	0.5	
(2)	$2H(s) \rightarrow H_2 + 2Pt(s)$ The reaction rate is modified by an activated H(s) coverage, ^b i.e., $k = AT^\beta \exp(-E/RT) \times \exp(-\epsilon[H(s)]/RT)$, where the activation parameter $\epsilon = -6$ kJ/mol	3.7×10^{21}		67.4
(3)	$H + Pt(s) \rightarrow H(s)$	1.00^c		
(4)	$O_2 + 2Pt(s) \rightarrow 2O(s)$	1.8×10^{21}	-0.5	
(5)	$O_2 + 2Pt(s) \rightarrow 2O(s)$ Reactions (4) and (5) represent alternative competing pathways	0.023^c		
(6)	$2O(s) \rightarrow O_2 + 2Pt(s)$ The reaction rate is modified by an activated O(s) coverage The activation parameter $\epsilon = -60$ kJ/mol	1.8×10^{21}		213.2
(7)	$O + Pt(s) \rightarrow O(s)$	1.0^c		
(8)	$H_2O + Pt(s) \rightarrow H_2O(s)$	1.0^c		
(9)	$H_2O(s) \rightarrow H_2O + Pt(s)$	1.0×10^{13}		40.3
(10)	$OH + Pt(s) \rightarrow OH(s)$	1.0^c		
(11)	$OH(s) \rightarrow OH + Pt(s)$	1.0×10^{13}		192.8
(12)	$H(s) + O(s) \leftrightarrow OH(s) + Pt(s)$	3.7×10^{21}		11.5
(13)	$H(s) + OH(s) \leftrightarrow H_2O(s) + Pt(s)$	3.7×10^{21}		17.4
(14)	$OH(s) + OH(s) \leftrightarrow H_2O(s) + O(s)$	3.7×10^{21}		48.2
(15)	$CO + Pt(s) \rightarrow CO(s)$ The reaction rate is second order in Pt(s) The reaction is equivalent to a sticking coefficient of 0.84	1.618×10^{20}	0.5	
(16)	$CO(s) \rightarrow CO + Pt(s)$	1.0×10^{13}		125.5
(17)	$CO_2(s) \rightarrow CO_2 + Pt(s)$	1.0×10^{13}		20.5
(18)	$CO(s) + O(s) \rightarrow CO_2(s) + Pt(s)$	3.7×10^{21}		105.0
(19)	$CH_4 + 2Pt(s) \rightarrow CH_3(s) + H(s)$ The reaction rate has a 2.3 order dependence on Pt(s) The reaction is equivalent to a sticking coefficient of 0.01	4.63×10^{20}	0.5	
(20)	$CH_3(s) + Pt(s) \rightarrow CH_2(s) + H(s)$	3.7×10^{21}		20.0
(21)	$CH_2(s) + Pt(s) \rightarrow CH(s) + H(s)$	3.7×10^{21}		20.0
(22)	$CH(s) + Pt(s) \rightarrow C(s) + H(s)$	3.7×10^{21}		20.0
(23)	$C(s) + O(s) \rightarrow CO(s) + Pt(s)$	3.7×10^{21}		62.8
(24)	$CO(s) + Pt(s) \rightarrow C(s) + O(s)$	1.0×10^{18}		184.0

^aArrhenius parameters for the rate constants written in the form: $k = AT^\beta \exp(-E/RT)$. The units of A are given in terms of moles, cubic meters, and seconds. E is in kJ/mol.

^bThe surface coverage (e.g., $[H(s)]$) is specified as a site fraction.

^cSticking coefficient. Total available site density for Pt is $\Gamma = 2.7 \times 10^{-9}$ mol/cm².

Catalytic ignition refers to phenomena where sufficient energy is released from a catalytic reaction to maintain further reaction without additional external heating [45]. Deutschmann *et al.* [40] experimentally obtained an ignition point around 873 K for the catalytic combustion of methane on the platinum foil. The present work investigates the behavior and changes of the heterogeneous mechanism at different temperatures around the ignition point. The effect of the surface temperature on the profile of methane mole fraction is shown in Figure 14.

At the low temperature 700 K, the methane concentration is almost constant and no methane is consumed. Increasing the surface temperature causes the methane consumption to be enhanced and at a temperature of about 1400 K, all of methane is depleted.

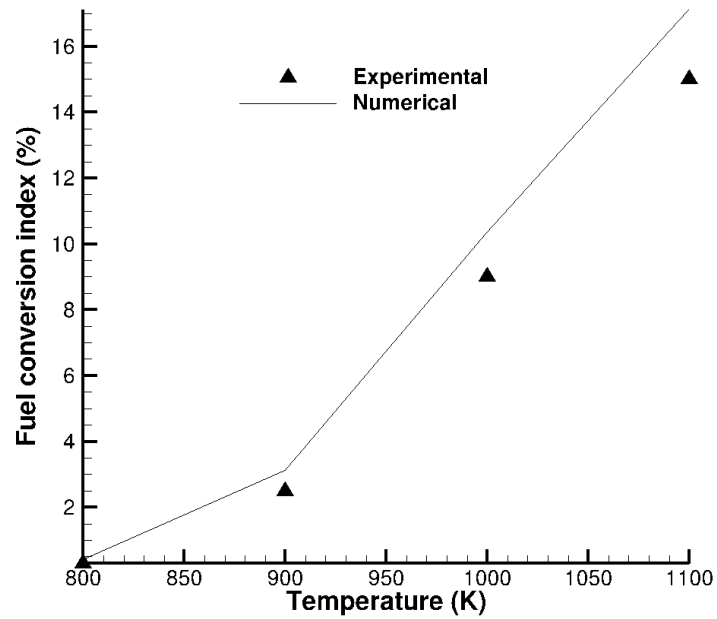


Figure 12 The comparison between the obtained numerical results with experimental data reported by [42]

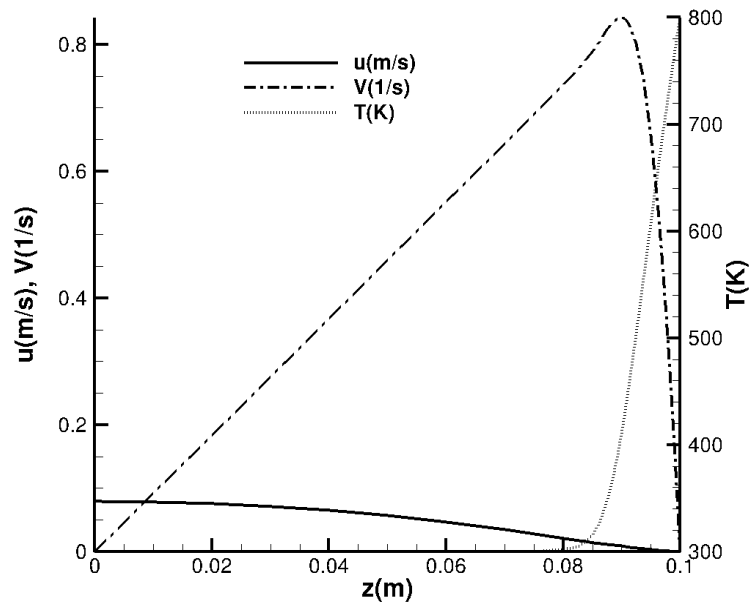


Figure 13 Velocity and temperature profiles for the surface temperature 800 K

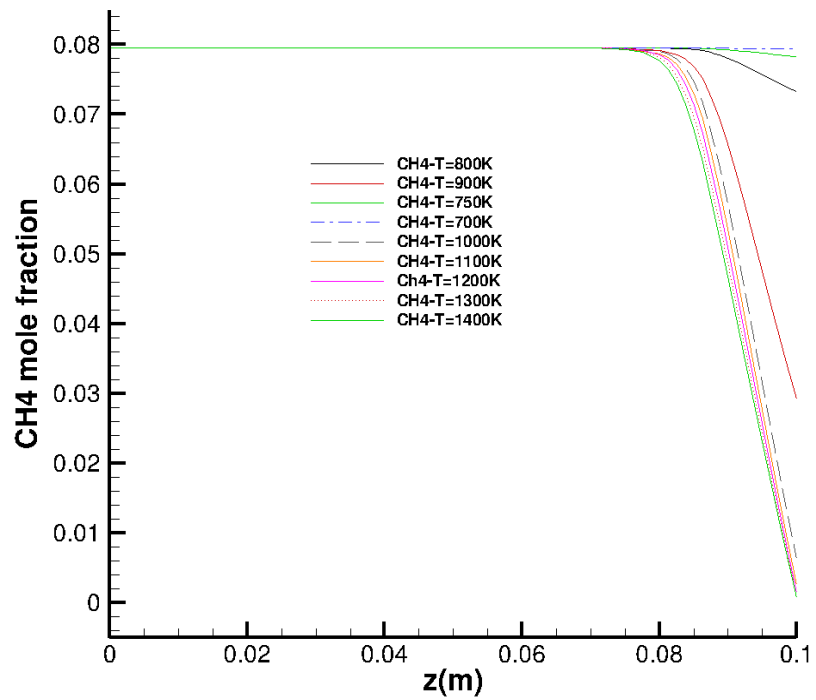


Figure 14 Effect of the surface temperature on CH4 concentration

Figure 15 shows the variation of the surface phase mass fraction with temperature. The site density is 2.7063×10^{-9} and initial coverages of the surface is $H(S) = 0.5$ and $Pt(S) = 5$. At the lower temperature, the platinum surface is mainly covered by oxygen. The oxygen coverage is decreased with increasing temperature, especially after the ignition point and $O(S)$ is consumed by the $OH(S)$ and $CO(S)$ formation reactions.

As seen in Figure 16, the main products of this heterogeneous mechanism are CO_2 and H_2O . The CH_4 and oxygen are consumed near the reactive surface and produce CO_2 and H_2O .

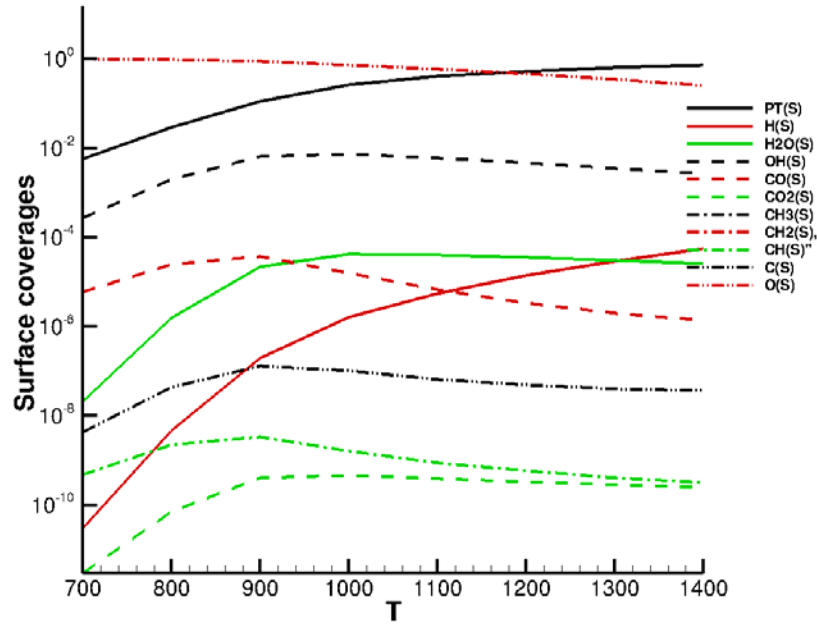


Figure 15 Surface site fraction for the different surface temperature

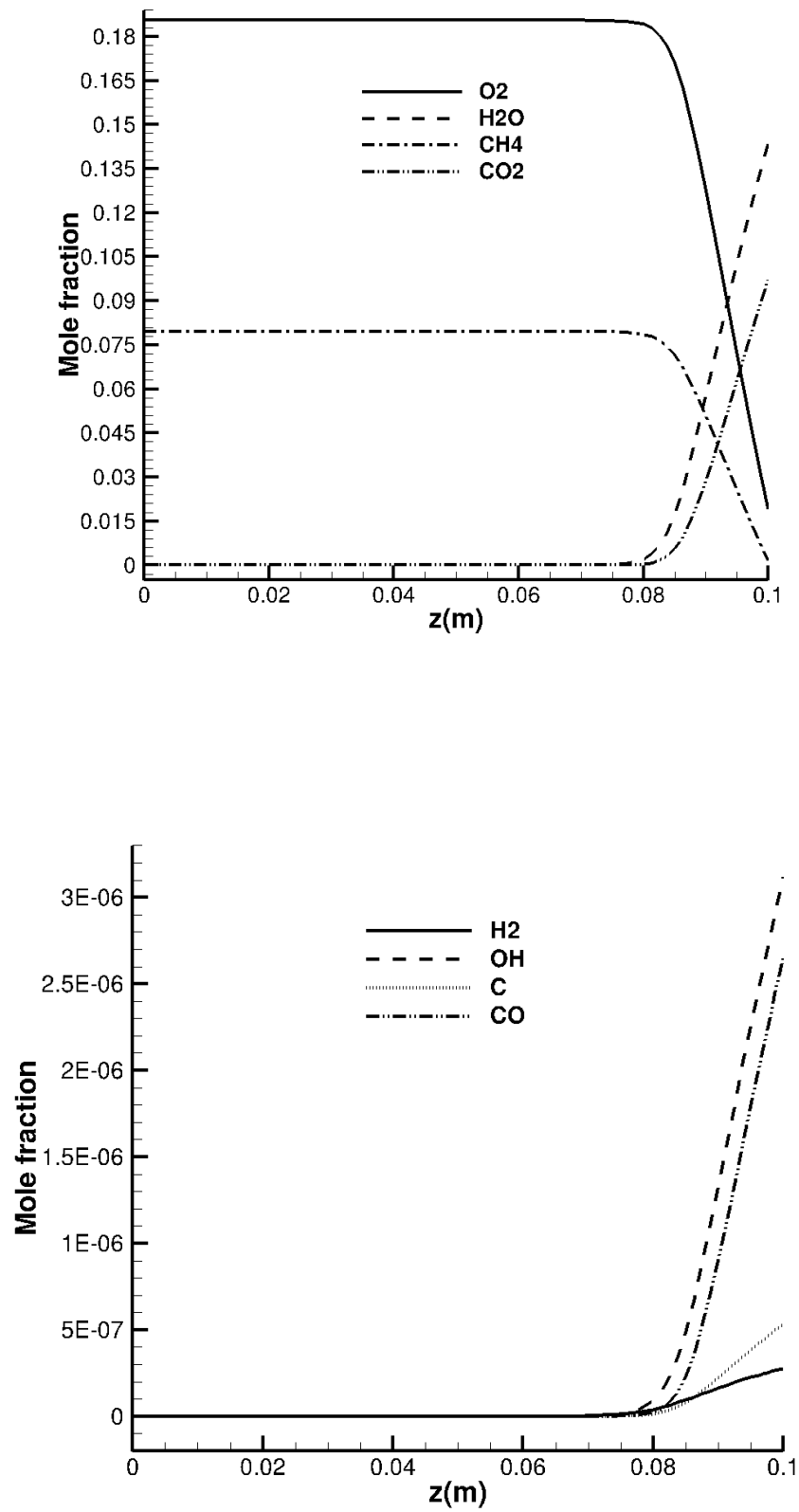


Figure 16 Gas phase species concentrations for the surface temperature 1200 K

3.2. CATALYTIC PARTIAL OXIDATION OF ISO-OCTANE OVER RHODIUM (RH) COATED SURFACE

The catalytic combustion of iso-octane over a rhodium/alumina coated honeycomb monolith is investigated as another test case. The initial and boundary conditions are given in Figure 17.

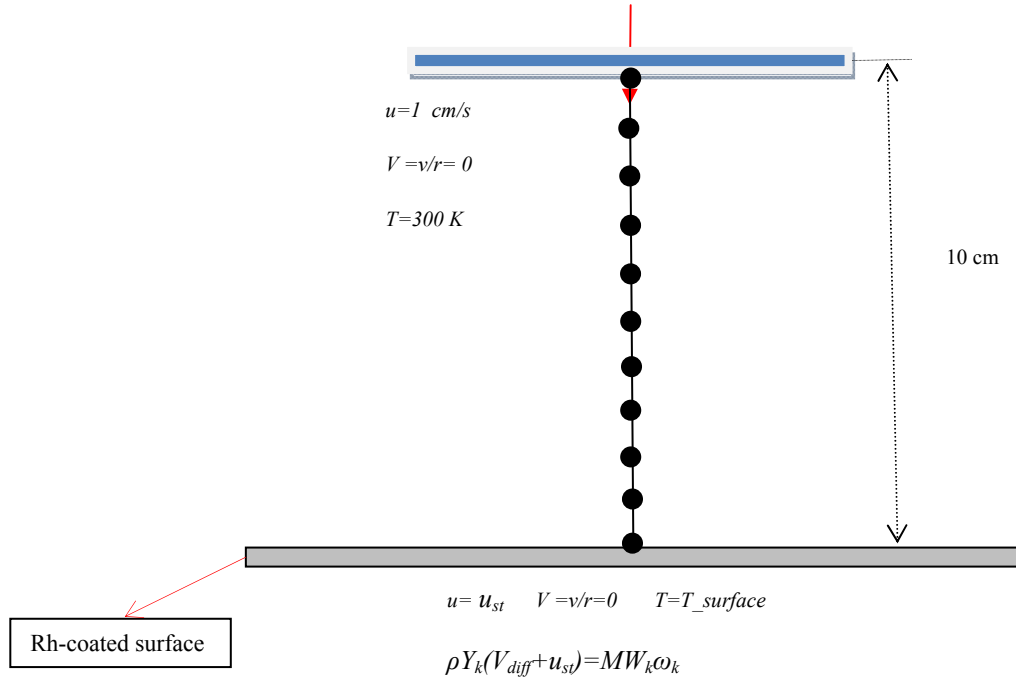


Figure 17 Geometry and boundary conditions for catalytic combustion of iso-octane over the Rhodium surface

The heterogeneous combustion of iso-octane on a rhodium-based catalyst is modeled by a detailed surface reaction mechanism proposed by Hartmann *et. al* [46]. Table 3 shows the details

of the chemistry model. The surface chemistry mechanism includes 17 surface species and 58 surface reactions.

Table 3 Reaction mechanism for iso-octane combustion on a Rh surface [12]

Reaction	A (mol cm s)	E _a (kJ mol ⁻¹)
H ₂ + 2Rh(s) → 2H(s)	1.0 × 10 ^{-02a}	0.0
O ₂ + 2Rh(s) → 2O(s)	1.0 × 10 ^{-02a}	0.0
CH ₄ + Rh(s) → CH ₄ (s)	8.0 × 10 ^{-03a}	0.0
C ₃ H ₈ + Rh(s) → C ₃ H ₈ (s)	5.8 × 10 ^{-03a}	0.0
H ₂ O + Rh(s) → H ₂ O(s)	1.0 × 10 ^{-01a}	0.0
CO ₂ + Rh(s) → CO ₂ (s)	1.0 × 10 ^{-05a}	0.0
CO + Rh(s) → CO(s)	5.0 × 10 ^{-01a}	0.0
2H(s) → 2Rh(s) + H ₂	3.0 × 10 ²¹	77.8
2O(s) → 2Rh(s) + O ₂	1.3 × 10 ²²	355.2-280θ _{O(s)} ^b
H ₂ O(s) → H ₂ O + Rh(s)	3.0 × 10 ¹³	45.0
CO(s) → CO + Rh(s)	3.5 × 10 ¹³	133.4-15θ _{CO(s)} ^b
CO ₂ (s) → CO ₂ + Rh(s)	1.0 × 10 ¹³	21.7
CH ₄ (s) → CH ₄ + Rh(s)	1.0 × 10 ¹³	25.1
C ₃ H ₈ (s) → C ₃ H ₈ + Rh(s)	1.0 × 10 ¹³	30.1
C ₃ H ₈ (s) + Rh(s) → C ₃ H ₇ (s) + H(s)	3.7 × 10 ²¹	55.0
C ₃ H ₇ (s) + H(s) → C ₃ H ₈ (s) + Rh(s)	3.7 × 10 ²¹	56.6
C ₃ H ₇ (s) + Rh(s) → C ₃ H ₆ (s) + H(s)	3.7 × 10 ²⁴	73.4
C ₃ H ₆ (s) + H(s) → C ₃ H ₇ (s) + Rh(s)	3.7 × 10 ²¹	75.9
C ₃ H ₈ (s) + O(s) → C ₃ H ₇ (s) + OH(s)	1.7 × 10 ²⁴	71.5
C ₃ H ₇ (s) + OH(s) → C ₃ H ₈ (s) + O(s)	3.7 × 10 ²¹	31.3
C ₃ H ₇ (s) + O(s) → C ₃ H ₆ (s) + OH(s)	3.7 × 10 ²⁴	88.7
C ₃ H ₆ (s) + OH(s) → C ₃ H ₇ (s) + O(s)	3.7 × 10 ²¹	45.3
C ₃ H ₆ (s) + Rh(s) → C ₂ H ₃ (s) + CH ₃ (s)	3.7 × 10 ²⁴	83.7
C ₂ H ₃ (s) + CH ₃ (s) → C ₃ H ₆ (s) + Rh(s)	3.7 × 10 ²¹	55.8
C ₂ H ₃ (s) + Rh(s) → C(s) + CH ₃ (s)	3.7 × 10 ²¹	35.6
C(s) + CH ₃ (s) → C ₂ H ₃ (s) + Rh(s)	3.7 × 10 ²¹	118.7
CH ₄ (s) + Rh(s) → CH ₃ (s) + H(s)	3.7 × 10 ²¹	61.0
CH ₃ (s) + H(s) → CH ₄ (s) + Rh(s)	3.7 × 10 ²¹	51.0
CH ₃ (s) + Rh(s) → CH ₂ (s) + H(s)	3.7 × 10 ²⁴	103.0
CH ₂ (s) + H(s) → CH ₃ (s) + Rh(s)	3.7 × 10 ²³	44.1
CH ₂ (s) + Rh(s) → CH(s) + H(s)	3.7 × 10 ²⁴	100.0
CH(s) + H(s) → CH ₂ (s) + Rh(s)	3.7 × 10 ²¹	68.0
CH(s) + Rh(s) → C(s) + H(s)	3.7 × 10 ²¹	21.0
C(s) + H(s) → CH(s) + Rh(s)	3.7 × 10 ²¹	172.8
CH ₄ (s) + O(s) → CH ₃ (s) + OH(s)	1.7 × 10 ²⁴	80.3
CH ₃ (s) + OH(s) → CH ₄ (s) + O(s)	3.7 × 10 ²¹	24.3
CH ₃ (s) + O(s) → CH ₂ (s) + OH(s)	3.7 × 10 ²⁴	120.3
CH ₂ (s) + OH(s) → CH ₃ (s) + O(s)	3.7 × 10 ²¹	15.1
CH ₂ (s) + O(s) → CH(s) + OH(s)	3.7 × 10 ²⁴	114.5
CH(s) + OH(s) → CH ₂ (s) + O(s)	3.7 × 10 ²¹	36.8
CH(s) + O(s) → C(s) + OH(s)	3.7 × 10 ²¹	30.1
C(s) + OH(s) → CH(s) + O(s)	3.7 × 10 ²¹	136.0
H(s) + O(s) → OH(s) + Rh(s)	5.0 × 10 ²²	83.7
OH(s) + Rh(s) → H(s) + O(s)	3.0 × 10 ²⁰	33.7
H(s) + OH(s) → H ₂ O(s) + Rh(s)	3.0 × 10 ²⁰	33.5
H ₂ O(s) + Rh(s) → H(s) + OH(s)	5.0 × 10 ²²	106.4
OH(s) + OH(s) → H ₂ O(s) + O(s)	3.0 × 10 ²¹	100.8
H ₂ O(s) + O(s) → OH(s) + OH(s)	3.0 × 10 ²¹	171.8
C(s) + O(s) → CO(s) + Rh(s)	5.2 × 10 ²³	97.9
CO(s) + Rh(s) → C(s) + O(s)	2.5 × 10 ²¹	169.0
CO(s) + O(s) → CO ₂ (s) + Rh(s)	5.5 × 10 ¹⁸	121.6
CO ₂ (s) + Rh(s) → CO(s) + O(s)	3.0 × 10 ²¹	115.3
CO(s) + H(s) → HCO(s) + Rh(s)	5.0 × 10 ¹⁹	108.9
HCO(s) + Rh(s) → CO(s) + H(s)	3.7 × 10 ²¹	0.0 + 50θ _{CO(s)} ^b
HCO(s) + Rh(s) → CH(s) + O(s)	3.7 × 10 ²⁴	59.5
CH(s) + O(s) → HCO(s) + Rh(s)	3.7 × 10 ²¹	167.5

For this simulation, a 20-node grid is initially created. The grid is refined during the simulation to provide an optimal number of nodes for the fast and accurate convergence of the solution. The simulations show that a grid with 42 nodes provided a robust solution.

The effect of the surface temperature on iso-octane conversion rate is shown in Figure 18. As indicated in the figure, the ignition point is between 700 K and 800 K.

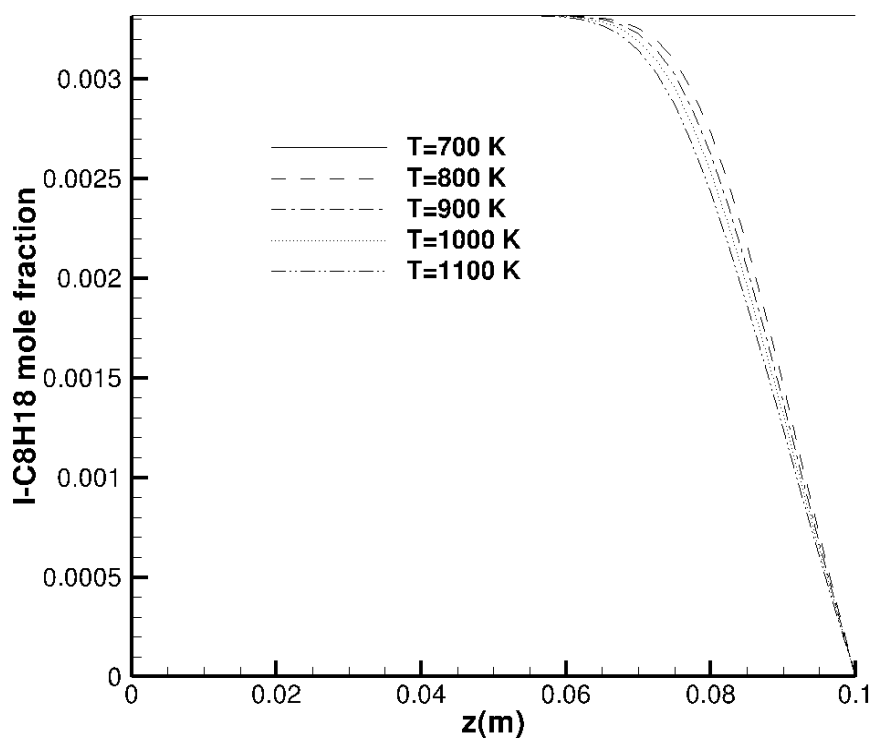


Figure 18 Effect of the surface temperature on I-C8H18 concentration

The surface temperature also affects the coverage of surface species. At low temperatures, the surface is almost completely covered by C(S). With increasing temperature, the

value of $C(S)$ is decreased and $O(S)$ and $CO(S)$ are the dominant surface species as shown in Figure 19.

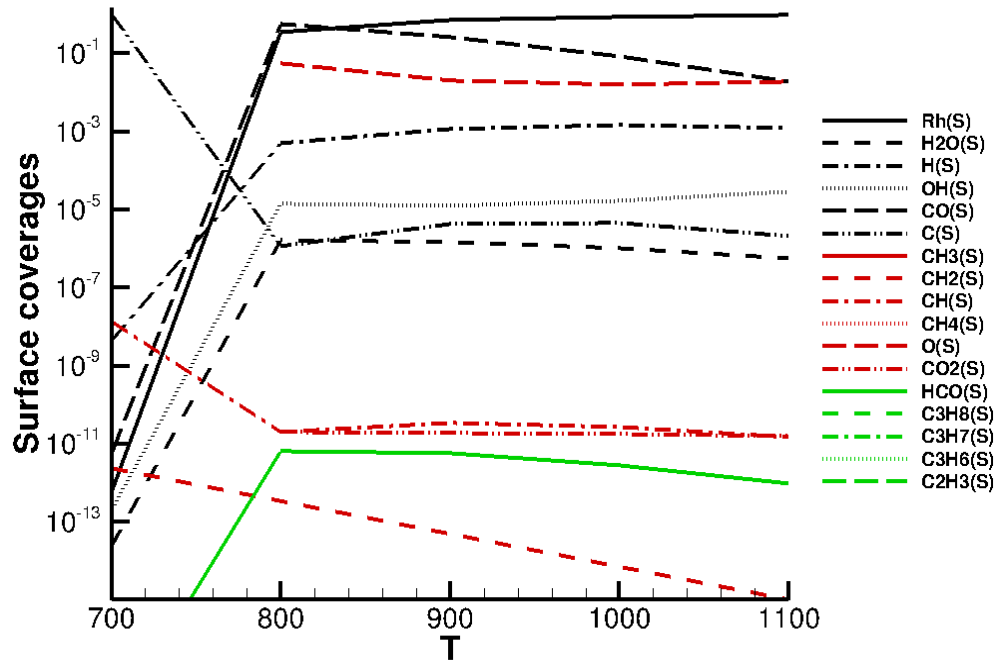


Figure 19 Surface coverages for the different surface temperature

Figure 20 shows the gas phase concentration along the injection to surface at the temperature 1100 K. The iso-octane is oxidized and combusted almost completely on the surface and products are mainly H_2O , CO and CO_2 .

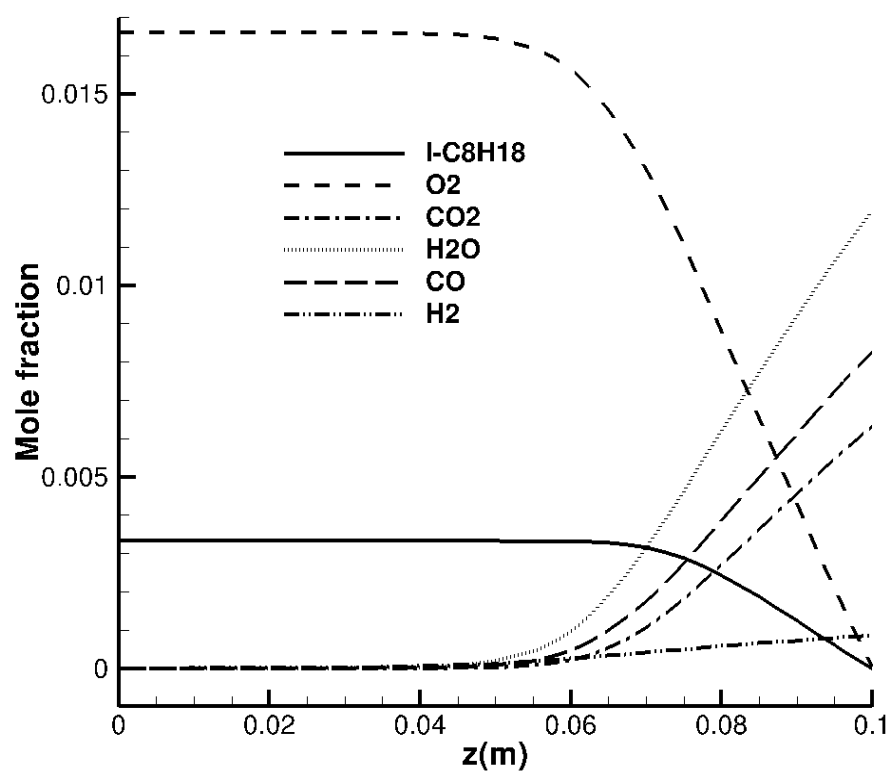


Figure 20 Gas phase species concentrations for the surface temperature 1100 K

CHAPTER 4

CATALYTIC PARTIAL OXIDATION OF METHANE

To organize and present the research in this chapter, the computational results are divided into a number of sections. For the catalytic partial oxidation of methane, these sections specifically address the parallel performance of the developed methodology, validation with experimental data, parametric study of design parameters, sensitivity analysis, and design optimization.

4.1. PARALLEL PERFORMANCE

The parallel performance of the currently developed methodology is assessed using the simulation for the catalytic partial oxidation of methane. The details concerning this simulation are presented in the following section, and are not presently required to assess algorithmic performance. The developed methodology utilizes standard Message Passing Interface (MPI) libraries, and the scalable performance is examined over an increasing range of processors. The simulations are performed on an in-house SimCenter cluster. This cluster has 325 dual-processor dual-core machines (1300 cores total), E1200 Gigabit Ethernet switches, and a cluster performance of 7.7 terraflops (TF).

Considering 10 Newton iterations, the execution times for 1, 2, 4, 8, 16, 32, 64 and 128 processors are shown in Figure 21. As illustrated in the figure, run time is decreased with increased number of processors. However, for evaluating the parallel efficiency, it more useful

to ascertain how much performance gain is achieved by parallelizing a given problem over a serial implementation. The speedup is a measure that captures the relative benefit of solving a problem in parallel. Speedup is defined as the ratio of the time taken to solve a problem on a single processor to the time required to solve the same problem on a parallel system [48]:

$$Speedup = \frac{T_{serial}}{T_{parallel}} \quad (48)$$

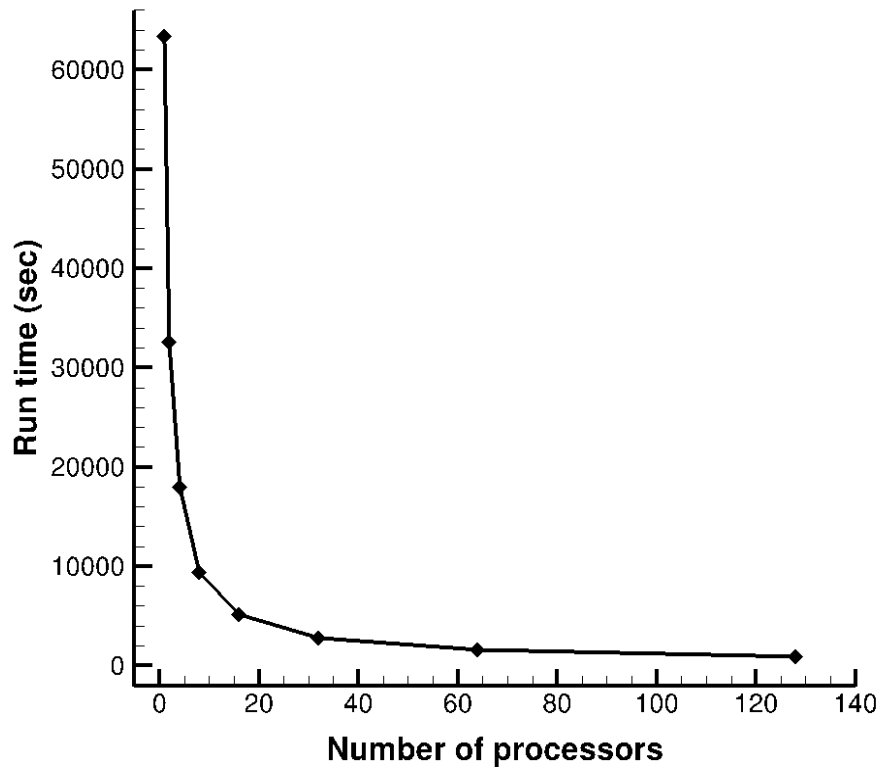


Figure 21 The total run times for the different number processors

The speedup for the current case is presented in Figure 22. As indicated, the speedup is decreasing with increasing the number of the processors. The computing speedup is close to the ideal speedup for the number of processors less than 10. Increasing number of processors for a fixed size problem, the communication overhead is increased, and which lead to decreasing

speedup. This result is typical in that for a given discretization, the amount of computational work is fixed, and as the number of processors is increased the communication costs become more significant. For larger problem sizes, the theoretical speedup is achieved for a larger number of processors.

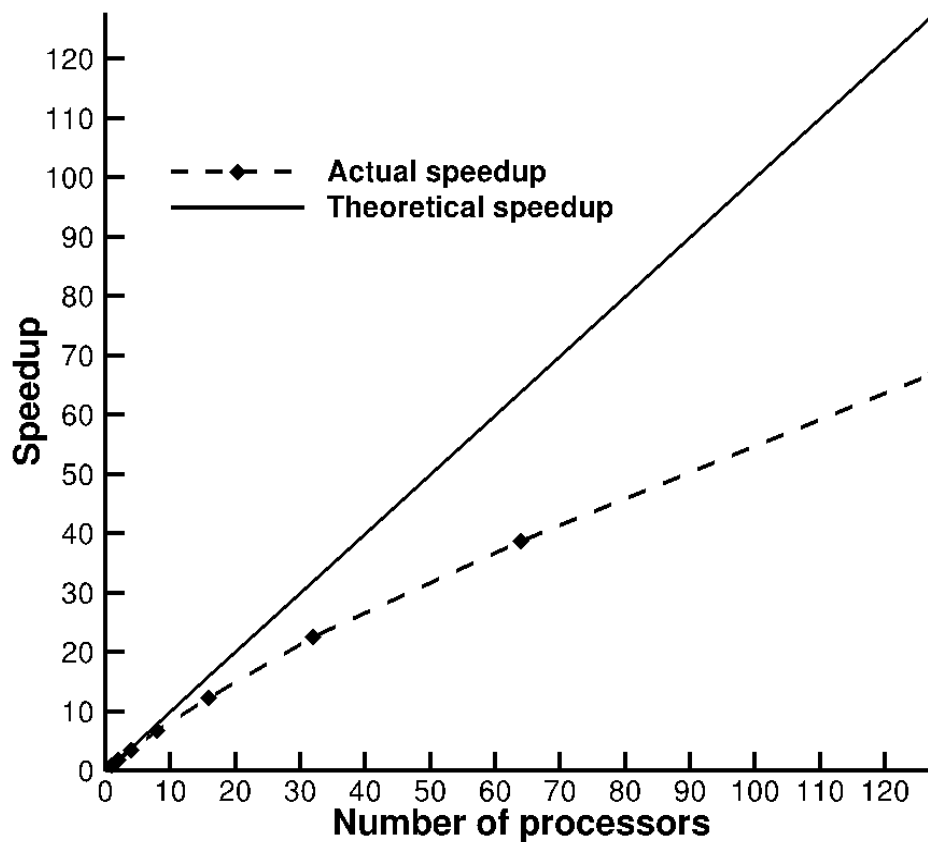


Figure 22 Parallel performance using Speedup

4.2. VALIDATION FOR THE CATALYTIC PARTIAL OXIDATION OF METHANE

In this section, the catalytic partial oxidation of methane over Rh/Al₂O₃ coated honeycombs is numerically investigated. Honeycomb-structured reactors are widely used in many engineering applications such as fuel reformers, catalytic converters, and gas turbine combustors. The experimental study conducted by Hettel *et al.* [14] is selected for validation purposes. In the experimental study the reactor is a 2 cm diameter cylinder, with 260 channels, and a channel density of 600 cpsi (channels per square inch). The initial and boundary conditions are summarized in Table 4. The simulations are performed with the detailed heterogeneous oxidation mechanism proposed by Deutschmann *et al.* [35], and include 38 heterogeneous reactions and 20 surface-adsorbed species. The site density is assumed to be 2.79×10^{-9} mol/cm², and the kinetic data of the surface-reaction mechanisms are taken from the literature. Eight gas-phase species (CH₄, CO₂, H₂O, N₂, O₂, CO, OH and H₂) are considered for the simulation, with the surface chemistry modeled using the mean-field approximation. Since it has no significant effect on the flow field for this test case and operating conditions, the homogenous combustion in the gas phase is ignored in this study [47]. The computational grid is comprised of 122,208 tetrahedral cells, and the parallel simulation performed with 64 processors. Figure 23 depicts the surface grid for one channel of the monolith. The grid is refined in the regions near the catalytic wall to accurately resolve the boundary layer. The “inflow” boundary condition is used at the channel inlet, and a fully developed boundary condition is considered for the outlet. The no-slip boundary condition with a catalytic reaction source term is applied at the channel walls. The temperature of the catalytic wall is assumed to be constant along the channel. The nonlinear system of equations obtained from the discretization is solved using Newton’s method, and the convergence history of the solution is shown in Figure 24.

Table 4 Initial conditions for catalytic partial oxidation of methane

Gas inlet velocity	0.329 m/s
Gas inlet temperature	1000 K
Wall temperature	1000 K
Gas inlet compositions (mole fraction)	$x_{\text{CH}_4} = 0.133$, $x_{\text{O}_2} = 0.067$, $x_{\text{N}_2} = 0.8$
Working pressure	1 atm
Channel width	1 mm
Channel length	10 mm



Figure 23 Grid generated for the channel of reactor

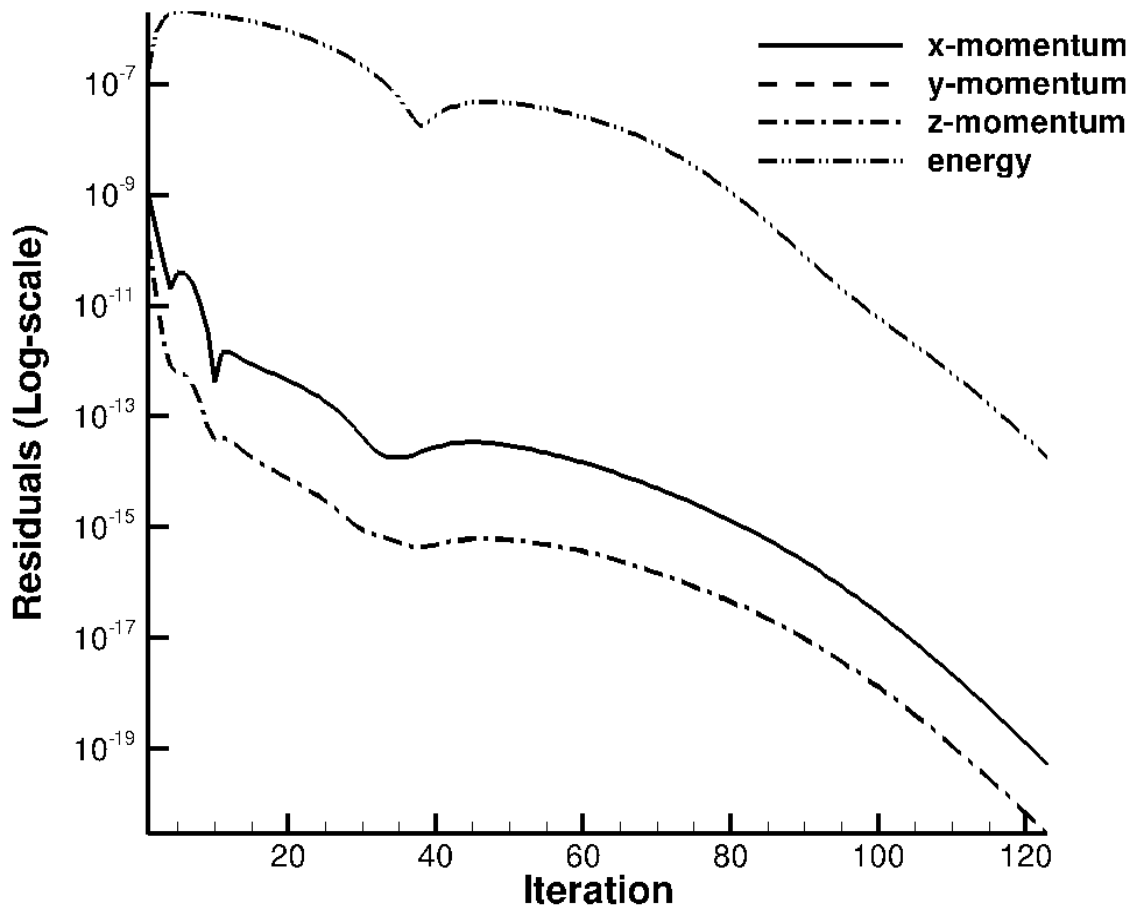


Figure 24 Convergence history of the solution

Figure 25 illustrates the comparison between the numerical results and experimental data for the species mole fractions as a function of position in the reactor. As seen, overall good agreement is observed. At the inlet of the reactor methane oxidation begins, and in the experimental test set-up the temperature is increased gradually to 1000 K in this initial section of the reactor. Therefore, due to difficulties in replicating these precise conditions, the greatest difference between the numerical and experimental data is visible in this region. Furthermore, as expected, oxygen is completely consumed in the first few millimeters of the reactor.

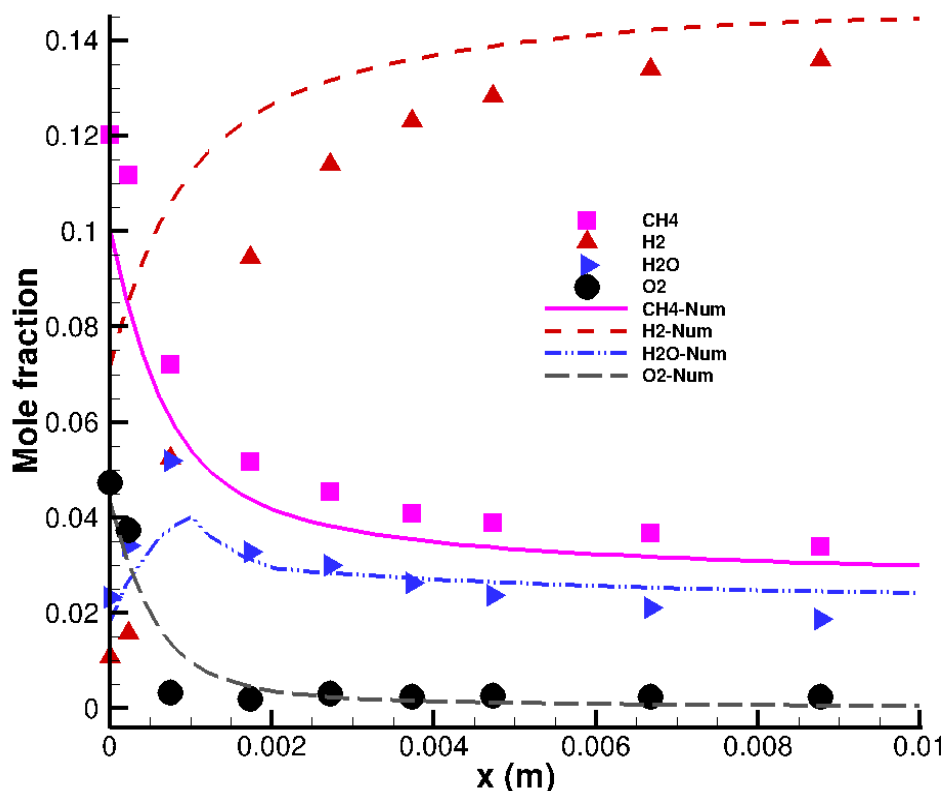


Figure 25 Comparison between the numerical results and experimental data for the partial oxidation of methane

Rhodium and platinum are considered good catalysts in terms of stability and yields. They are widely used for partial oxidation and catalytic combustion of methane in fuel reformers, catalytic burners and catalytic gas turbines. To better understand the performance of a methane reformer with these two catalysts, numerical simulations are performed. The detailed heterogeneous oxidation mechanisms developed by Deutschmann *et al.* [35] (24 heterogeneous reactions and 11 surface-adsorbed species) and Deutschmann *et al.* [41] (38 heterogeneous reactions and 20 surface-adsorbed species) are used to model surface chemistry for rhodium and platinum, respectively. The temperature of the catalyst wall is fixed to 1070 K. The inlet velocity

is considered to be 0.5 m/s. Figure 26 shows the mole fraction of species along the symmetry axis of the reformer for both catalysts. As seen, oxygen is completely consumed (conversion of 99%) in both cases. Rhodium shows better performance for partial oxidation of methane (conversion of 90%) than platinum (conversion of 77%).

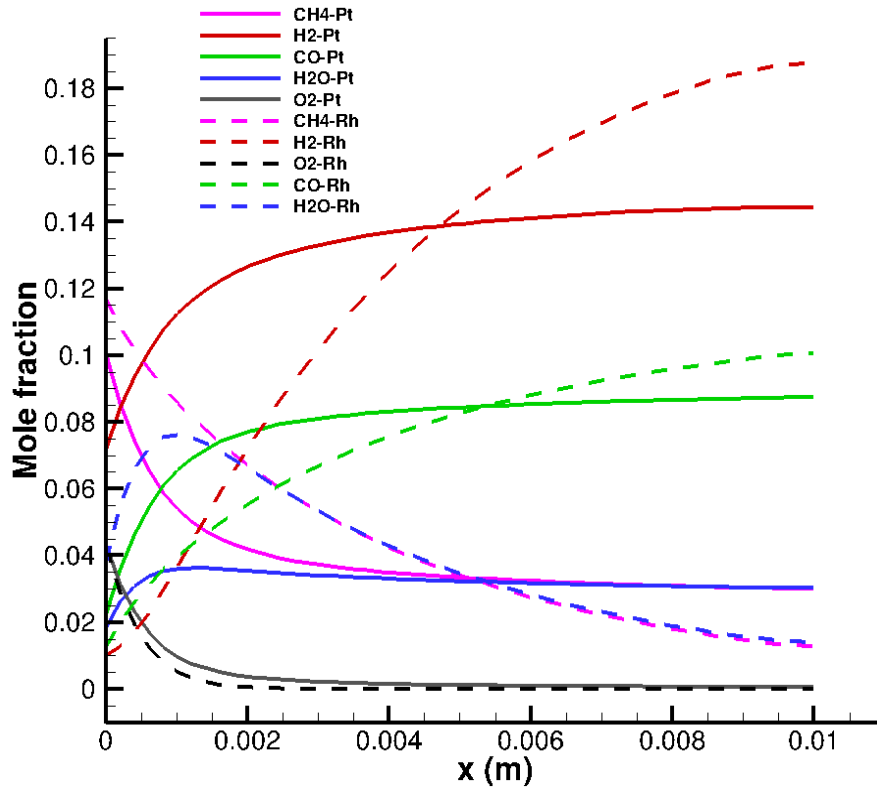


Figure 26 The mole fraction of species along symmetry axis of the reformer for both catalyst Rh and Pt

Figure 27 and Figure 28 show species mole fraction contours for reactors with platinum and rhodium, respectively. Streamwise velocity contours are also shown in Figure 27(f). The gradient of the hydrogen mole fraction is smaller across the cross section of the channel as hydrogen has a higher diffusion coefficient relative to other species considered in this simulation. The maximum velocity in the channel is close to 1 m/s.

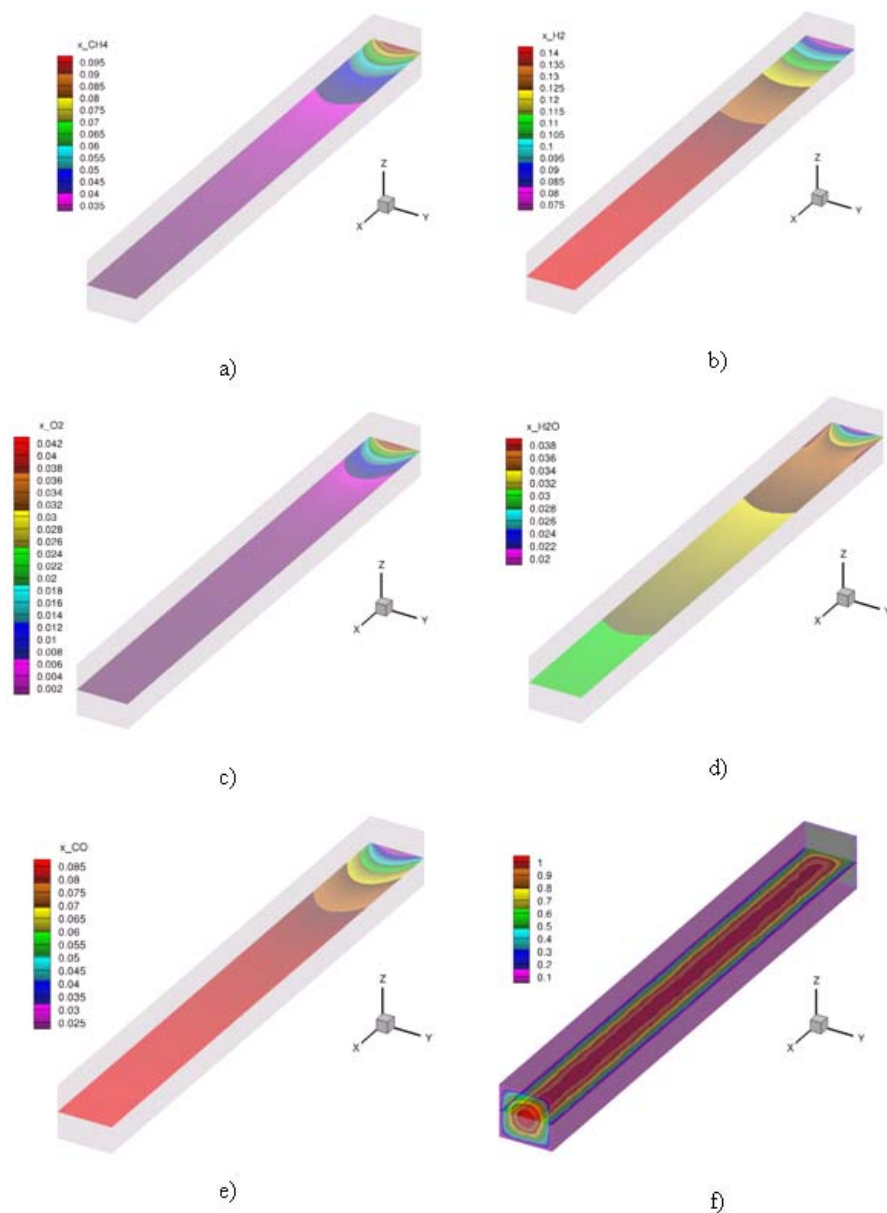


Figure 27 Contour plots for the reactor with Platinum catalyst a) CH₄ mole fraction b) H₂ mole fraction c) O₂ mole fraction d) H₂O mole fraction e) CO mole fraction f) x-velocity

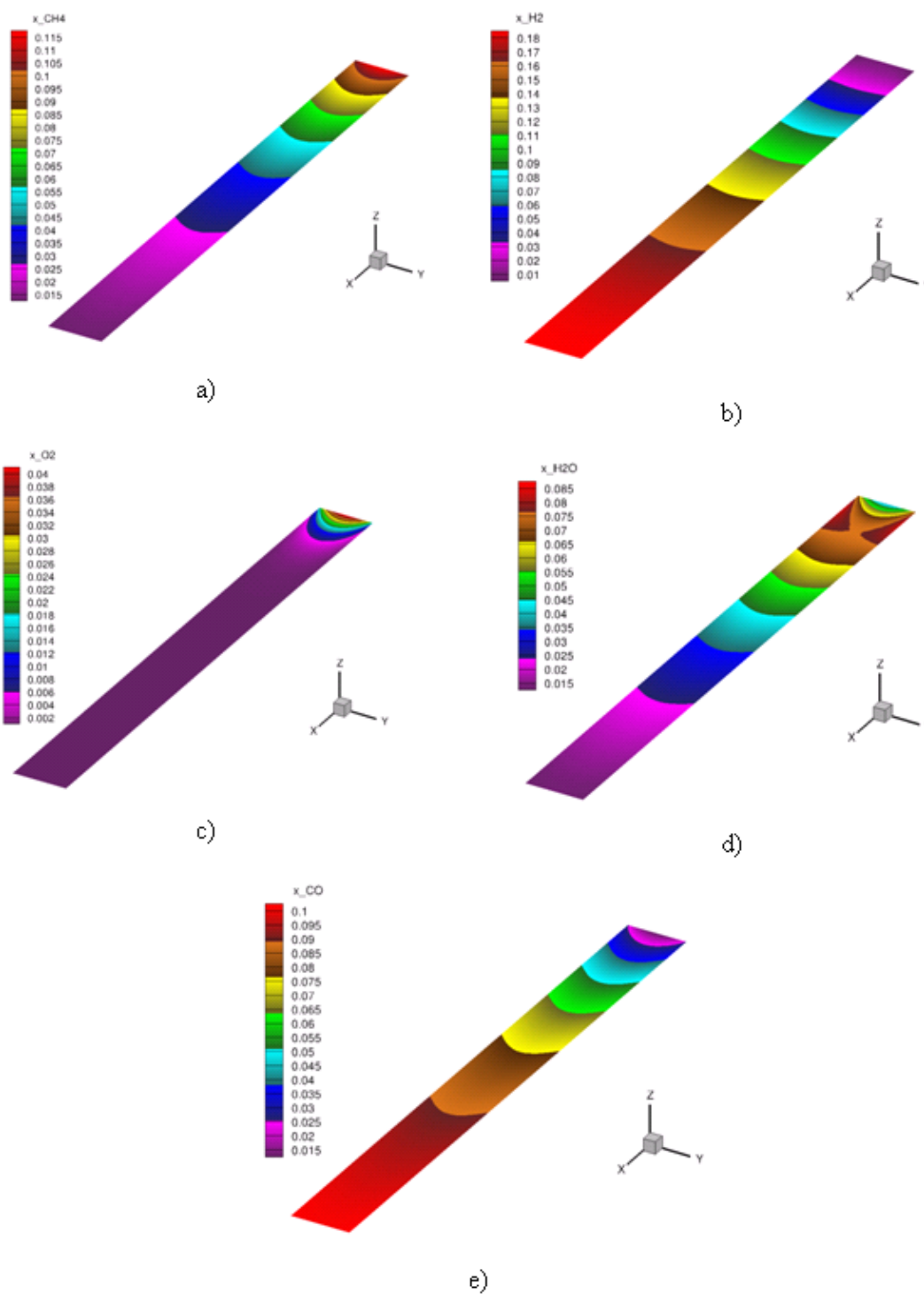


Figure 28 Contour plots for the reactor with Rhodium catalyst a) CH₄ mole fraction b) H₂ mole fraction c) O₂ mole fraction d) H₂O mole fraction e) CO mole fraction

4.3. PARAMETER STUDY

In this section, the effect of the different design parameters on the fuel reformer performance is investigated. These design parameters can be related to the shape/size of the reformer as well as the operating conditions and catalyst material. In this work the inlet methane/oxygen ratio, inlet velocity, and catalytic wall temperature are considered as variables for parametric study. Note that by using the inlet velocity as one of the parameters, the effect of different Reynolds numbers on reformer performance is also studied indirectly.

The baseline conditions for this study are shown in Table 5. Figure 29 shows the comparison of the mole fraction of species along the symmetry axis of the reformer with two different inlet velocities of 0.5 and 2 m/s. The conversion of methane is predicted to decrease with increasing inlet velocity. The rate of oxygen consumption along the reactor is also decreased and therefore the peak of H_2O concentration is shifted towards the middle of the channel for the higher inlet velocity. Mole fraction contours of the different species for the reactor with inlet velocity of 2 m/s are illustrated in Figure 30.

Table 5 Baseline conditions for catalytic combustion of methane

Gas inlet velocity	0.5 m/s
Gas inlet temperature	1070 K
Wall temperature	1070 K
Gas inlet compositions(mole fraction)	$x_{\text{CH}_4} = 0.133$, $x_{\text{O}_2} = 0.067$, $x_{\text{N}_2} = 0.8$
Working pressure	1 atm
Channel width	1 mm
Channel length	10 mm
Catalyst	Rh

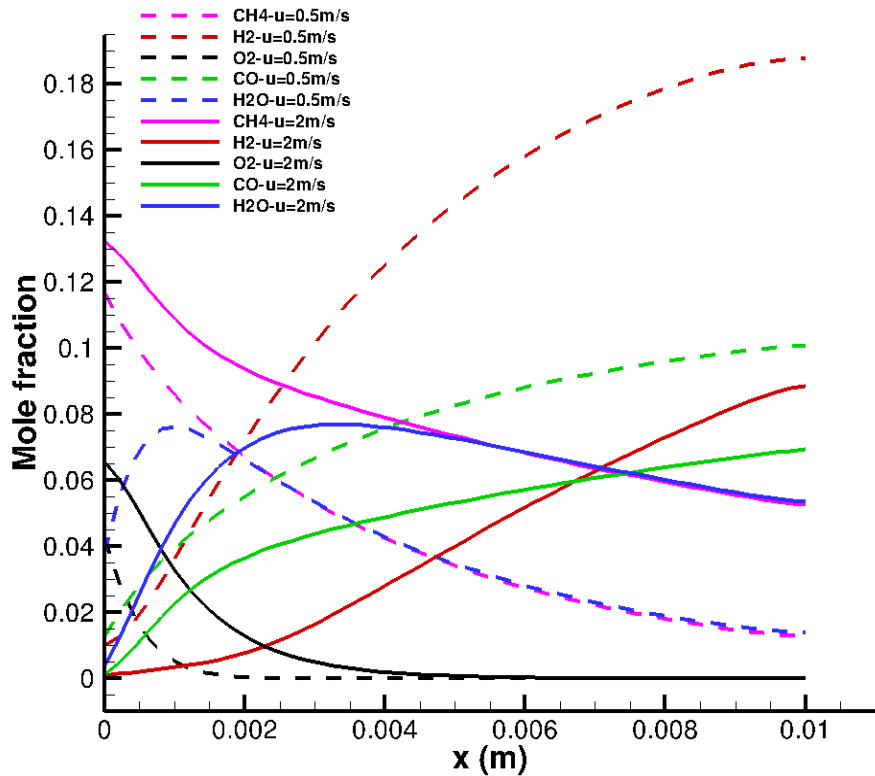
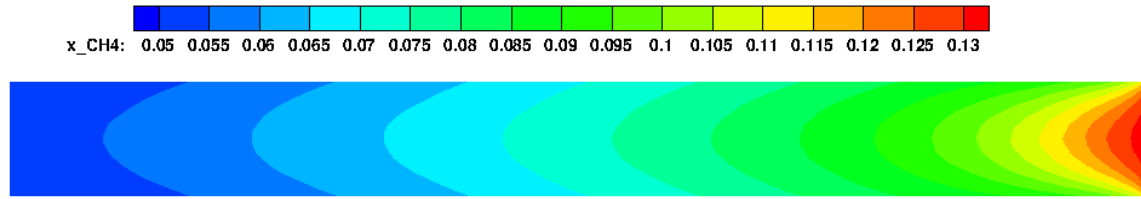
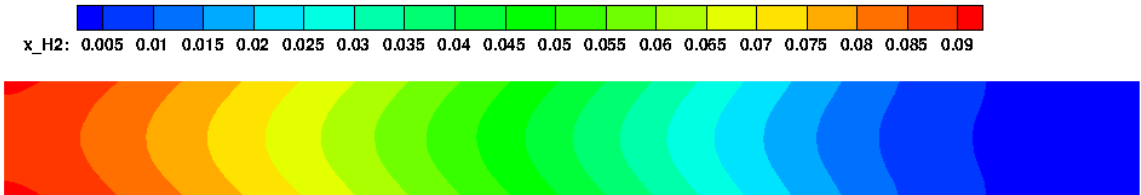


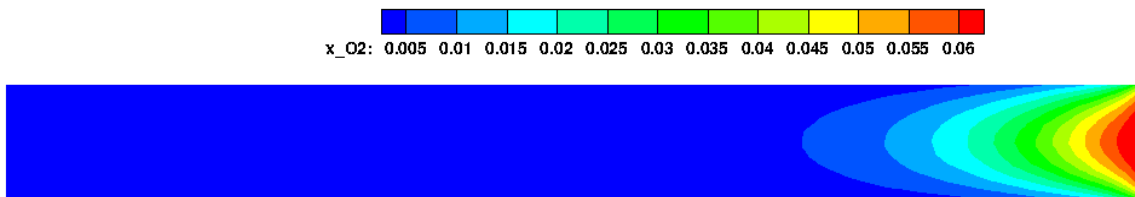
Figure 29 The comparison of the mole fraction of species along symmetry axis of the reformer with the different inlet velocities 0.5 and 2 m/s



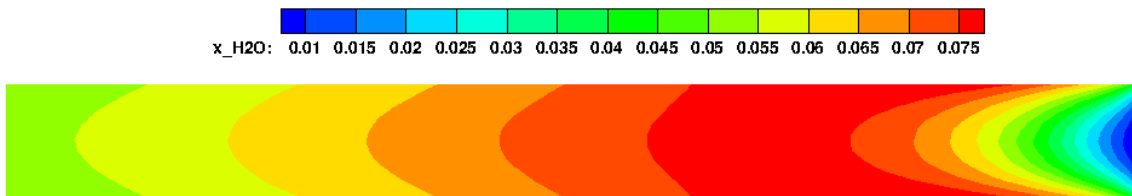
a)



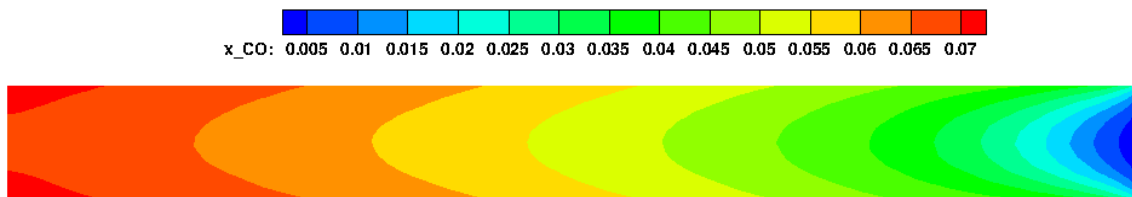
b)



c)



d)



e)

Figure 30 The mole fraction contour for the reactor with the inlet velocity 2 m/s

The influence of the catalytic wall temperature on species conversion rates is shown in Figure 31. The numerical results predict that the conversion of methane increases from 90% at 1070 K to 96% at 1170 K. Additionally, hydrogen production is increased by approximately 10% at the higher temperature.

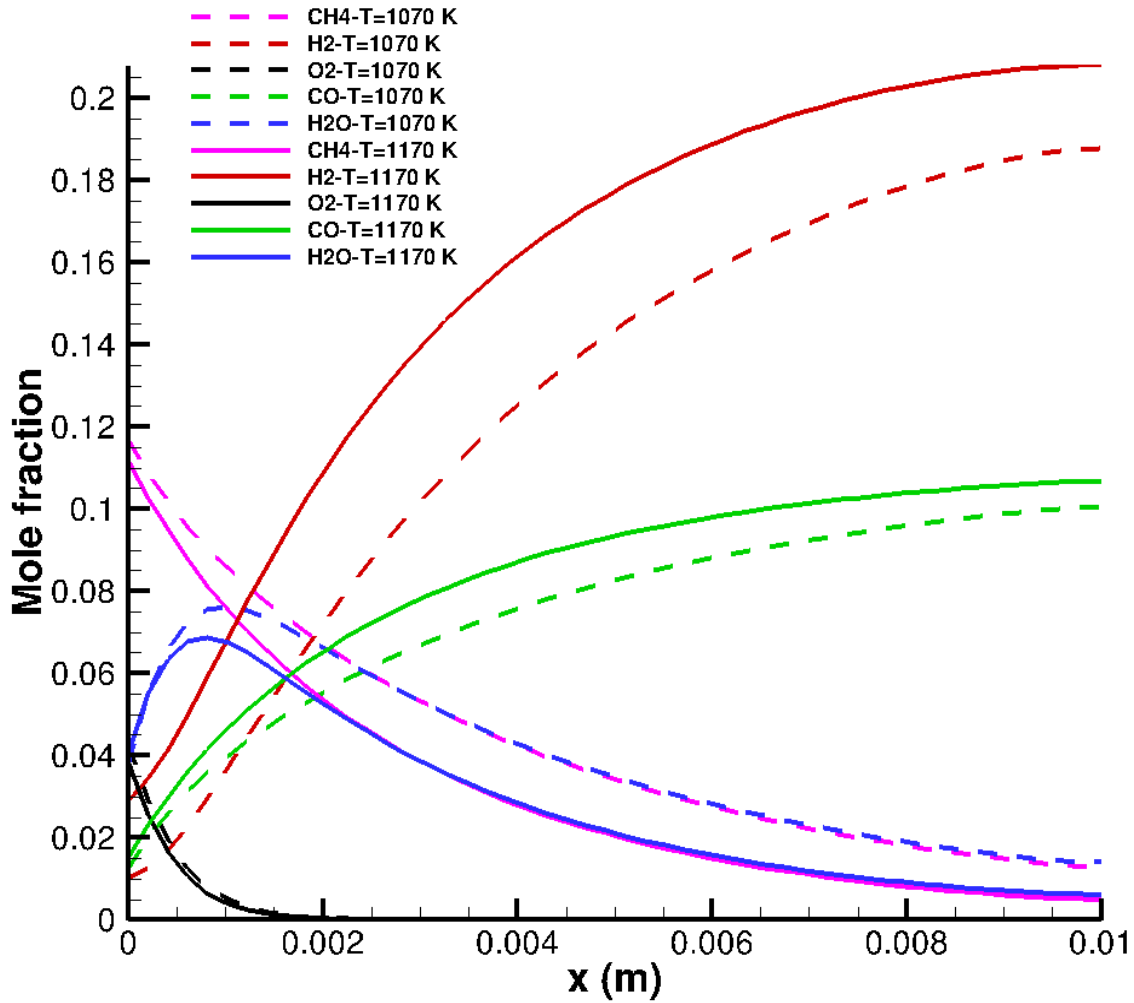


Figure 31 The comparison of the mole fraction of species along symmetry axis of the reformer for the different catalytic wall temperature

The inlet methane-oxygen ratio represents another important design parameter. To investigate the influence of this ratio, two different simulations were performed. These consisted of methane-oxygen ratios of 1 ($x_{CH_4} = 0.1$ and $x_{O_2} = 0.1$) and 1/3 ($x_{CH_4} = 0.05$ and $x_{O_2} = 0.15$). The numerical results are shown in Figure 32, which compares the aforementioned cases with a baseline methane-oxygen ratio of approximately 2 ($x_{CH_4} = 0.133$ and $x_{O_2} = 0.067$). Figure 32 demonstrates the influence of the methane-oxygen ratio on reformer performance. As seen, the size of the active methane conversion region increases with higher methane-oxygen ratios at the inlet. The hydrogen production reaches the highest level for the most-fuel-rich mixture. Hydrogen production for the mixture ratio of 1/3 is minimal and CO, CO₂ and H₂O are the main products, as can be seen from the mole fraction contours illustrated in Figure 33.

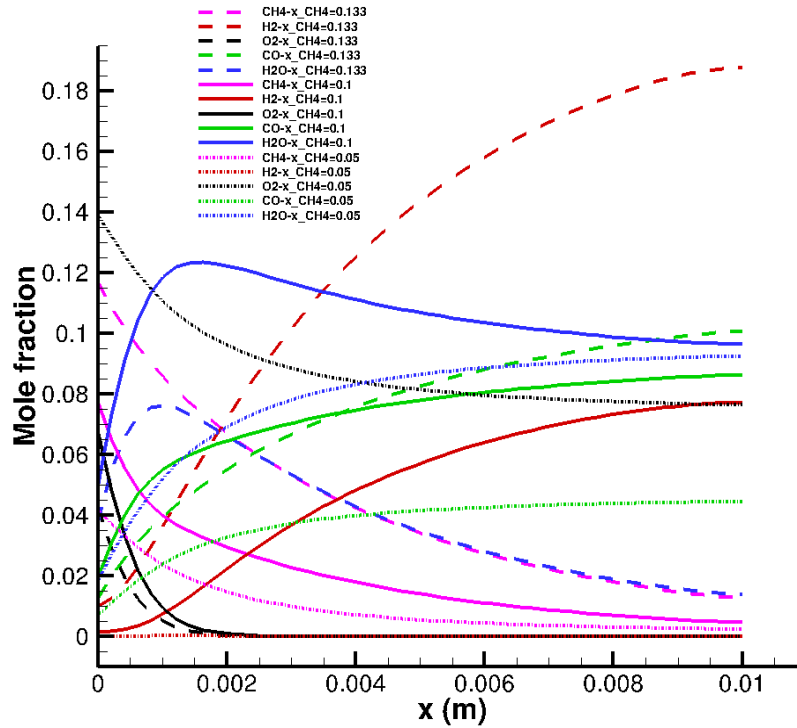
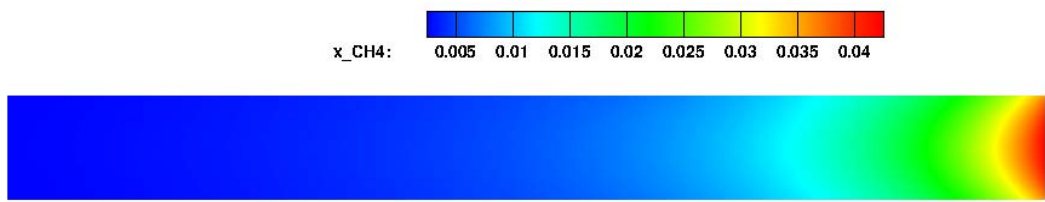
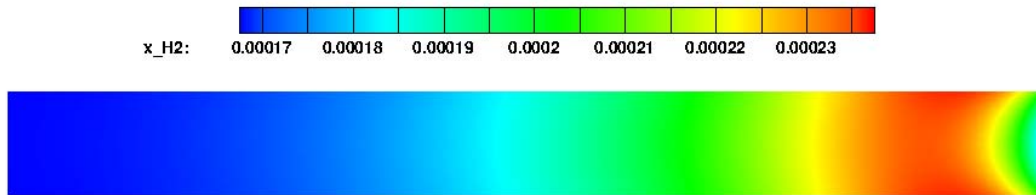


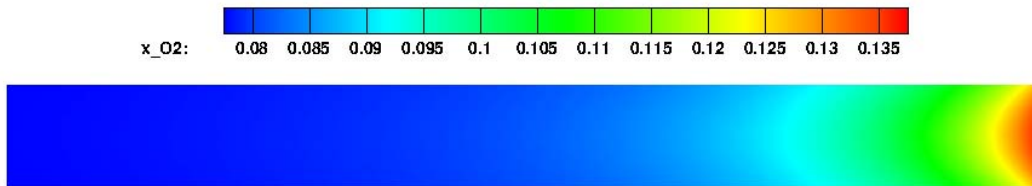
Figure 32 The influence of the variation of methane/oxygen ratio on the reformer performance



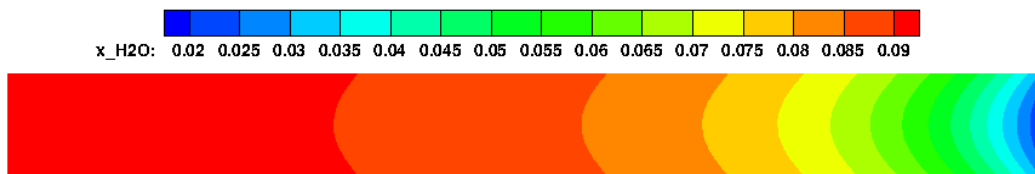
a)



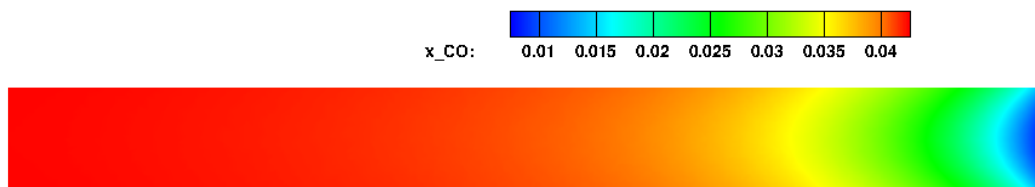
b)



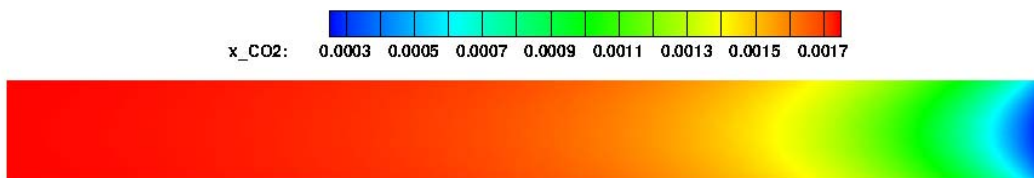
c)



d)



e)



f)

Figure 33 The mole fraction contour for the reformer with the methane/oxygen ratio 1/3

Catalyst loading is an important factor in the design and optimization of catalytic reactors. The heterogeneous flux with catalyst loading effects has been previously given in equation (24). For considering the effect of catalyst loading, two parameters $F_{\text{cat/geo}}$ (ratio of catalytic surface area to geometric surface area) and η (effectiveness factor) are considered. As shown in Figure 34, the methane conversion increases for high catalyst loading. The methane conversion increases from 57% at $F_{\text{cat/geo}}\eta = 0.5$ to 98% at $F_{\text{cat/geo}}\eta = 2$, and the hydrogen production at $F_{\text{cat/geo}}\eta = 2$ increases about 7% relative to the baseline case. Additionally, oxygen is almost completely consumed by surface reactions in the first millimeter of the reactor length for all three cases. For $F_{\text{cat/geo}}\eta = 0.5$ the contours of the concentrations of species along the length of the reactor are shown in Figure 35 to illustrate the variations within the channel.

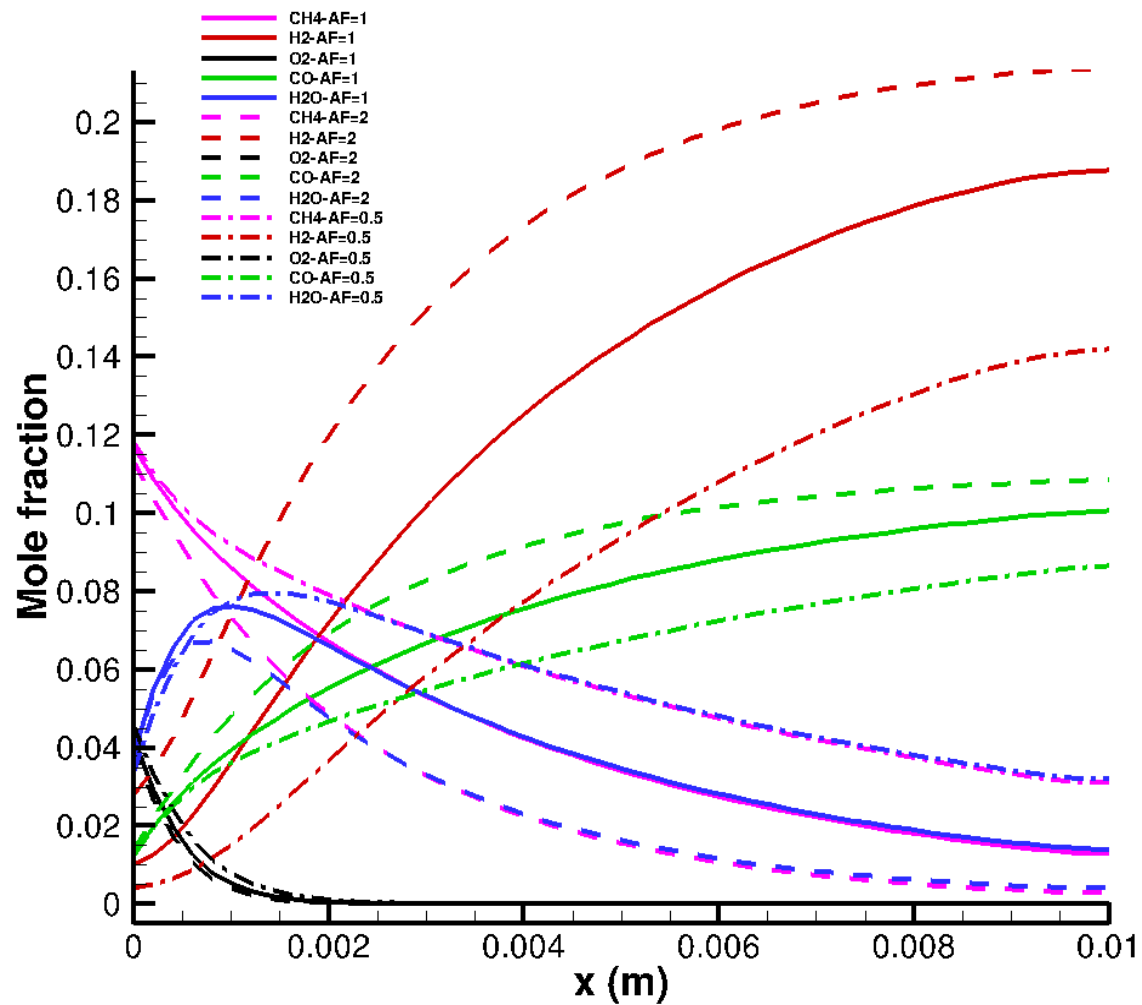


Figure 34 The influence of the variation of the catalyst loading on the reformer performance

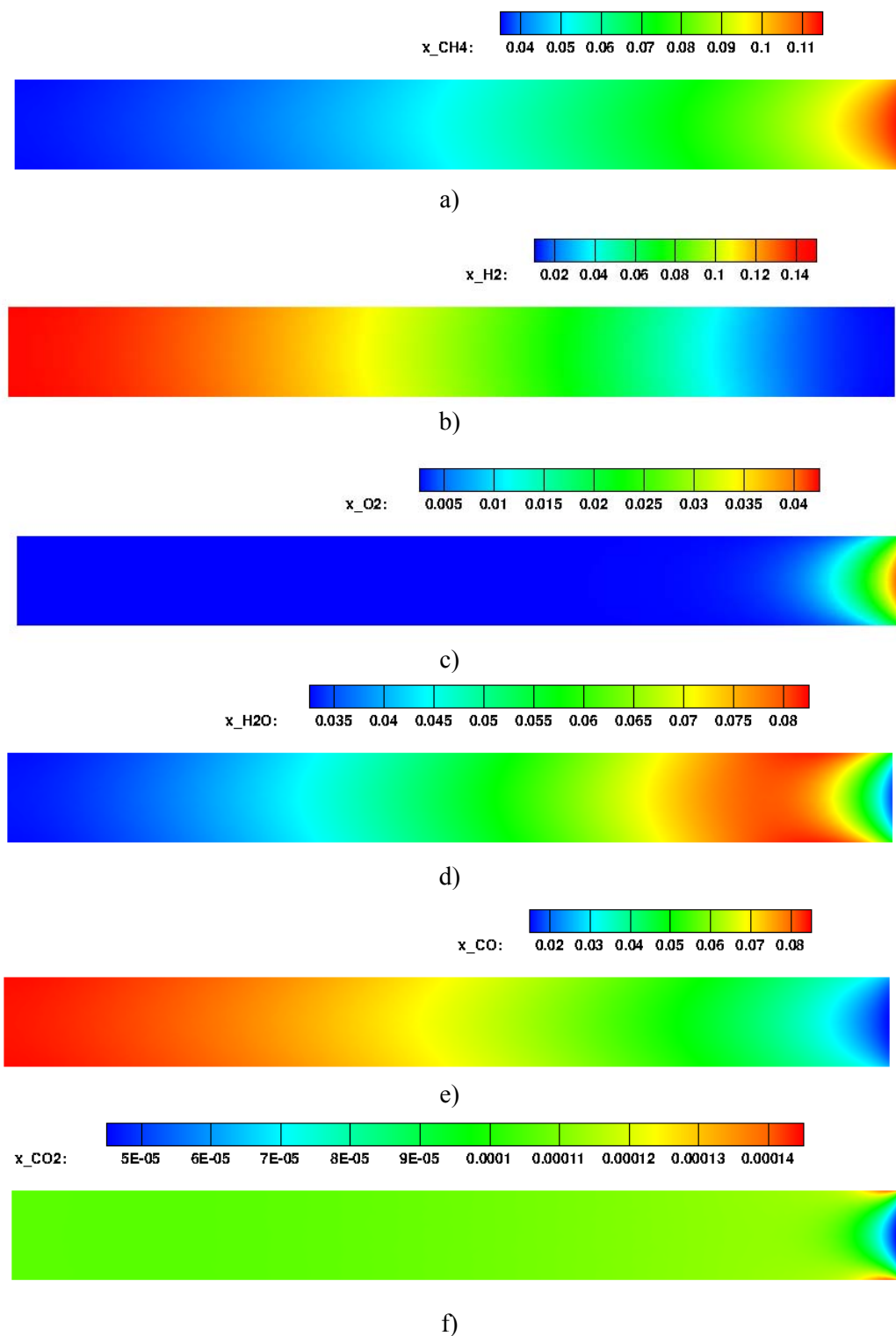


Figure 35 The mole fraction contour for the reformer with $F_{cat/geo}\eta = 0.5$

4.4. SENSITIVITY ANALYSIS

For the parametric studies, the dependencies of the reformer performance on design variables were obtained by comparing baseline solutions to those with variations. An alternative approach to assessing these effects is through the use of sensitivity analysis. In this method, the sensitivities are obtained by computing gradients or derivatives of the solution with respect to the set of design variables. These sensitivity analysis methods, having widely varying implementation costs, provide a precise sensitivity measure at roughly the same cost as a function evaluation [26]. As previously discussed, there are several methods for computing sensitivity derivatives.

The typical use of sensitivity analysis is for computational design whereby the cost function is to be either minimized or maximized. To improve the cost function, gradient-based optimization algorithms require information on how the cost function changes with respect to the design variables; that is, $dl/d\beta$. Furthermore, sensitivity derivatives may be used to identify the variables that have the most significant impact on design performance. Design variables of the inlet velocity, methane density, oxygen density, catalytic wall temperature, and catalytic area ratio are considered for sensitivity analysis in this study. The mean value of H_2 concentration at the outlet boundary is considered as the cost function. For verification purposes, sensitivity derivatives obtained using the adjoint and direct differentiation approaches are compared with those computed using a central finite-difference method. For the central finite-difference method, a perturbation value of 1×10^{-5} is used for the simulation. The baseline conditions for this study have been previously given in Table 5. Sensitivity derivative results are presented in Table 6. As illustrated in Table 6, the sensitivity derivatives obtained by the direct differentiation and adjoint methods show good agreement, and match up to nine digits. Additionally, it may be observed

that methane concentration, followed by oxygen concentration, plays the most significant roles in the mean value of H_2 concentration. Differences are observed in comparisons with the central finite-difference method. These discrepancies may be attributable to the highly nonlinear response of the cost function to the design variables and due to subtractive cancellation errors in the finite-difference method. To ascertain a better understanding on the sources of errors, a more detailed step-size study for the finite-difference method is warranted.

Table 6 The sensitivity derivatives for the different design variables

DV	finite difference	direct differentiation	adjoint
Inlet velocity	-0.00571674320	-0.00580817201	-0.00584081720
Inlet methane concentration	0.10364058231	0.10718769820	0.10718769812
Inlet oxygen concentration	-0.080342139543	-0.079660588349	-0.079660588319
Catalytic wall temperature	0.00116746547	0.00105843297	0.00105843127
Catalytic area ratio	0.00104274151	0.00113610487	0.00113610454

4.5. OPTIMIZATION

In gradient-based optimization algorithms, sensitivity derivatives are utilized in determining a search direction that will maximize or minimize the cost function. One potential drawback to these methods is the added complexity and computational costs associated with evaluating these gradients. However, sensitivity analysis requires solutions to linearized systems of equations, whereas finite-difference methods necessitate the solution to nonlinear systems for each design variable perturbation. Furthermore, as noted previously, the discrete adjoint method

eliminates the dependence of the sensitivity of the cost function with respect to the state-vector and, therefore, represents an efficient means to evaluate sensitivity derivatives for large number of design parameters. Since the number of design variables is small in this case, there is no significant advantage of using the adjoint method relative to the direct differentiation. Thus, the direct differentiation method is utilized.

Optimization is the minimization or maximization of a function subjected to constraints on its variables. The optimization problem can be defined as

$$\begin{aligned} & \min I(\boldsymbol{\beta})_{\boldsymbol{\beta} \in \mathbb{R}^n} \\ & \text{Subject to:} \quad \begin{aligned} & g_i(\boldsymbol{\beta}) \leq 0 \quad i \in J \\ & \boldsymbol{\beta}^L \leq \boldsymbol{\beta} \leq \boldsymbol{\beta}^U \end{aligned} \end{aligned} \tag{49}$$

where $I(\boldsymbol{\beta})$ is the objective or cost function, $g_i(\boldsymbol{\beta})$ is the vector of inequality constraints, and $\boldsymbol{\beta}^L$ and $\boldsymbol{\beta}^U$ the lower and upper side-constraints on the design variable, respectively. Numerous algorithms have been developed for solving this standard optimization problem and, moreover, are available in software packages.

In the current research, the DAKOTA toolkit is used. DAKOTA (Design Analysis Kit for Optimization and Terascale Applications) was developed at Sandia National Laboratories [38]. DAKOTA's optimization capabilities include a wide variety of gradient-based and nongradient-based optimization methods. It includes many external optimization libraries such as the OPT++ library [49], CONMIN and DOT libraries [50], and an interface to link with third-party routines that provide the function evaluations and sensitivity information.

An interface is created to link the flow solver to DAKOTA. Figure 36 shows the workflow involving the flow solver and DAKOTA. The output file from DAKOTA containing

new values for the solver is “params.in”. This file is created by DAKOTA during each design cycle.

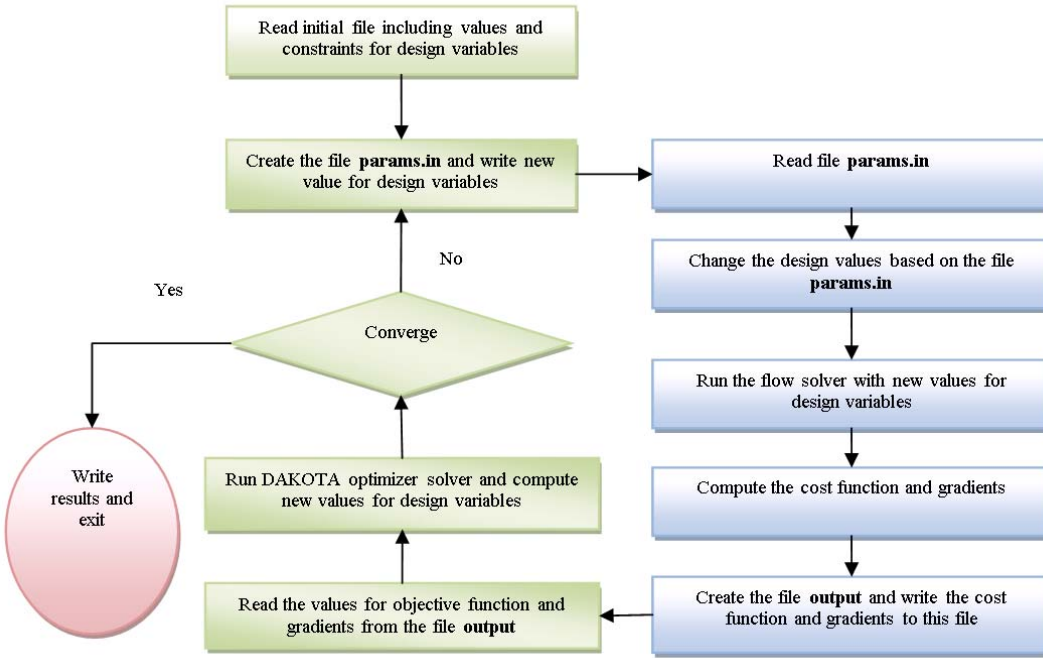


Figure 36 The data interchange and interface between the flow solver and DAKOTA

Initially, to demonstrate the numerical optimization procedure, three design parameters including inlet velocity, inlet methane concentration, and catalytic wall temperature are studied. For this optimization, the mean value of CH₄ concentration at the outlet boundary is considered as the cost function, and the initial conditions on the design parameters of inlet velocity, inlet methane concentration, and catalytic wall temperature are 0.7 m/s, 0.05, and 1000 K, respectively. The initial concentration for oxygen and nitrogen are 0.15 and 0.8, respectively. All other conditions are the same as found in Table 5. Note that since the values of the design

variables have different orders of magnitude, scaled values are used within the optimization for methane concentration and catalytic wall temperature. Additionally, side-constraints are imposed on these design variables and are listed in Table 7.

Table 7 Initial values and constrained bounds for the design variables

	inlet velocity	methane concentration at inlet	catalytic wall temperature
Lower bound	0.3	0.3	0.8
Upper bound	1.5	1.3	1.2
Initial values	0.7	0.5	1.0

The optimization is performed using two gradient-based algorithms: the Fletcher-Reeves conjugate gradient (frcg) method (from DAKOTA's CONMIN library) and a quasi-Newton method (from DAKOTA's OPT++ library). Both methods achieve the same local optimal point of 0.3 m/s, 0.0825, and 1200 K for inlet velocity, methane concentration, and catalytic wall temperature, respectively. Note that in this case, the lower side-constraint for inlet velocity and the upper side-constraint for catalytic wall temperature are active. For this particular optimization, as seen in Table 8, the quasi-Newton algorithm requires significantly more gradient calculations and design cycles as compared to the Fletcher-Reeves conjugate gradient method. Figure 37 shows a comparison of methane concentration along the centerline of the reactor using baseline and optimized conditions.

Table 8 the number of solver and gradients calls for the optimization algorithms

Method	function evaluation	gradient calculations
Fletcher-Reeves conjugate gradient method	17	7
quasi-Newton algorithm	17	15

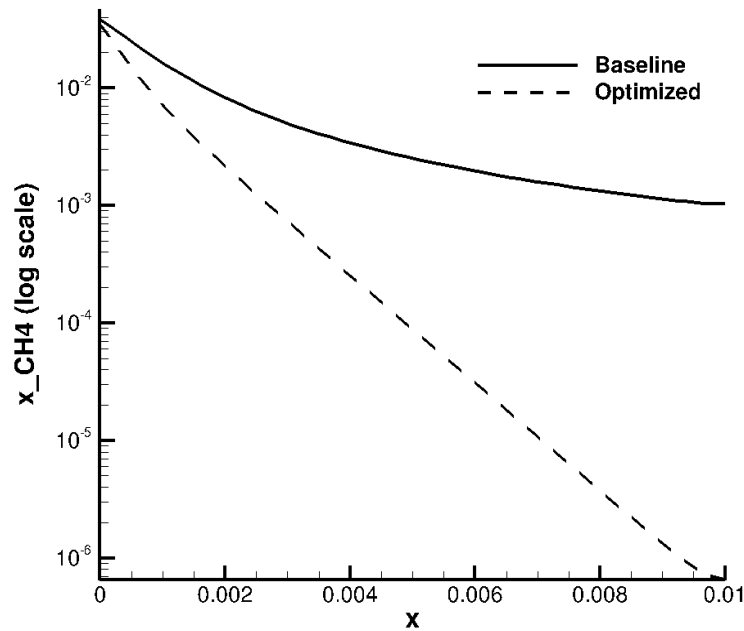


Figure 37 The comparison between the optimized conditions for methane concentration along the reactor

While the previous case optimized the methane conversion, the main goal of reformer design is to maximize the hydrogen production. In some cases, although methane is almost completely consumed for the given conditions, the main products of the chemistry are species other than hydrogen. For this reason, a cost function representing the hydrogen concentration at the outlet boundary may be defined as

$$Cost\ function = \frac{1 - \iint_{Outlet\ BC} \rho_{H_2} dA}{0.09} \quad (50)$$

Based on the previous optimization results using high-fidelity analysis, the Fletcher-Reeves conjugate gradient method is selected for this case. Again, the design variables of inlet velocity, wall temperature and inlet methane concentration are used, and the initial conditions on these design parameters are 0.7 m/s, 0.082, and 1000 K, respectively. The initial concentration for oxygen and nitrogen are 0.118 and 0.8, respectively. For this optimization, 20 objective function evaluations and 5 gradient calculations were required to obtain the local minimum point of 0.545 m/s, 0.13, and 1200 K. A comparison of hydrogen concentration along the centerline of the reactor using baseline and optimized conditions is shown in Figure 38.

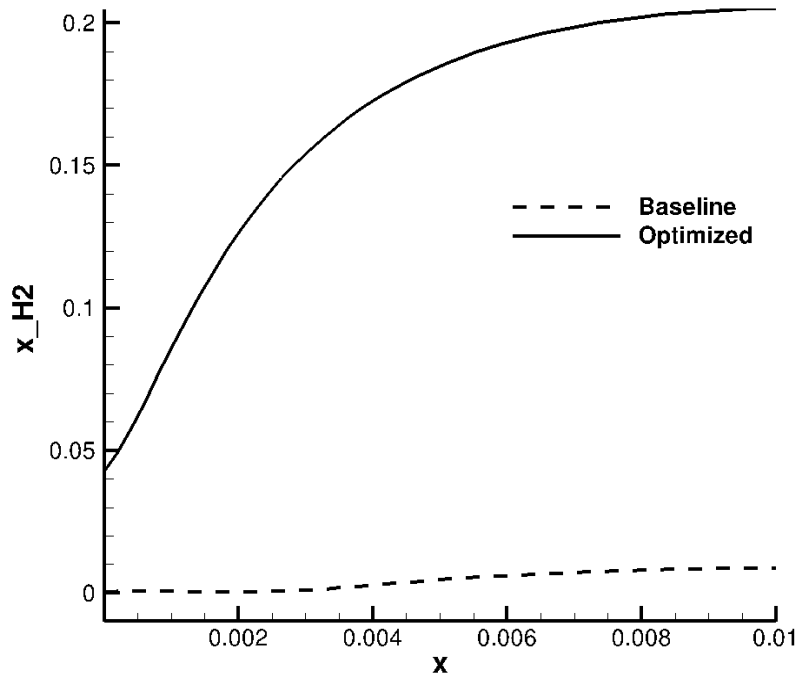


Figure 38 The comparison between the base condition and the optimized condition for hydrogen concentration along the centerline of the reactor

CHAPTER 5

NUMERICAL SIMULATION A HONEYCOMB-STRUCTURED CATALYTIC REFORMING REACTOR

The chemical and thermal phenomena within the full reactor are computationally investigated in this section. Two monolithic reactors were simulated.

The first test case is a cylindrical monolith with diameter 1.84 cm and length 10 cm as shown in Figure 39. The channels have a square cross-section of dimension 1.6 mm * 1.6 mm [6]. Since the geometry is symmetric, only a quarter of the reactor is simulated. A grid with 1,261,820 prism cells is generated by Pointwise [51] as indicated in Figure 40. Figure 41 shows the boundary conditions used to model this problem. The reactor performance is investigated with two different inflow conditions. Table 9 shows input mole fractions for two test conditions. The simulations are performed on the in-house SimCenter cluster.

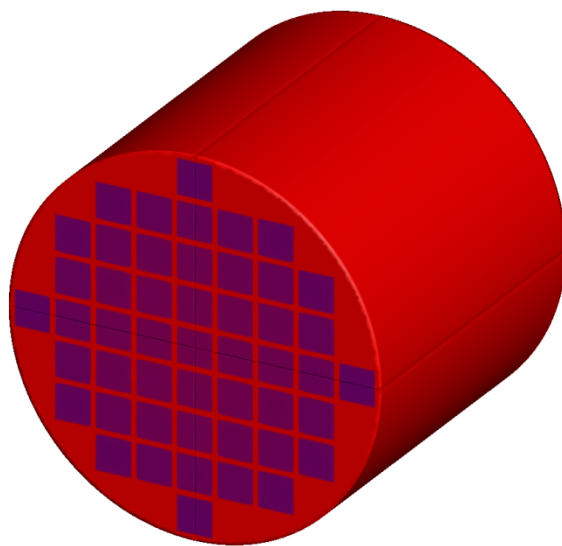


Figure 39 The cylindrical monolithic reactor with square cross-section channels

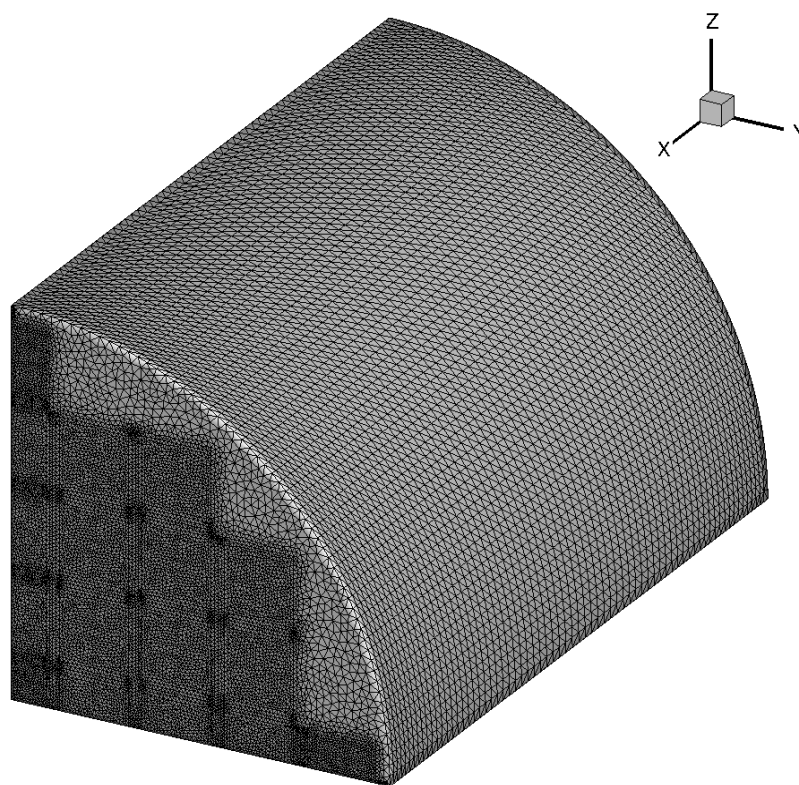


Figure 40 The generated grid for the monolithic reactor

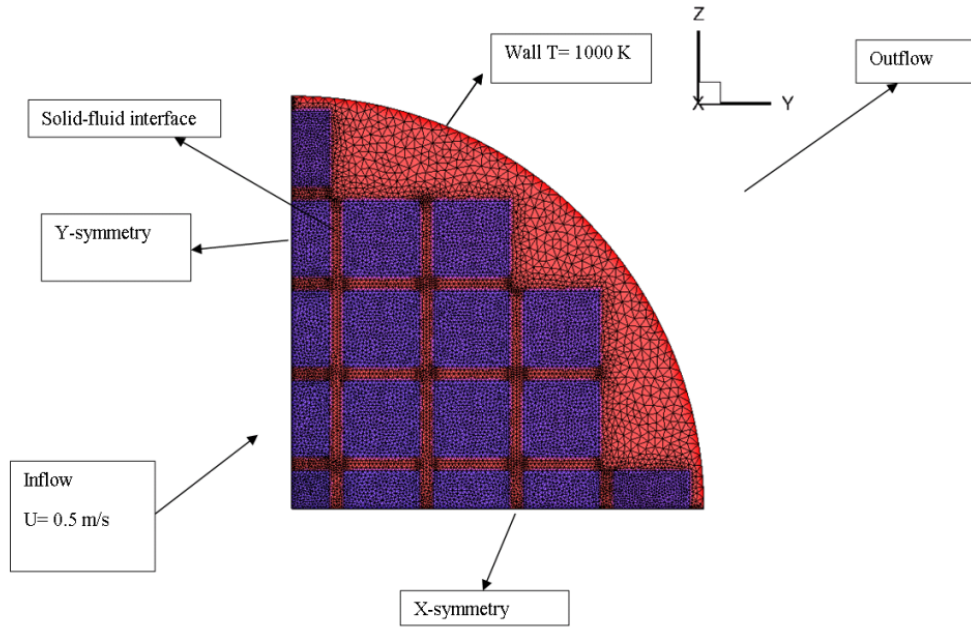


Figure 41 The boundary conditions for the monolithic reactor and mesh cross-section

Table 9 Initial conditions for fuel reforming reactor

		Test conditions 1	Test conditions 2
Gas inlet compositions(mole fraction)	x_{CH_4}	0.0449	0.133
	x_{O_2}	0.1934	0.067
	x_{N_2}	0.7545	0.8
	x_{H_2}	0.0072	0.0
Gas inlet velocity		0.329 m/s	0.329 m/s
Gas inlet temperature		975 K	975 K
Reactor temperature		1000 K	1100 K
Working pressure		1 atm	1 atm

The governing equations are similar to what were described in Chapter 2, but one additional equation for the solid phase is added. Therefore, the system of equations is:

$$\frac{\partial \vec{Q}}{\partial t} + \nabla \cdot (\vec{F}_e(\vec{Q}) - \vec{F}_v(\vec{Q})) = \vec{S}(\vec{Q}) \quad (51)$$

where

$$\vec{Q} = \begin{bmatrix} \rho_1 \\ \rho_2 \\ \vdots \\ \rho_{ns} \\ \rho u \\ \rho v \\ \rho w \\ \rho e_t \\ \sum_{i=1}^{ns} (\rho_i e_i) \end{bmatrix} \quad (52)$$

$$\vec{F}_e = \begin{bmatrix} \rho_1 u \\ \rho_2 u \\ \vdots \\ \rho_{ns} u \\ \rho u^2 + p \\ \rho uv \\ \rho uw \\ (\rho e_t + p)u \\ 0 \end{bmatrix} \hat{i} + \begin{bmatrix} \rho_1 v \\ \rho_2 v \\ \vdots \\ \rho_{ns} v \\ \rho uv \\ \rho v^2 + p \\ \rho vw \\ (\rho e_t + p)v \\ 0 \end{bmatrix} \hat{j} + \begin{bmatrix} \rho_1 w \\ \rho_2 w \\ \vdots \\ \rho_{ns} w \\ \rho uw \\ \rho wv \\ \rho w^2 + p \\ (\rho e_t + p)w \\ 0 \end{bmatrix} \hat{k} \quad (53)$$

$$\vec{F}_v = \begin{bmatrix} J_{1x} \\ J_{2x} \\ \vdots \\ J_{nsx} \\ \tau_{xx} \\ \tau_{xy} \\ \tau_{xz} \\ u\tau_{xx} + v\tau_{xy} + w\tau_{xz} - \hat{q}_x \\ 0 \end{bmatrix} \hat{i} + \begin{bmatrix} J_{1y} \\ J_{2y} \\ \vdots \\ J_{nsy} \\ \tau_{xy} \\ \tau_{yy} \\ \tau_{yz} \\ u\tau_{xy} + v\tau_{yy} + w\tau_{yz} - \hat{q}_y \\ 0 \end{bmatrix} \hat{j} + \begin{bmatrix} J_{1z} \\ J_{2z} \\ \vdots \\ J_{nzs} \\ \tau_{zx} \\ \tau_{zy} \\ \tau_{zz} \\ u\tau_{zx} + v\tau_{zy} + w\tau_{zz} - \hat{q}_z \\ -\hat{q}_{zs} \end{bmatrix} \hat{k} \quad (54)$$

$$\vec{S} = \begin{bmatrix} \dot{\omega}_1 \\ \dot{\omega}_2 \\ \vdots \\ \dot{\omega}_{ns} \\ 0 \\ 0 \\ 0 \\ 0 \\ 0 \\ 0 \end{bmatrix} \quad (55)$$

Since eight gas-phase species (CH_4 , CO_2 , H_2O , N_2 , O_2 , CO , OH and H_2) are considered in the simulation, the number of equations is 13 (8 mass conservations, 3 momentum conservations, 1 energy conservation for fluid phase and 1 energy conservation for the solid phase).

The contours of the velocity and temperature for test condition 1 are shown in Figure 42. Since the reactor wall is isothermal, the temperature within the reactor in steady state condition is reaches 1000 K. In the reactor channels, fully developed temperature profiles are recognized. The maximum velocity within the reactor channels is 1.1 m/s.

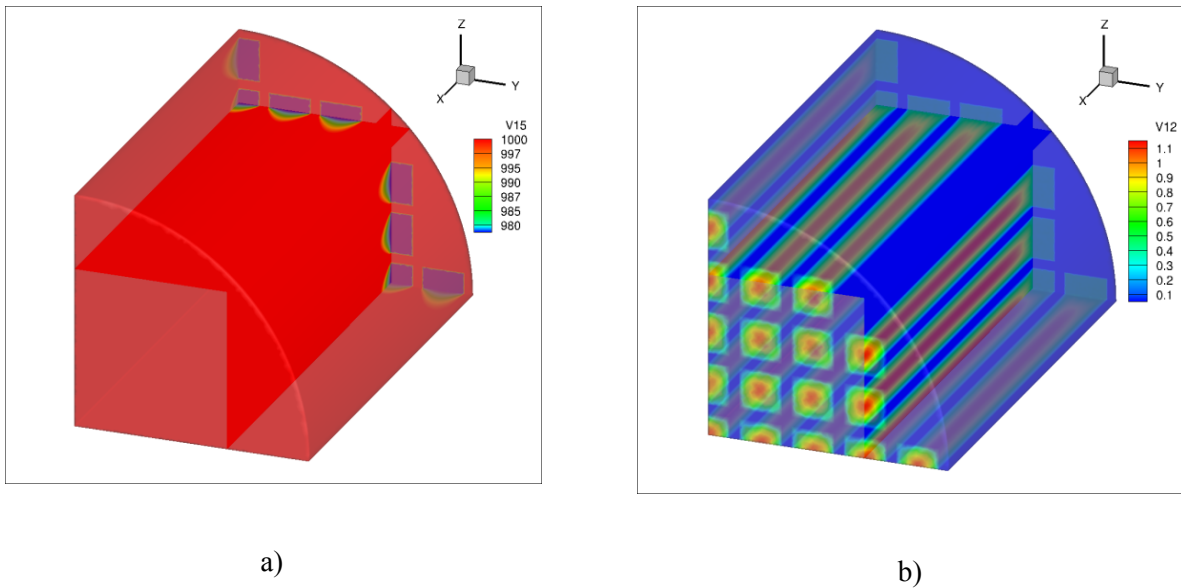
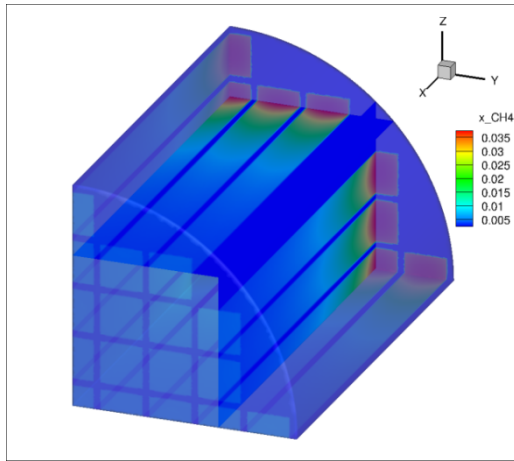
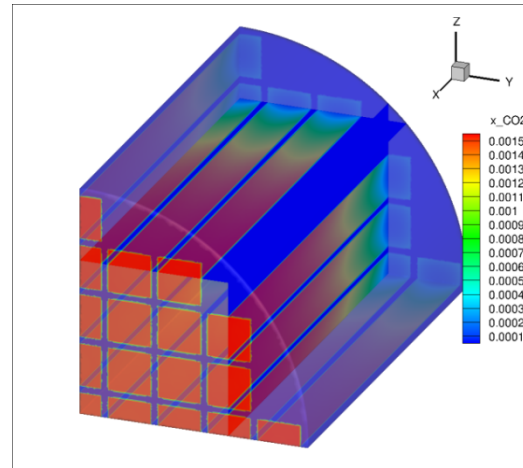


Figure 42 Contours of a) Temperature b) Velocity for the reactor at test conditions 1

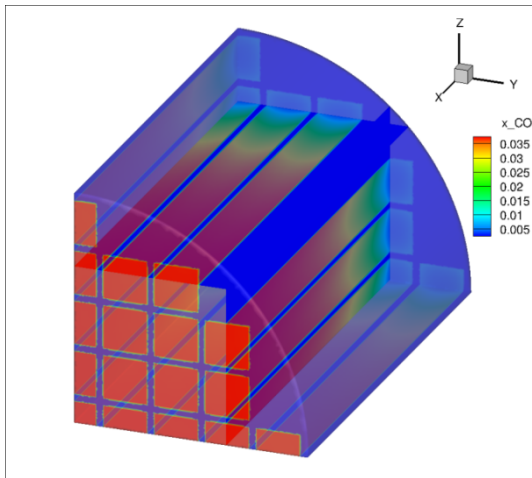
In the test condition 1, contours of mole fraction within the reactor are indicated in Figure 43. With the inlet boundary condition in this case, products are mainly H_2O and CO . Since the inlet concentration of methane is small, no significant oxidation is shown in the process and oxygen is not completely consumed. The conversion of methane in this case is about 85%.



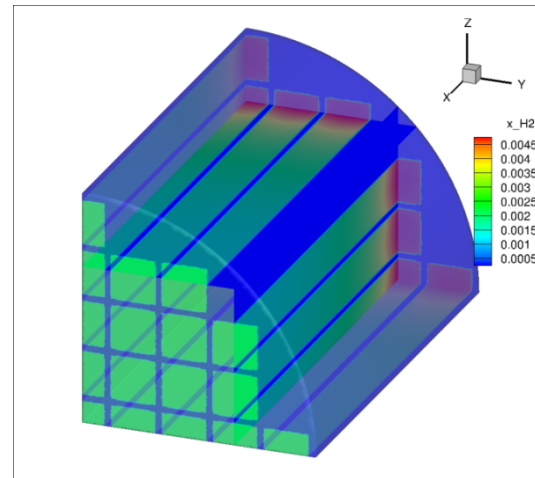
a)



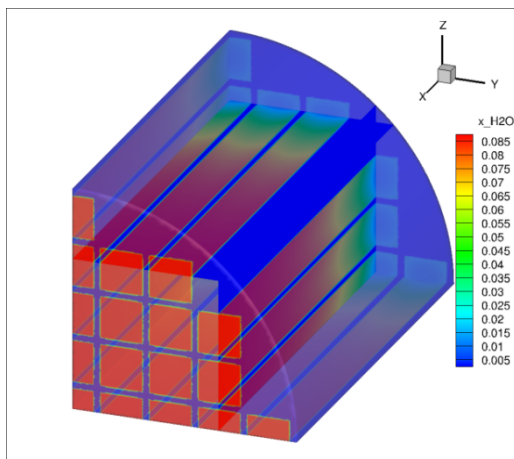
b)



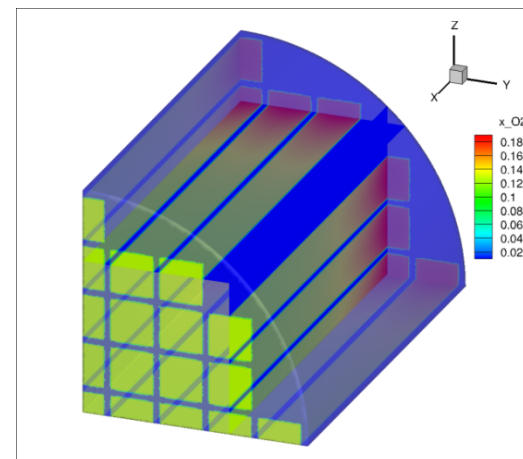
c)



d)



e)



f)

Figure 43 Contour plots for species mole fractions for test condition 1 a) CH₄ b) CO₂ c) CO d) H₂ e) H₂O f) O₂

The reactor is performed as a methane fuel reformer in the test condition 2. At the test condition 2, the temperature of the reactor is fixed to 1100 K and inflow concentrations are changed. Temperature and velocity contours are shown in Figure 44. The maximum velocity in this case is increased compared with the previous one because the reactor temperature is increased. As indicated in Figure 45, concentrations of the species are totally different compared with the previous case. Hydrogen is the main product of this process. The oxygen is completely consumed and the conversion of the methane is about 91%. As shown in both test cases, the gradient of the hydrogen mole fraction is smaller across the cross section of the channel because hydrogen has a higher diffusion coefficient relative to other species considered in this simulation.

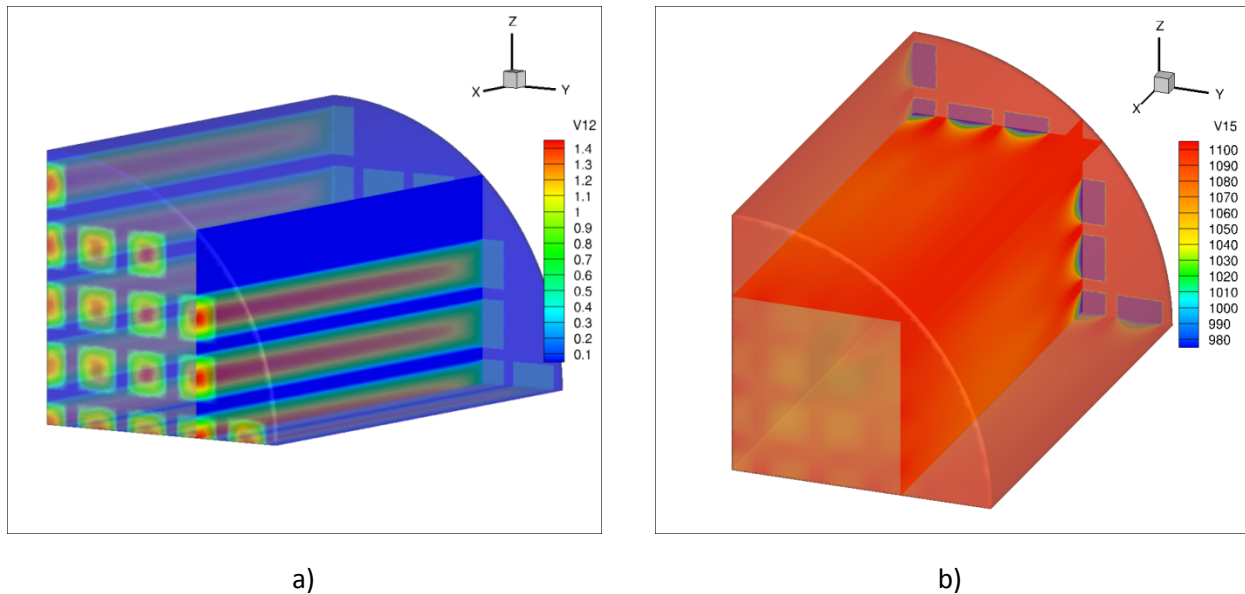
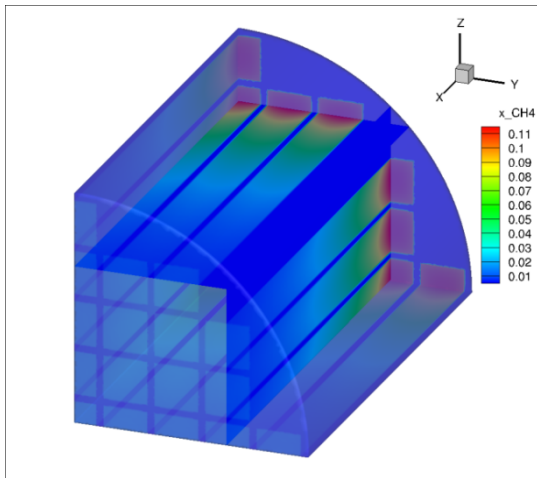
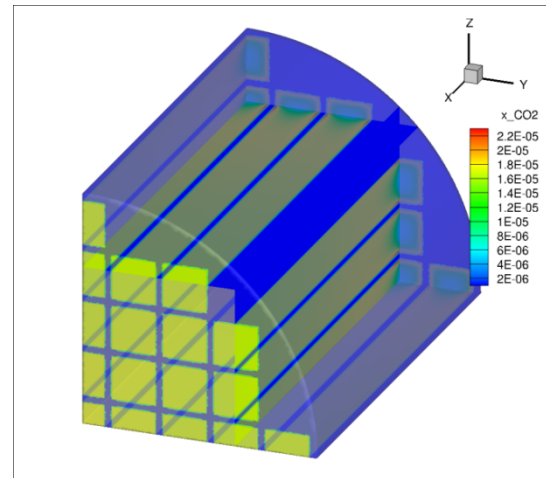


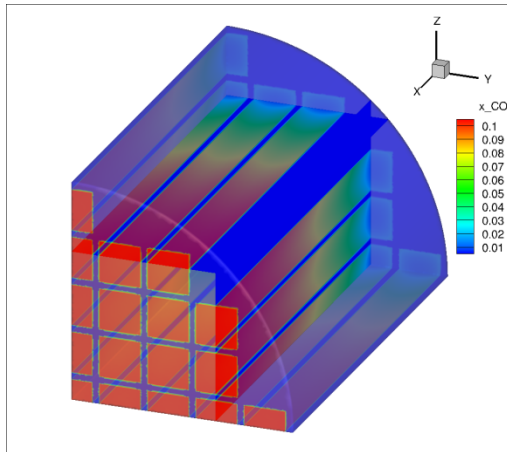
Figure 44 Contours of a) Velocity b) Temperature for the reactor at test conditions 2



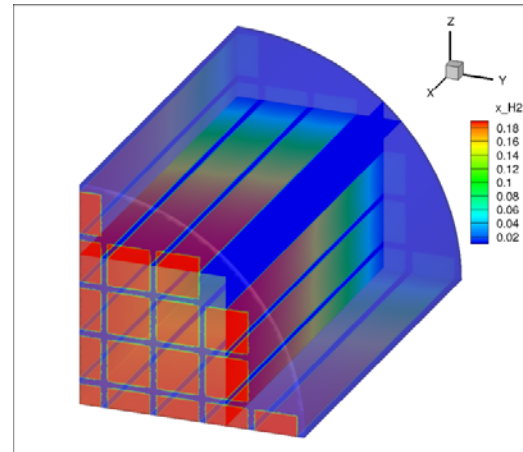
a)



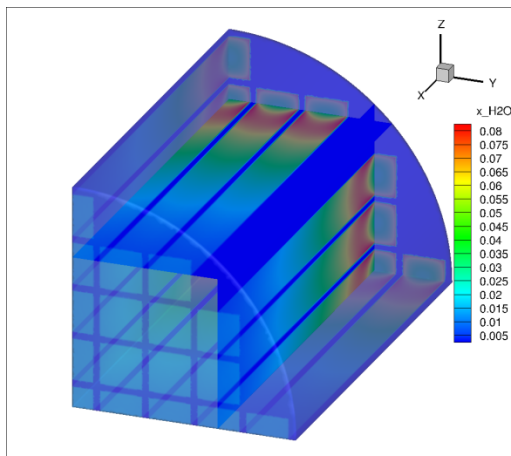
b)



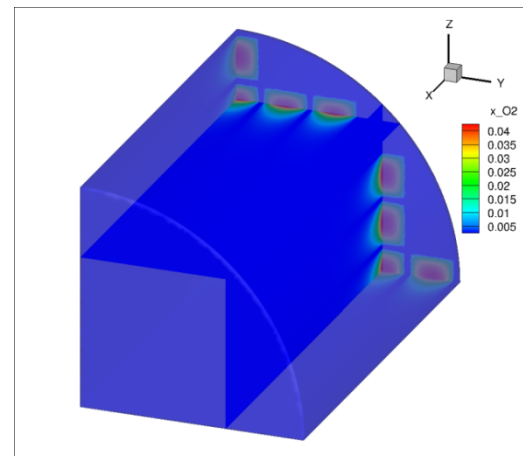
c)



d)



e)



f)

Figure 45 Contour plots for species mole fractions at test conditions 2 a) CH_4 b) CO_2 c) CO d) H_2 e) H_2O f) O_2

In the second test case, the reactor is a rhodium-coated monolithic honeycomb with a 2 cm diameter cylinder and a channel density of 600 cpsi (channels per square inch). A value of 2 W/(mK) was used for the thermal conductivity of the solid. The structure of the reactor is illustrated in Figure 46. For simulations, a quarter of the reactor is considered because of the symmetry properties. Figure 47 and Figure 48 indicate the mesh and the boundary conditions used in the numerical analysis, respectively. A number of 3,308,100 prism cells (9,924,300) with triangular base are generated with Pointwise software [51] for analyzing of the catalytic combustion within the reactor.

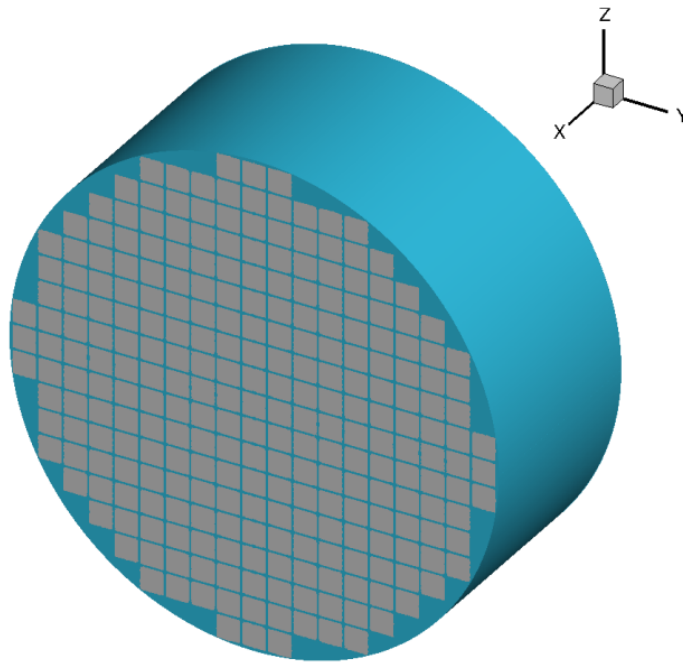


Figure 46 The structure of the reactor

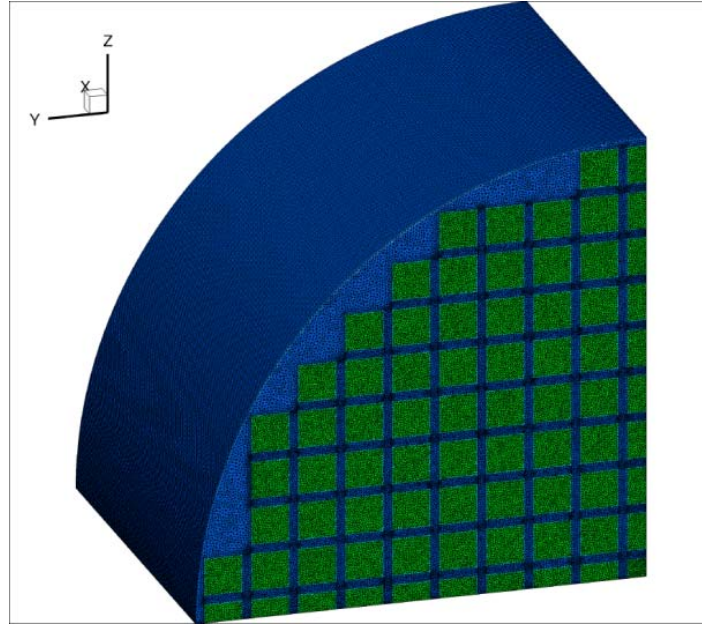


Figure 47 The mesh generated for the simulation

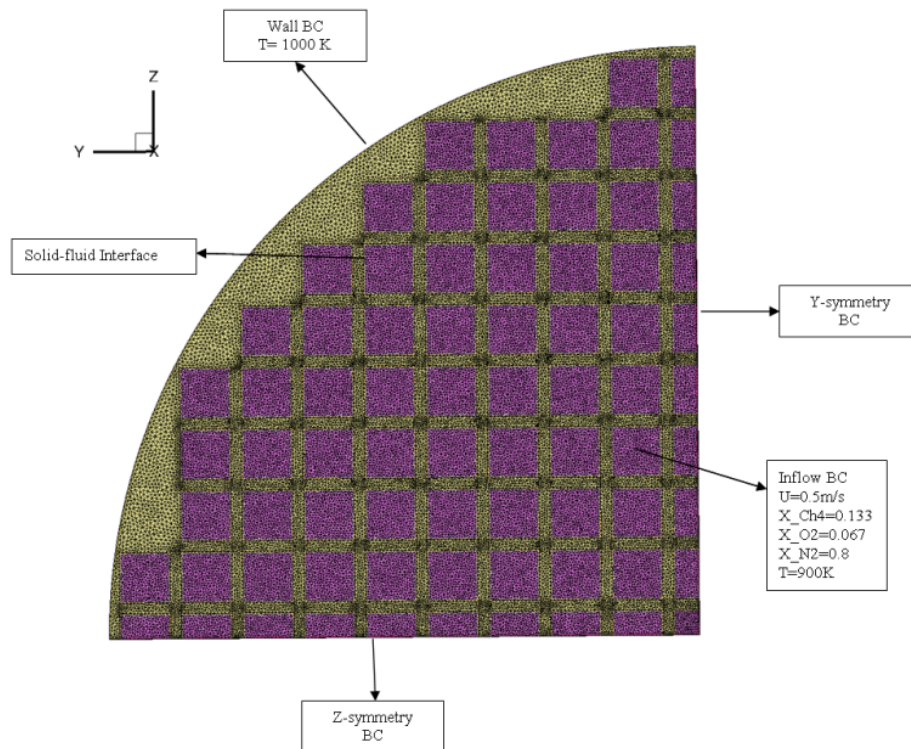


Figure 48 The boundary conditions for the simulation

Figure 49 shows the contour of species concentration within the reactor. As shown in the figure, variation of the gas mass concentrations along the reactor are almost the same for all the inner channels. The only difference is in the channels near the external boundary of the reactor. The temperature distribution within the reactor has a significant effect on the mass concentration of species and eventually the reactor performance. Because the temperature distribution in the regions close to the external boundary of the reactor is different from other regions, a different flow pattern is seen within the reactor. The difference for the species of H_2 and CO_2 is more visible, and the O_2 mass fraction is less sensitive to the temperature distribution within the reactor.

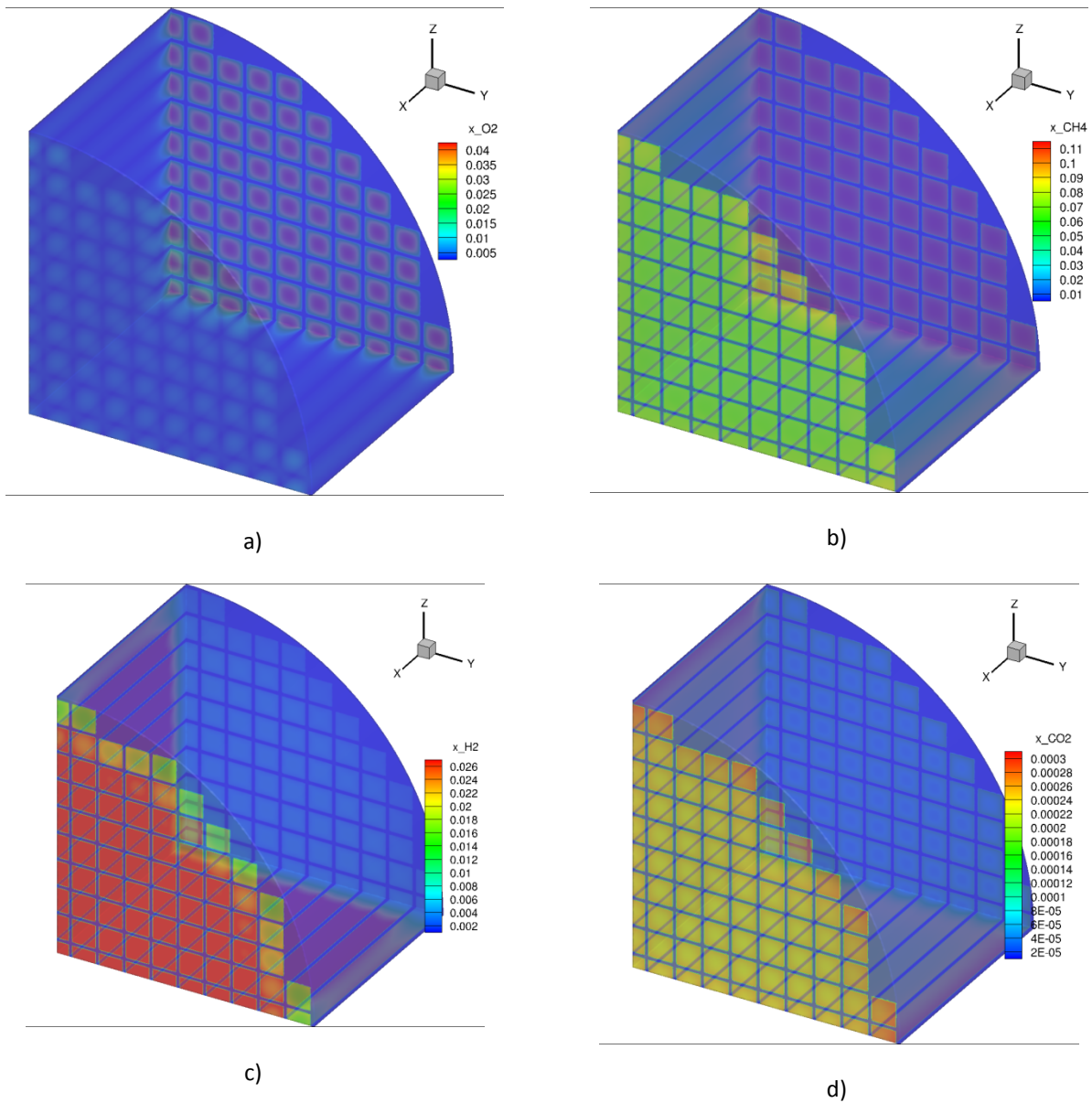


Figure 49 Contour plots for the reactor a) O₂ mole fraction b) CH₄ mole fraction c) H₂ mole fraction d) CO₂ mole fraction e) Temperature

5.1. SENSITIVITY ANALYSIS OF THE FULL REACTOR

The following two cost functions are considered for sensitivity analysis:

Case-1: the mean value of the CH₄ concentration at the outlet boundary.

Case-2: the mean value of the H₂ concentration at the outlet boundary.

The operating conditions are the same as described in test condition 2 of Table 9. Improving the performance of the fuel reforming is the ultimate goal of the reactor design: the first cost function is minimizing of CH_4 concentration, and the second cost function is the maximizing of H_2 concentration. Sensitivity derivatives of the cost functions representing the reactor performance with respect to various design parameters can be extremely useful in the design cycle.

Four design parameters are included to compute sensitivity derivatives of the aforementioned objective functions. The design parameters are the inlet velocity, the inlet methane concentration, the inlet oxygen concentration and thermal conductivity of monolith.

Table 10 shows the sensitivity derivatives of both cost functions obtained using the discrete adjoint method for the full reactor.

Table 10 Sensitivity derivatives of both cost functions obtained using the discrete adjoint method for the full reactor

DV	Cost-1	Cost-2
Inlet velocity	5.6876980509e-3	-1.7594093681e-3
Inlet methane density	1.1162738317e-1	1.8562329355e-1
Inlet oxygen density	-3.5172116328e-2	-8.3257422654e-2
Thermal conductivity of monolith	-1.1102201864e-4	2.4238135909e-5

CHAPTER 6

CONCLUSION

6.1. SUMMARY

The complex interaction of chemical and physical processes inside the methane reforming reactor is numerically studied with an implicit, unstructured finite volume based multi-species Navier-Stokes solver. The surface chemistry, heterogeneous combustion and coverages are computed and solved by coupling the high-fidelity simulation with Cantera. Coupling with the Cantera package enabled solving the stiff system of equations encountered while modeling the surface chemistry. The governing equations for the fluid and solid phases (the reactor's body) are solved simultaneously. For validation, numerical results are compared with experimental data and good agreement is observed for the catalytic partial oxidation. To assess the effect of various parameters on reactor efficiency, a parametric study was performed. This study indicated that the conversion of methane decreases with increasing inlet velocity and, therefore, Reynolds number. Moreover, the methane and hydrogen production increases with increasing catalytic wall temperature; methane conversion decreases with increasing methane/oxygen ratio, and hydrogen production is higher at richer mixtures. Sensitivity analysis was additionally used to assess the effect of design parameters on reactor performance. Verification of these sensitivity derivatives was performed using finite-difference, direct differentiation, and adjoint formulations. From sensitivity analysis it was observed that the methane concentration, followed by oxygen concentration, play the most significant roles in the

mean value of H_2 concentration. Finally, utilizing the sensitivity analysis capability, computational design was performed with a gradient-based optimization algorithm. Considering the inlet velocity, wall temperature and inlet methane concentration as design variables, two optimization cases were performed. The first optimization selected the mean value of CH_4 concentration at the outlet boundary as the objective function, and compared the numerical performance of Fletcher-Reeves conjugate gradient and quasi-Newton algorithms. The second optimization case selected hydrogen concentration at the outlet boundary as the objective function, and demonstrated significant reactor improvement over the baseline design. The results obtained from the optimization process show that numerical optimization can be successfully used to improve the performance of the reactor with less computational cost than conventional methods.

6.2. RECOMMENDATIONS FOR FUTURE WORK

The catalytic reactors are mainly used in fuel reforming and can be worked in three different reforming modes of steam reforming (SR), partial oxidation (POX) and autothermal reforming (ATR). Catalytic combustion is also used in a wide variety of applications, mainly driven by environmental concerns like automotive catalytic converters, gas turbine and selective catalytic reactor for reduction of pollutants and production of low temperature heat.

Catalytic reactors are generally characterized by the complex interaction of various physical and chemical processes. Because of the complexity and coupled interaction of the mass and heat transfer, design and optimization of catalytic reactors is difficult and expensive. Computational fluid dynamics (CFD) can be used as an appropriate tool for the understanding the interaction of physics and chemistry in the reactor and support reactor design and

engineering. CFD also can be used for the supporting of the experimental tests. It also can be a time-efficient and inexpensive alternative to trial-and-error experimental investigations.

Some extensions may be:

- Model the heterogeneous reaction rates with some fundamental methods like Ab-initio calculation, Density function theory (DFT) and Kinetic Monte Carlo.
- Extend the numerical simulations to other engineering and industrial applications like automotive catalytic converters and stationary gas turbines for reducing pollutants.
- Consider the homogenous combustion in the simulations and study the effects on the distribution of gas species within the reactor
- Develop the numerical model to investigate the behavior of the catalytic combustion of fuel reformers with more complex features and with heavy fuels like Diesel.
- Increase the speed up of the numerical procedure using GPU-accelerated computing in solving the stiff system of equations of the surface chemistry.

REFERENCES

- [1] R. E. Hayes and S. T. Kolaczkowski, *Introduction to Catalytic Combustion*, Gordon and Breach Science Publishers, 1997.
- [2] O. Deutschmann, *Modeling and Simulation of Heterogeneous Catalytic Reactions*, Wiley-VCH, 2012.
- [3] H. D. Minh, *Numerical Methods for Simulation and Optimization of Chemically Reacting Flows in Catalytic Monoliths*, PhD Thesis, University of Heidelberg, 2005.
- [4] M. Hettel, C. Diehm, B. Torkashvand and O. Deutschmann, "Critical Evaluation of In-situ Probe Techniques for Catalytic Honeycomb Monoliths," *Catalysis Today*, vol. 216, 2013.
- [5] A. Kumar, *Physical Models and Computational Algorithms for Simulation of Catalytic Monolithic Reactors*, PhD Thesis, Ohio State University, 2009.
- [6] L. L. Raja, R. J. Kee, O. Deutschmann, J. Warnatz and L. D. Schmidt, "A critical evaluation of Navier–Stokes, boundary-layer, and plug-flow models of the flow and chemistry in a catalytic-combustion monolith," *Catalysis Today*, vol. 59, no. 1-2, pp. 47-60, 2000.
- [7] A. E. Cerkanowicz, R. B. Cole and J. G. Stevens, "Catalytic Combustion Modeling; Comparisons With Experimental Data," *ASME. J. Eng. Power*, vol. 99, no. 4, pp. 593-600, 1997.
- [8] J. F. Kramer, S. A. Reihani and G. S. Jackson, "Low Temperature Combustion of Hydrogen on Supported Pd Catalysis," in *29th International Symposium on Combustion*, Japon, 2002.
- [9] O. Deutschmann, L. I. Maier, U. Riedel, A. H. Stroemman and R. W. Dibble, "Hydrogen assisted catalytic combustion of methane on platinum," *Catalysis Today*, vol. 59, no. 1-2, pp. 141-150, 2000.
- [10] U. Dogwiler, P. Benz and J. Mantzaras, "Two-Dimensional Modelling for Catalytically Stabilized Combustion of a Lean Methane-Air Mixture with Elementary Homogeneous and Heterogeneous Chemical Reactions," *Combustion and Flame*, vol. 116, pp. 243-258, 1999.
- [11] P. Markatou, L. D. Pfefferle and M. D. Smooke, "A computational study of methane-air combustion over heated catalytic and non-catalytic surfaces," *Combustion and Flame*, vol. 93, no. 1-2, pp. 185-201, 1993.
- [12] M. Hartmann, L. Maier, H. D. Minh and O. Deutschmann, "Catalytic partial oxidation of iso-octane over rhodium catalysts: An experimental, modeling, and simulation study," *Combustion and Flame*,

- vol. 157, no. 9, pp. 1771-1782, 2010.
- [13] M. Maestri and A. Cuoci, "Coupling CFD with detailed microkinetic modeling in heterogeneous catalysis," *Chemical Engineering Science*, vol. 96, pp. 106-117, 2013.
- [14] M. Hettel, C. Diehm, H. Bonart and O. Deutschmann, "Numerical simulation of a structured catalytic methane reformer by DUO: The new computational interface for OpenFOAM® and DETCHEM™," *Catalysis Today*, vol. 258, no. 2, pp. 230-240, 2015.
- [15] "www.openfoam.org," OpenFOAM, The Open Source CFD Toolbox, 2014. [Online].
- [16] O. Deutschmann, S. Tischer, C. Correa, D. Chatterjee, S. Kleditzsch, V. M. Janardhanan, N. Mladenov, H. D. Minh, H. Karadeniz and M. Hettel, "www.detchem.com," DETCHEM Software Package, 2014. [Online].
- [17] H. D. Minh, H. G. Bock, S. Tischer and O. Deutschmann, "Optimization of Two-Dimensional Flows with Homogeneous and Heterogeneously Catalyzed Gas-Phase Reactions," *AIChE Journal*, vol. 54, no. 9, pp. 2432-2440, 2008.
- [18] H. D. Minh, Numerical Methods for Simulation and Optimization of Chemically Reacting Flows in Catalytic Monoliths, PhD Thesis, University of Heidelberg, 2005.
- [19] D. Arnost and P. Schneider, "Dynamic transport of multicomponent mixtures of gases in porous solids," *The Chemical Engineering Journal*, vol. 57, pp. 91-99, 1995.
- [20] M. Coltrin, R. Kee and F. Rupley, "Surface chemkin: A general formalism and software for analyzing heterogeneous chemical kinetics at gas-solid interfaces," *Int. J. Chem. Kinet*, vol. 23, p. 1111, 1991.
- [21] P. L. Roe, "Approximate Reimann Solvers, Parameter Vectors and Difference Schemes," *Journal of Computational Physics*, vol. 43, pp. 357-372, 1981.
- [22] M. Busby, Steps Toward More Accurate and Efficient Simulations of Reactive Flows, Ph.D. Thesis, Mississippi State University, 1997.
- [23] S. Kapadia, Computational Design and Sensitivity Analysis of Solid Oxide Fuel Cells, Ph.D Thesis, University of Tennessee at Chattanooga, 2008.
- [24] J. C. Newman, W. K. Anderson and D. Whitfield, "Multidisciplinary sensitivity derivatives using complex variables," Technical Report MSSU-COE-ERC-98-09, Engineering Research Center Report, Mississippi State University, 1998.
- [25] W. K. Anderson, J. C. Newman, D. Whitfield and E. Nielsen, "Sensitivity analysis for the navier-stokes equations on unstructured meshes using complex variables," *AIAA Journal*, vol. 39, p. 56-63, 2001.

- [26] C. E. Burdyslaw, Achieving Automatic Concurrency Between Computational Field Solvers and Adjoint Sensitivity Codes, Ph.D dissertation, University of Tennessee at Chattanooga, 2006.
- [27] Y. Saad and M. H. Schultz, "GMRES: A Generalized Minimal Residual Algorithm for Solving Nonsymmetric Linear Systems," *SIAM J. Sci. Stat. Comput.*, vol. 7, pp. 856-869, 1986.
- [28] METIS, [Online]. Available: <http://glaros.dtc.umn.edu/gkhome/views/metis>.
- [29] A. G. Dixon, Modeling and simulation of heterogeneous catalytic processes, vol. 45, Advances in Chemical Engineering, Academic Press, 2014.
- [30] R. J. Kee, M. Coltrin and P. Glarborg, Chemically Reacting Flow: Theory & Practice, John Wiley & Sons, 2003.
- [31] A. Quarteroni, R. Sacco and F. Saleri, Numerical mathematics, Springer, 2000.
- [32] A. C. Hindmarsh, P. N. Brown, K. E. Grant, S. L. Lee, R. Serban, D. E. Shumaker and C. S. Woodward, "SUNDIALS: Suite of Nonlinear and Differential/Algebraic Equation Solvers," *ACM Transactions on Mathematical Software*, vol. 31, no. 3, pp. 363-396, 2005.
- [33] P. N. Brown, G. D. Byrne and A. C. Hindmarsh, "VODE: a Variable-coefficient ODE Solver," *SIAM J. Sci. Stat. Comput.*, vol. 10, no. 5, pp. 1038-1051, 1989.
- [34] L. R. Petzold, "A description of DASSL: A differential/algebraic system solver," in *10th IMACS World Congress*, 1982.
- [35] O. Deutschmann, R. Schwiedemoch, L. I. Maier and D. Chatterjee, "Natural Gas Conversion in Monolithic Catalysts: Interaction of Chemical Reactions and Transport Phenomena," *Studies in Surface Science and Catalysis*, vol. 136, pp. 251-258, 2001.
- [36] D. G. Goodwin, H. K. Moffat and R. L. Speth, "Cantera: An object- oriented software toolkit for chemical kinetics, thermodynamics, and transport processes," 2015. [Online]. Available: <http://www.cantera.org>.
- [37] D. G. Goodwin, Cantera C++ User's Guide, California Institute of Technology, 2002.
- [38] B. M. Adams, L. E. Bauman, W. J. Bohnhoff, K. R. Dalbey, M. S. Ebeida, J. P. Eddy, M. S. Eldred, P. D. Hough, K. T. Hu, J. D. Jakeman, L. P. Swiler and D. M. Vigil, "DAKOTA, A Multilevel Parallel Object-Oriented Framework for Design Optimization, Parameter Estimation, Uncertainty Quantification, and Sensitivity Analysis: Version 5.2 User's Manual," Sandia Technical Report SAND2010-2183, 2009.
- [39] L. C. Elliott, Solid Oxide Fuel Cell Simulation and Design Optimization with Numerical Adjoint Techniques, Ph.D dissertation, University of Tennessee at Chattanooga, 2008.

- [40] O. Deutschmann, F. Behrendt and J. Warnatz, "Modelling and simulation of heterogeneous oxidation of methane on a platinum foil," *Catalysis Today*, pp. 461-470, 1994.
- [41] O. Deutschmann, R. Schmidt, F. Behrendt and J. Warnatz, "Numerical Modeling of Catalytic Ignition," *Proc. Combust. Inst.*, vol. 26, pp. 1747-1754, 1996.
- [42] V. Dupont, S. H. Zhang and A. Williams, "Experiments and simulations of methane oxidation on a platinum surface," *Chemical Engineering Science*, vol. 56, pp. 2659-2670, 2001.
- [43] J. F. Grcar, "The twopnt program for boundary value problems: Version 3.10 of March 1992," Sandia National Labs, Livermore, CA, 1992.
- [44] M. T. Heath, *Scientific Computing: An Introductory Survey*, McGraw-Hill, 1997.
- [45] K. L. Hohn, C. C. Huang and C. Cao, "Catalytic ignition of light hydrocarbons," *Journal of Natural Gas Chemistry*, vol. 18, no. 2, pp. 115-123, 2009.
- [46] M. Hartmann, L. Maier, H. D. Minh and O. Deutschmann, "Catalytic partial oxidation of iso-octane over rhodium catalysts: An experimental, modeling, and simulation study," vol. 157, no. 9, pp. 1771-1782, 2010.
- [47] O. Deutschmann and L. D. Schmidt, "Modeling the Partial Oxidation of Methane in a Short-Contact-Time Reactor," *AIChE Journal*, vol. 44, no. 11, pp. 2465-2477, 1998.
- [48] A. Grama, A. Gupta, G. Karypis and V. Kumar, *Introduction to Parallel Computing*, Second, Ed., Pearson, 2003.
- [49] J. C. Meza, R. A. Oliva, P. D. Hough and P. J. Williams, "OPT++: an object oriented toolkit for nonlinear optimization," *ACM Transactions on Mathematical Software*, vol. 33, no. 2, pp. 126- 136, 2007.
- [50] "DOT Users Manual, Version 4.20," Vanderplaats Research and Development, Inc., Colorado Springs, CO, 1995.
- [51] "www.pointwise.com," [Online].

APPENDIX A

CANTERA FILE FOR CATALYTIC COMBUSTION OF HYDROGEN ON PALLADIUM

This cti file is written based on the chemical reaction mechanism described in reference [37].

```

units(length = "cm", time = "s", quantity = "mol", act_energy = "J/mol")

ideal_gas(name = "gas",
  elements = "O H C",
  species = ""H2 H O2 H2O OH O"",
  options = ['skip_undeclared_elements',
    'skip_undeclared_species'],
  initial_state = state(temperature = 600.0, pressure = OneAtm,
    mole_fractions = 'H2:0.01, O2:0.21')
)

ideal_interface(name = "Pt_surf",
  elements = " Pd H O ",
  species = "" Pd(S) H(S) H2O(S) OH(S) O(S) """,
  phases = "gas",
  site_density = 1.55e-9,
  reactions = "all",
  initial_state = state(temperature = 1200.0,
    coverages = 'O(S):0.99, Pd(S):0.0, H(S):0.1')
)

#-----

species(name = "H2",
  atoms = " H:2 ",
  thermo = (
    NASA([ 300.00, 1000.00], [ 3.355351400E+00, 5.013614400E-04,
      -2.300690800E-07, -4.790532400E-10, 4.852258500E-13,
      -1.019162600E+03, -3.547722800E+00] ),
    NASA([ 1000.00, 5000.00], [ 3.066709500E+00, 5.747375500E-04,
      1.393831900E-08, -2.548351800E-11, 2.909857400E-15,
      -8.654741200E+02, -1.779842400E+00] )
  )
)

species(name = "H2O",
  atoms = " H:2 O:1 ",
  thermo = (
    NASA([ 300.00, 1000.00], [ 4.167723400E+00, -1.811497000E-03,
      5.947128800E-06, -4.869202100E-09, 1.529199100E-12,
      -3.028996900E+04, -7.313547400E-01] ),
    NASA([ 1000.00, 5000.00], [ 2.611047200E+00, 3.156313000E-03,
      -9.298543800E-07, 1.333153800E-10, -7.468935100E-15,
      -2.986816700E+04, 7.209126800E+00] )
  )
)

species(name = "H",
  atoms = " H:1 ",
  thermo = (
    NASA([ 200.00, 1000.00], [ 2.500000000E+00, 0.000000000E+00,
      0.000000000E+00, 0.000000000E+00, 0.000000000E+00,
      2.547365990E+04, -4.466828530E-01] ),
    NASA([ 1000.00, 6000.00], [ 2.500002860E+00, -5.653342140E-09,
      3.632517230E-12, -9.199497200E-16, 7.952607460E-20,
      2.547365890E+04, -4.466984940E-01] )
  )
)

# note = "L 5/93"
)

species(name = "OH",
  atoms = " O:1 H:1 ",

```

```

thermo = (
  NASA([ 200.00, 1000.00], [ 3.992015430E+00, -2.401317520E-03,
    4.617938410E-06, -3.881133330E-09, 1.364114700E-12,
    3.615080560E+03, -1.039254580E-01] ),
  NASA([ 1000.00, 6000.00], [ 2.838646070E+00, 1.107255860E-03,
    -2.939149780E-07, 4.205242470E-11, -2.421690920E-15,
    3.943958520E+03, 5.844526620E+00] )
)
# note = "TPIS78"
)
species(name = "O",
atoms = "O:1 ",
thermo = (
  NASA([ 200.00, 1000.00], [ 3.168267100E+00, -3.279318840E-03,
    6.643063960E-06, -6.128066240E-09, 2.112659710E-12,
    2.912225920E+04, 2.051933460E+00] ),
  NASA([ 1000.00, 6000.00], [ 2.543636970E+00, -2.731624860E-05,
    -4.190295200E-09, 4.954818450E-12, -4.795536940E-16,
    2.922601200E+04, 4.922294570E+00] )
)
# note = "L 1/90"
)
species(name = "O2",
atoms = "O:2 ",
thermo = (
  NASA([ 300.00, 1000.00], [ 3.783713500E+00, -3.023363400E-03,
    9.949275100E-06, -9.818910100E-09, 3.303182500E-12,
    -1.063810700E+03, 3.641634500E+00] ),
  NASA([ 1000.00, 5000.00], [ 3.612213900E+00, 7.485316600E-04,
    -1.982064700E-07, 3.374900800E-11, -2.390737400E-15,
    -1.197815100E+03, 3.670330700E+00] )
)
)
species(name = "O(S)",
atoms = "O:1 Pd:1 ",
thermo = (
  NASA([ 300.00, 1000.00], [ -9.498690400E-01, 7.404230500E-03,
    -1.045142400E-06, -6.112042000E-09, 3.378799200E-12,
    -1.320991200E+04, 3.613790500E+00] ),
  NASA([ 1000.00, 3000.00], [ 1.945418000E+00, 9.176164700E-04,
    -1.122671900E-07, -9.909962400E-11, 2.430769900E-14,
    -1.400518700E+04, -1.153166300E+01] )
)
)
species(name = "H(S)",
atoms = "H:1 Pd:1 ",
thermo = (
  NASA([ 300.00, 1000.00], [ -1.302987700E+00, 5.417319900E-03,
    3.127797200E-07, -3.232853300E-09, 1.136282000E-12,
    -4.227707500E+03, 5.874323800E+00] ),
  NASA([ 1000.00, 3000.00], [ 1.069699600E+00, 1.543223000E-03,
    -1.550092200E-07, -1.657316500E-10, 3.835934700E-14,
    -5.054612800E+03, -7.155523800E+00] )
)
)
species(name = "H2O(S)",
atoms = "O:1 H:2 Pd:1 ",
thermo = (
  NASA([ 300.00, 1000.00], [ -2.765155300E+00, 1.331511500E-02,

```

```

        1.012769500E-06, -7.182008300E-09, 2.281377600E-12,
        -3.639805500E+04, 1.209814500E+01] ),
NASA( [ 1000.00, 3000.00], [ 2.580305100E+00, 4.957082700E-03,
-4.689405600E-07, -5.263313700E-10, 1.199832200E-13,
-3.830223400E+04, -1.740632200E+01] )
    )
)

species(name = "Pd(S)",
atoms = " Pd:1 ",
thermo = (
    NASA( [ 300.00, 1000.00], [ 0.000000000E+00, 0.000000000E+00,
0.000000000E+00, 0.000000000E+00, 0.000000000E+00,
0.000000000E+00, 0.000000000E+00] ),
    NASA( [ 1000.00, 3000.00], [ 0.000000000E+00, 0.000000000E+00,
0.000000000E+00, 0.000000000E+00, 0.000000000E+00,
0.000000000E+00, 0.000000000E+00] )
    )
)

species(name = "O2(S)",
atoms = " O:2 Pd:1 ",
thermo = (
    NASA( [ 300.00, 1000.00], [-0.20174649E+01, 0.14146218E-01, -0.16376665E-05,
-0.11264421E-07, 0.60101386E-11, -0.25084473E+04, 0.79811935E+01] ),
    NASA( [ 1000.00, 3000.00], [0.35989249E+01, 0.20437732E-02, -0.23878221E-06, -0.22041054E-09, 0.53299430E-13,
-0.41095444E+04, -0.21604582E+02] )
    )
)

species(name = "OH(S)",
atoms = " O:1 H:1 Pd:1 ",
thermo = (
    NASA( [ 300.00, 1000.00], [ -2.034088100E+00, 9.366268300E-03,
6.627521400E-07, -5.207488700E-09, 1.708873500E-12,
-2.531994900E+04, 8.986318600E+00] ),
    NASA( [ 1000.00, 3000.00], [ 1.824997300E+00, 3.250156500E-03,
-3.119754100E-07, -3.460320600E-10, 7.917147200E-14,
-2.668549200E+04, -1.228089100E+01] )
    )
)

species(name = "H2(S)",
atoms = " H:2 Pd:1 ",
thermo = (
    NASA( [ 300.00, 1000.00], [-0.21517782E+01, 0.87039210E-02, 0.11154106E-05,
-0.42477102E-08, 0.96133203E-12, -0.22640681E+04, 0.97397461E+01] ),
    NASA( [ 1000.00, 3000.00], [0.15330955E+01, 0.34586885E-02, -0.32622225E-06, -0.36824219E-09, 0.83855205E-13,
-0.36401533E+04, -0.10822206E+02] )
    )
)

#####!
#####      H2-O2 Surface Reaction on Pd      #####!
#####!
# Reaction 1
surface_reaction( "H2 + 2 Pd(S) => 2 H(S)", stick(0.70,0.0,0.0))

# Reaction 2
surface_reaction( "2 H(S) => H2 + 2 Pd(S)",
Arrhenius(4.800E+21, 0, 84.0,

```

```

coverage = ['H(S)', 0.0, 0.0, -15.0])

# Reaction 3
surface_reaction("H + Pd(S) => H(S)", stick(1.00,0.0,0.0))

# Reaction 4
surface_reaction("O2 + 2 Pd(S) => 2 O(S)", stick(0.400E-00,0.0,0.0))

# Reaction 5
surface_reaction("2 O(S) => O2 + 2 Pd(S)", [7.100E+21,0.0,230.0])

# Reaction 6
surface_reaction("O + Pd(S) => O(S)", stick(1.00,0.0,0.0))

# Reaction 7
surface_reaction("H2O + Pd(S) => H2O(S)", stick(0.75,0.0,0.0))

# Reaction 8
surface_reaction("H2O(S) => H2O + Pd(S)", [1.300E+13,0.0,44.0])

# Reaction 9
surface_reaction("OH + Pd(S) => OH(S)", stick(1.00,0.0,0.0))

# Reaction 10
surface_reaction("OH(S) => OH + Pd(S)", [1.300E+13,0.0,213.0])

# Reaction 11
surface_reaction("H(S) + O(S) = OH(S) + Pd(S)", [3.70E+21,0.00,11.5])

# Reaction 12
surface_reaction("H(S) + OH(S) = H2O(S) + Pd(S)", [3.70E+21,0.00,17.4])

# Reaction 13
surface_reaction("OH(S) + OH(S) = H2O(S) + O(S)", [3.70E+21,0.00,48.2])

```

APPENDIX B

REACTION MECHANISM FOR METHANE CATALYTIC COMBUSTION ON PLATINUM

- A, b and E are Arrhenius parameters for the rate constants $k = AT^b \exp(-\frac{E}{RT})$
- $cov(s)$ (surface coverage of species s) and ϵ are the parameters in the modified reaction rate formula $k = AT^b \exp(-\frac{E}{RT}) * \exp(-\epsilon \frac{cov(s)}{RT})$

	Reaction	A(cm,mol,s)	b	E (J/mol)	
	Adsorption				
1	H + Pt => H_Pt	1	0	0	STICK
2	O2 + 2 Pt => 2O_Pt	0.023	0	0	STICK
3	O + Pt => O_Pt	1	0	0	STICK
4	H2O + Pt => H2O_Pt	7.50E-01	0	0	STICK
5	OH + Pt => OH_Pt	1.00E+00	0	0	STICK
	Desorption				
6	H2O_Pt => H2O + Pt	1.00E+13	0	40300	
7	OH_Pt => OH + Pt	1.00E+13	0	192800	
8	2O_Pt => O2 + 2 Pt	3.70E+21	0	213200	$cov(s) = cov(O_Pt)$ $\epsilon = -60000.0 \text{ J/mol}$
9	2H_Pt => H2 + 2 Pt	3.70E+21	0	67400	$cov(s) = cov(H_Pt)$ $\epsilon = -60000.0 \text{ J/mol}$
10	CO_Pt => CO + Pt	1.00E+13	0	125500	
11	CO2_Pt => CO2 + Pt	1.00E+13	0	20500	
	Surface reactions				
12	H2 + 2 Pt => 2H_Pt	4.46E+10	0.5	0	First order reaction rate in Pt
13	O2 + 2 Pt => 2O_Pt	1.80E+21	-0.5	0	
14	H_Pt + O_Pt = OH_Pt + Pt	3.70E+21	0	11500	
15	H_Pt + OH_Pt = H2O_Pt + Pt	3.70E+21	0	17400	
16	OH_Pt + OH_Pt = H2O_Pt + O_Pt	3.70E+21	0	48200	
17	CO + Pt => CO_Pt	1.62E+20	0.5	0	Second order reaction rate in Pt
18	CO_Pt + O_Pt => CO2_Pt + Pt	3.70E+21	0	105000	
19	CH4 + 2 Pt => CH3_Pt + H_Pt	4.63E+20	0.5	0	2.3 order reaction rate in Pt
20	CH3_Pt + Pt => CH2_Pt + H_Pt	3.70E+21	0	20000	
21	CH2_Pt + Pt => CH_Pt + H_Pt	3.70E+21	0	20000	
22	CH_Pt + Pt => C_Pt + H_Pt	3.70E+21	0	20000	
23	C_Pt + O_Pt => CO_Pt + Pt	3.70E+21	0	62800	
24	CO_Pt + Pt => C_Pt + O_Pt	1.00E+18	0	184000	

APPENDIX C

REACTION MECHANISM FOR METHANE CATALYTIC COMBUSTION ON RHODIUM

- A, b and E are Arrhenius parameters for the rate constants $k = AT^b \exp(-\frac{E}{RT})$

	Reaction	A(cm,mol,s)	b	E (J/mol)	
	Adsorption				
1	H2 +_Rh_ +_Rh_ =>H_Rh_ +H_Rh	1.00E-02	0	0	STICK
2	O2 +_Rh_ +_Rh_ =>O_Rh_ +O_Rh	1.00E-02	0	0	STICK
3	CH4 +_Rh_ =>CH4_Rh	8.00E-03	0	0	STICK
4	H2O +_Rh_ =>H2O_Rh	1.00E-01	0	0	STICK
5	CO2 +_Rh_ =>CO2_Rh	1.00E-05	0	0	STICK
6	CO +_Rh_ =>CO_Rh	5.00E-01	0	0	STICK
	Desorption				
7	H_Rh_ +H_Rh =>_Rh_ +_Rh_ +H2	3.00E+21	0	77800	
8	O_Rh_ +O_Rh =>_Rh_ +_Rh_ +O2	1.30E+22	0	355200	
9	H2O_Rh =>H2O +_Rh_	3.00E+13	0	45000	
10	CO_Rh =>CO +_Rh_	3.50E+13	0	133400	
11	CO2_Rh =>CO2 +_Rh_	1.00E+13	0	21700	
12	CH4_Rh =>CH4 +_Rh_	1.00E+13	0	25100	
	Surface reactions				
13	H_Rh_ +O_Rh =>OH_Rh +_Rh_	5.00E+22	0	83700	
14	OH_Rh +_Rh_ =>H_Rh_ +O_Rh	3.00E+20	0	37700	
15	H_Rh_ +OH_Rh =>H2O_Rh +_Rh_	3.00E+20	0	33500	
16	H2O_Rh +_Rh_ =>H_Rh_ +OH_Rh	5.00E+22	0	106400	
17	OH_Rh_ +OH_Rh =>H2O_Rh +O_Rh	3.00E+21	0	100800	
18	H2O_Rh +O_Rh =>OH_Rh_ +OH_Rh	3.00E+21	0	224200	
19	C_Rh_ +O_Rh =>CO_Rh +_Rh_	3.00E+22	0	97900	
20	CO_Rh +_Rh_ =>C_Rh_ +O_Rh	2.50E+21	0	169000	
21	CO_Rh_ +O_Rh =>CO2_Rh +_Rh_	1.40E+20	0	121600	
22	CO2_Rh +_Rh_ =>CO_Rh_ +O_Rh	3.00E+21	0	115300	
23	CH4_Rh +_Rh_ =>CH3_Rh_ +H_Rh	3.70E+21	0	61000	
24	CH3_Rh_ +H_Rh =>CH4_Rh +_Rh_	3.70E+21	0	51000	
25	CH3_Rh +_Rh_ =>CH2_Rh_ +H_Rh	3.70E+24	0	103000	
26	CH2_Rh_ +H_Rh =>CH3_Rh +_Rh_	3.70E+21	0	44000	
27	CH2_Rh +_Rh_ =>CH_Rh_ +H_Rh	3.70E+24	0	100000	
28	CH_Rh_ +H_Rh =>CH2_Rh +_Rh_	3.70E+21	0	68000	
29	CH_Rh +_Rh_ =>C_Rh_ +H_Rh	3.70E+21	0	21000	
30	C_Rh_ +H_Rh =>CH_Rh +_Rh_	3.70E+21	0	172800	
31	CH4_Rh_ +O_Rh =>CH3_Rh_ +OH_Rh	1.70E+24	0	80300	
32	CH3_Rh_ +OH_Rh =>CH4_Rh +O_Rh	3.70E+21	0	24300	
33	CH3_Rh +O_Rh =>CH2_Rh_ +OH_Rh	3.70E+24	0	120300	
34	CH2_Rh_ +OH_Rh =>CH3_Rh +O_Rh	3.70E+21	0	15100	

35	$\text{CH}_2\text{Rh} + \text{O}_\text{Rh} \Rightarrow \text{CH}_\text{Rh} + \text{OH}_\text{Rh}$	3.70E+24	0	158400	
36	$\text{CH}_\text{Rh} + \text{OH}_\text{Rh} \Rightarrow \text{CH}_2\text{Rh} + \text{O}_\text{Rh}$	3.70E+21	0	36800	
37	$\text{CH}_\text{Rh} + \text{O}_\text{Rh} \Rightarrow \text{C}_\text{Rh} + \text{OH}_\text{Rh}$	3.70E+21	0	30100	
38	$\text{C}_\text{Rh} + \text{OH}_\text{Rh} \Rightarrow \text{CH}_\text{Rh} + \text{O}_\text{Rh}$	3.70E+21	0	145500	

VITA

Arman Raoufi completed the Bachelor of Science degree in Mechanical Engineering at the Ferdowsi University of Mashhad and Master of Science degree in Mechanical Engineering at the K.N. Toosi University of Technology in 2004 and 2006 receptively. After graduating, he worked for one year at the K.N. Toosi University of Technology as a research assistant and then joined renewable energy department of Niroo Research Institute where he worked on the design, manufacturing and simulation of fuel cells for more four years. In 2011, he decided to pursue his Ph.D. in Computational Engineering at the SimCenter, the University of Tennessee at Chattanooga and earned his degree in 2016.